

2022

Study of Resonantly Stabilized Radicals in Combustion Environments

James H. Lee

West Virginia University, yolee1@mix.wvu.edu

Follow this and additional works at: <https://researchrepository.wvu.edu/etd>

 Part of the [Physical Chemistry Commons](#)

Recommended Citation

Lee, James H., "Study of Resonantly Stabilized Radicals in Combustion Environments" (2022). *Graduate Theses, Dissertations, and Problem Reports*. 11371.

<https://researchrepository.wvu.edu/etd/11371>

This Dissertation is protected by copyright and/or related rights. It has been brought to you by the The Research Repository @ WVU with permission from the rights-holder(s). You are free to use this Dissertation in any way that is permitted by the copyright and related rights legislation that applies to your use. For other uses you must obtain permission from the rights-holder(s) directly, unless additional rights are indicated by a Creative Commons license in the record and/ or on the work itself. This Dissertation has been accepted for inclusion in WVU Graduate Theses, Dissertations, and Problem Reports collection by an authorized administrator of The Research Repository @ WVU. For more information, please contact researchrepository@mail.wvu.edu.

Study of Resonantly Stabilized Radicals in Combustion Environments

James Lee

Dissertation submitted
to the Eberly College of Arts and Sciences
at West Virginia University

in partial fulfillment of the requirements for the degree of
Doctor of Philosophy in
Chemistry

Fabien Goulay, Ph.D., Chair

Blake Mertz, Ph.D

Brian Popp, Ph.D

Terry Gullion, Ph.D

Earl Scime, Ph.D

C. Eugene Bennet Department of Chemistry

Morgantown, West Virginia
2022

Keywords: Gas Phase Reactions, Free Radicals, Resonantly Stabilized Radicals, Hydrocarbons, Kinetics, Pulsed Laser Photolysis, Laser-Induced Fluorescence, High-Temperature, Photoionization Mass Spectrometry, Propargyl, Hydroxyl

Copyright 2022 James Lee

Abstract

Study of Resonantly Stabilized Radicals in Combustion Environments

James Lee

Resonantly stabilized radicals (RSRs) play an important role in combustion environments due to their high stability resulting from resonance. Many RSRs such as the propargyl, allyl, or benzyl radicals are precursors to the formation of polycyclic aromatic hydrocarbons (PAHs), which can aggregate to form soot. Due to their stability, these RSRs can accumulate in combustion environments in significant quantities. The primary way these radical species are consumed in flames or by reactions with other abundant radicals, by self-recombination of propargyl to form benzene, or in the form of other abundant radicals such as the hydroxyl radical. Experimentally determining the pathways for consumption of these radicals is necessary to better understand soot formation pathways. Product analysis is obtained for the $C_3H_3 + OH$ reaction using a multiplexed photoionization time-of-flight mass spectrometry coupled to synchrotron radiation at the Advanced Light Source (ALS) of the Lawrence Berkeley National Laboratories in Berkeley, California. Product analysis supports the production of m/z 56, with the predominant isotope formed being acrolein. Notably absent is the presence of propargyl alcohol, which indicates that the allylic form is the most favorable structure. Among the smaller radical exit pathways, the vinyl radical is produced in appreciable quantities, indicating that its coproduct, CO, is a major product of the reaction at higher temperatures.

The study of kinetics for these reactions in-house requires proper experimental setup that can provide the necessary conditions such as pressure and temperature. For combustion reactions, higher experimental temperatures are necessary to emulate the conditions in a flame. To this end, a high-temperature fast flow reactor is constructed to provide the necessary conditions for the reaction. Pressure measurements were conducted to obtain the flow velocity, pressure, and temperature of the gas in the high-temperature flow past a standing normal shockwave. The standing normal shockwave is formed by increasing pressure downstream from the supersonic gas expansion to form a differential of pressure between the nozzle and flow cell. To verify the temperature extracted from the pressure measurements, the CN radical was used to determine the temperature of a gas through rotational spectroscopy. CN radicals were produced by pulsed laser photolysis (PLP) at 266 nm from ICN precursor and its concentration is monitored using laser-induced fluorescence (LIF) at an excitation wavelength range of 378 - 382 nm. The rotational spectrum is obtained and analyzed with the PGOPHER software to determine the gas temperature.

To my parents, Sang and Myung Lee
Whose many sacrifices
As well as unyielding love and support
I will always be grateful for

Acknowledgements

Many people have supported me through my graduate tenure at West Virginia University. The first individual I must thank my adviser, Dr. Fabien Goulay. His sage-like patience and prompt responses to my requests and questions made my time at graduate school much smoother. While I have always been good at foreseeing what problems may appear when tackling a new problem, I am not always so adept at finding solutions to those problems. His differing approach to addressing problems is something that I have learned much from and hope to take to all of my future ventures. I will always be grateful for his guidance and appreciative of the time I have spent working with him.

I would like to thank the faculty of Allen, Sherman, and Randy in the material shop who helped with the construction of the parts needed for my research to progress, as well Greg Lusk for helping with any electronic and programming difficulties I had encountered. Without their dedication to their work, I would not have been able to conduct the research I needed to during my time in graduate school. I am also extremely grateful Dr. Selby for her collaborative efforts and support throughout the years. Reliable both in and outside of the lab, I can only hope that I can take much of her knowledge and skills to my future work. To all of the other staff and faculty at WVU, I thank you for the help and guidance you have provided me over the years.

Perhaps the support came from my family, who supported me throughout all of my years of graduate school. I would not have been able to make it through the trials of graduate school without the support from my family. I would like to thank both my mother and father, Myung and Sang Lee, for showing me support in your own personal ways. I have always tried to

take the best qualities of both of you and embody them as best as I can. I would like to thank my brother, Willey Lee, who I can rely on to keep me grounded in my thoughts through our conversations. I hope I can support you in your future ventures, wherever they may take you.

Finally, I would like to express my heartfelt gratitude to all of my friends who helped keep me sane during the tougher times. Thank you to Tudor Crihalmeanu who kept me honest by being my gym partner for much of graduate school. Thanks to Steven Knowlden of the Popp group, who provided me with a lot of laughter during my graduate career. I would also like to thank my group members of Kacee Caster, Tadini Masaya, Susith Pathmasiri, and Patrick Rutto for all of your help and support during graduate school.

Table of Contents

Abstract.....	i
Acknowledgements.....	iv
List of Tables	ix
List of Figures	x
List of Schemes.....	xiii
List of Symbols and Abbreviations	xiv
Chapter 1: Introduction	1
1.1 Carbon growth environments.....	1
1.2 Combustion.....	2
1.3 Polycyclic Aromatic Hydrocarbons.....	2
1.4 Carbon Growth Scheme	3
1.5 Resonantly Stabilized Radicals	5
1.6 The OH Radical.....	8
1.7 The CN Radical	10
1.8 The Propargyl Radical.....	10
1.9 Laval Nozzles	11
1.10 High Temperature Radical Reaction Studies.....	14
1.11 Purpose of research	17
1.12 Significance of Research.....	18
1.13 References	19
Chapter 2: Experimental and Methods.....	31
2.1 High-Temperature Fast-Flow	31

2.2	Validation of Flow Conditions	39
2.2.1	Pitot Tube Measurements	39
2.3	Temperature Determination of the High-temperature Flow	44
2.4	Kinetic and Product Detection Studies	45
2.5	Quasi-Static Reaction Cell	46
2.6	Pulsed Laser Photolysis/Laser-Induced Fluorescence	47
2.7	Pseudo-First Order Kinetics	49
2.8	CN Radical as a Temperature Proxy	51
2.8.1	PGOPHER Simulations and Fitting of Experimental Spectra	51
2.9	Computational Methods	54
2.10	MESMER	55
2.11	Product Detection Experiments	56
2.12	Multiplexed Photoionization Mass Spectrometry (PIMS)	57
2.14	3D Data Collection	58
	References	60
	Chapter 3: Reaction of the CN $X^2\Sigma^+$ ($v'' = 0$) Radical with 2-methylfuran	63
3.1	Generation of the CN Radical	63
3.1	CN Radical + 2-Methylfuran Kinetic Study	64
3.2	Fluence Dependence	65
3.3	Pressure and Temperature Dependence	67
3.4	CN ($B^2\Sigma^+$) + 2-methylfuran Potential Energy Surface	68
3.5	Discussion of Reaction Characteristics	70
3.6	Conclusion	74
3.7	References	77
	Chapter 4: OH + Propargyl Radical Reaction	79
4.1	OH + Propargyl Radical	79
4.2	Potential Energy Surface of the OH + Propargyl Radical Reaction	80

4.3 Photodissociation of Propargyl Chloride at 193 nm	83
4.4 Addition of OH	86
4.4.1 <i>M/z</i> 56 Isomers at 298 K	86
4.4.2 High Signal Masses	87
4.4.3 Determination of Branching Ratios of the Products of the OH + Radical Reaction	88
4.4.4 500 K Reaction Conditions	90
4.5 Discussion	91
References 4.7	93
Chapter 5: Concluding Remarks	94
References	96
Appendix	97

List of Tables

Table 3.1. Abstraction pathways for the CN + 2-methylfuran reaction with corresponding enthalpies

Table 4.1. Table of experimentally validated species and their relative branching ratios at 298 K and 4 Torr.

List of Figures

Chapter 1: Introduction

Figure 1.1 Schematic of the growth and formation of carbon particles in premixed flames. Image taken from Richter and Howard.³

Chapter 2: Experimental Methods

Figure 2.1. Schematic of the high-temperature pulsed flow reactor. Temperatures of up to 750 K are attainable for the purpose of kinetic and product detection studies

Figure 2.2. Mach and temperature profiles along the length of the Laval nozzle depicting the vertical shockwave.

Figure 2.3. Boundary layer formation after supersonic expansion through a standing normal shockwave, resulting in a subsonic, high-temperature flow

Figure 2.4. Kinetic experimental timing for the high-temperature fast-flow cell.

Figure 2.5. Pitot tube insert used to measure the impact pressure of the flow at subsonic and supersonic conditions.

Figure 2.6. Bow shock formation at the entrance of a pitot tube due to supersonic gas flow

Figure 2.7. Mach number profile as a function of distance from the exit of the nozzle at 450 K reservoir temperature, 4 SLM flow rate, and 60 Torr reservoir pressure. The horizontal blue line is the minimum expected Mach number after the gas has undergone supersonic expansion and passed through the shockwave.

Figure 2.8. Time-resolved pressure measurements of the pitot tube at 750 K and 4 SLM total flow as a function of the throttled back pressure of the cell. Establishment of flow conditions can be seen at approximately 3.5 – 4 Torr back pressure.

Figure 2.9. Schematic of the multiplexed photoionization mass spectrometer at the Advanced Light Source. Image source from Osborn et al.⁴

Figure 2.10. Schematic of the quasi-static reaction cell used in the CN determination of temperature by CN rovibrational excitation as well as the kinetic study of CN + 2-methylfuran

Figure 2.11. Rovibrational transition from the $v=0$ state to $v = 1$

Figure 2.12. CN LIF-signal temporal trace at different 2-MF number densities as follows: 0.0 molecules cm^{-3} (light green), 2.4×10^{13} molecules cm^{-3} (brown), 2.9×10^{13} molecules cm^{-3} (purple), 4.3×10^{13} molecules cm^{-3} (blue), 5.7×10^{13} molecules cm^{-3} (dark green), 7.1×10^{13} molecules cm^{-3} (red), 8.5×10^{13} molecules cm^{-3} (black). The lines are exponential fit to the experimental data from 30 to 600 μs .

Figure 2.13. Experimental (top) and simulated (bottom) CN LIF spectrum of the R-branch of the $B^2\Sigma^+, v = 0 \leftarrow X^2\Sigma^+, v = 0$ transition. The CN radical is produced from the photolysis of ICN at 266 nm in Ar at 5 Torr and detected at 420 nm. The simulation returns a rotational temperature of 440 K.

Figure 2.14. Temperature characterization of the quasi-static small cell using PGOPHER fits of experimental rovibronic spectra of the CN radical.

Figure 2.15. Schematic of MESMER probability calculations. Variables such as the energy of the species, temperature of the gas, and affect of the bath gas are taken into account to determine the probabilities of proceeding down certain reaction pathways.

Figure 2.16. Schematic of the multiplexed photoionization mass spectrometer at the Advanced Light Source. Image source from Osborn et al.⁵

Chapter 3. Temperature Validation Experiments with the CN Radical

Figure 3.1. Pseudo-first order rate coefficients of the CN + 2-MF reaction as a function of 2-MF number density at 304 K and 5.34 Torr. The vertical error bars are reported to 2σ . The black solid line is a linear fit of k_{1st} values resulting in a 2nd order rate coefficient

Figure 3.2. Second order rate coefficients of the CN + 2-Methylfuran reaction as a function of laser fluence at 304 K and 5.34 Torr. The vertical error bars are reported to 2σ .

Figure 3.3. Second order rate coefficients of the CN + 2-Methylfuran reaction as a function of pressure at 304 K. The vertical error bars are reported to 2σ .

Figure 3.4. Second order rate coefficients of the CN + 2-methylfuran reaction as a function of temperature at 5.44 Torr. The vertical and horizontal error bars are reported to 2σ precision.

Figure 3.5. A portion of the CN + 2-MF potential energy surface for addition of the CN radical onto 2-methylfuran unsaturation.

Figure 3.6. Experimental bimolecular rate constants of CN vs. temperature for selected hydrocarbons.

Chapter 4: OH + Propargyl Radical Reaction

Figure 4.1. Potential Energy Surface for the molecular exit channels (top) and radical exit channels (bottom) adapted from Pham et al.

Figure 4.2. Mass spectrum of the photodissociation of C_3H_3Cl with the photoionization spectrum of the propargyl radical.

Figure 4.3. Depletion of m/z 39 with and without the OH radical coincidental with the m/z 56 signal increase

Figure 4.4. Photoionization spectrum (open circles) of m/z 78 ion signal obtained by photolysis of C_3H_3Cl and urea-peroxide complex integrated over 0-80 ms time range. The green line shows the three isomers of acrolein, allenol, and cyclopropanone that were fit to the experimental spectrum. Branching fractions are obtained based on the weighted fit of the m/z 56 signal.

Figure 4.5. Absolute and calculated photoionization spectra of the potential isomers of m/z 56. Franck-Condon factors are calculated using the Gaussian⁶ suite of programs for cyclopropanone and propargyl alcohol. Allenol, acrolein, and methylketene absolute photoionization cross sections are experimentally determined by Savee et al.⁷

Figure 4.6. Fit of the radical signal at m/z 29. S'_i is the amount of precursor consumed, $c_{1,i}$ is the pseudo first-order rate coefficient for the formation of species "i", $c_{2,i}$ is the pseudo first-order rate coefficient for loss of the radical signal, and t is the reaction time. The fit to function allows determination of the theoretical radical signal without the radical decay.

Figure 4.7. Fit of the m/z 56 signal at 500 K with the weighted cross sections of

Appendix

Figure A1. Mass spectrum of $C_3H_3Cl + HOOH$ at 500 K

Figure A2. Photoionization spectrum of m/z 28 of the $C_3H_3Cl + HOOH$ reaction superimposed on the photoionization spectrum of ethylene

Figure A3. Photoionization spectrum of m/z 29 of the $C_3H_3Cl + HOOH$ reaction superimposed on the photoionization spectrum of the HCO radical

Figure A4. Photoionization spectrum of m/z 42 of the $C_3H_3Cl + HOOH$ reaction superimposed on the experimental spectrum of ethenone and ethynol

Figure A5. Photoionization spectrum of m/z 52 of the $C_3H_3Cl + HOOH$ reaction superimposed onto the experimental photoionization spectrum of propadienone and the PEPICO spectrum of 2-propynal

List of Schemes

Scheme 1.1 Formation of naphthalene from benzene via the HACA mechanism. Image from J. Lahaye, Mechanisms of soot formation.⁸

Scheme 1.2. Resonantly stabilized radical self-reaction to form polycyclic aromatic hydrocarbons (PAHs).⁹

Scheme 1.3. Hydroxyl radical reaction pathways of abstraction (i), addition (ii), and association (iii).

List of Symbols and Abbreviations

2-MF	2-Methylfuran
Ar	Argon
cm ⁻³	Cubic Centimeters
CRESU	Cinétique de Réaction en Ecoulement Supersonique Uniforme (Reaction kinetics in uniform supersonic flow)
DG535	Digital Delay/Pulse Generator
eV	Electron volts
FTIR	Fourier transformed Infrared spectroscopy
HACA	Hydrogen-Abstraction-C ₂ H ₂ -Addition
HAMA	Hydrogen-Abstraction-Methyl-Addition
HAVA	Hydrogen-Abstraction-Vinyl-Addition
ICN	Iodine Cyanide
INT	Intermediate
K	Kelvin
L	Liter
LIF	Laser-Induced Fluorescence
M	Mach number
ME	Master Equation
MESMER	Master Equation Solver for Multi-Energy Well Reactions
Mb	Megabarn
<i>m/z</i>	Mass-to-charge ratio
Nd:YAG	neodymium-doped yttrium aluminum garnet
ns	nanoseconds
PAH	Polycyclic Aromatic Hydrocarbon
PES	Potential Energy Surface
PIMS	Photoionization mass spectrometry

PLP	Pulsed laser photolysis
PMT	Photomultiplier tube
RSR	Resonantly Stabilized Radical
Slm	Standard liters per minute
SRS	Stanford Research Systems
TMC-1	Taurus molecular cloud 1
TOF-MS	Time-of-Flight Mass Spectrometer
VOC	Volatile Organic Compound
VUV	Vacuum Ultraviolet
μs	microseconds

Chapter 1: Introduction

1.1 Carbon growth environments

Carbon growth is not well understood but is present in many environments. The process is involved in the formation of aerosol particles in the atmosphere,^{1, 10, 11} the growth of carbon species in cold dark clouds in the interstellar medium,^{3, 4, 12} and the combustion and formation of polycyclic aromatic hydrocarbons from carbon-based fuels. These growth processes are difficult to study, leading to many of these pathways being unknown or ill-defined.

The most well-known process involving carbon growth is combustion, specifically the burning of fossil fuels. Burning of fossil fuels still comprises the vast majority of society's energy production.³ While they may take different forms such as gasoline or natural gas, ultimately are all burned to produce energy. Despite the prevalence of combustion as a means of producing energy, it is a very inefficient process when considering the total energy inside of the fuel. When considering car engines, for example, only 12% - 30% of the energy from the fuel is used to move the vehicle¹³. While some of the losses come from unavoidable conditions such as braking or wind resistance, combustion inefficiencies represent a significant and solvable portion of the inefficiency present. Much of these inefficiencies are locked behind the carbon growth that occurs during the combustion of hydrocarbon fuels.

New technologies are constantly being developed for the purpose of studying these carbon growth processes. Improved spectroscopic techniques have allowed for the discovery of many more organic species in the interstellar medium,¹¹ giving greater insights into the formation and growth of prebiotic chemical species that may have given way to the formation

of life. Recent studies have even shown the presence of the propargyl radical, a radical of vital importance in combustion research¹⁴⁻¹⁶ in TMC-1, an interstellar cold, dark cloud.¹⁷ This discovery highlights some of the commonality between different fields of research, the broad reaching applications of the experimental techniques used to study them, and the importance of understanding the exact mechanisms of carbon growth. Many of these studies then pave the way for innovation built on the knowledge obtained from the studies such as a study done on the supercritical processing/combustion of biodiesel fuels leading to reduced particle emission, leading to cleaner combustion.¹⁶

1.2 Combustion

The process of combustion involves the oxidative chain reaction of a fuel. This chain reaction results in a release of energy accompanied by high-temperatures and increases in pressure. The heat and pressures produced by these reactions power the industries and engines that power society. The complete combustion of fuels has few products, only producing $\text{H}_2\text{O} + \text{CO}_2$. Unideal conditions during combustion, such as a lack of oxygen or lower temperatures, lead to incomplete combustion, and ultimately lead to the formation of unwanted byproducts such as carbon particles in the form of soot and other volatile organic compounds (VOCs), many of which are eventually released into the environment. Not only are these harmful byproducts produced in these cases, but the energy which should be powering engines and factories become locked inside of the bonds of these byproducts and are ultimately never burned.

1.3 Polycyclic Aromatic Hydrocarbons

Polycyclic aromatic hydrocarbons (PAHs) are formed due to successive reactions that occur in unideal combustion environments. These PAHs are known to be the precursors to formation of

larger carbon nanoparticles in carbon-rich environments such as flames^{18, 19-21} and the interstellar medium.^{4, 21} Resonantly stabilized are of particular note in the formation of PAHs as they are more stable due to their resonance structures, and therefore are more likely to accumulate in combustion systems. These radicals can self-react or react with other RSRs to form ring structures with very few steps. During combustion process, many intermediate species are formed as part of the chain reaction. These intermediate species can include free atoms such as H, hydrocarbons, free radicals such as OH, and resonantly stabilized radicals (RSRs). After formation, these PAHs can aggregate to form larger systems of PAHs, which can nucleate on dust or other fine particles to form carbon nanoparticles such as soot. These PAHs have been classified as a pollutant,¹⁰ are known to be harmful to humans,²² and are well known to be present in combustion.¹⁰

1.4 Carbon Growth Scheme

The formation of PAHs begins when the pyrolysis and oxidation of fuel proceeds through the chain reaction to form small radicals. Small radicals such as H, O, OH, and CH propagate the chain reaction and lead to the combustion of the fuel, shown in figure 1.1. Many of these radicals, due to lack of ideal combustion conditions, can react, leading to molecular growth. The formation of the first aromatic ring or rings (benzene, naphthalene, anthracene) is thought to be a rate limiting step in the overall combustion scheme, as these are thought to then further aggregate to form soot.^{3, 12, 23, 24}

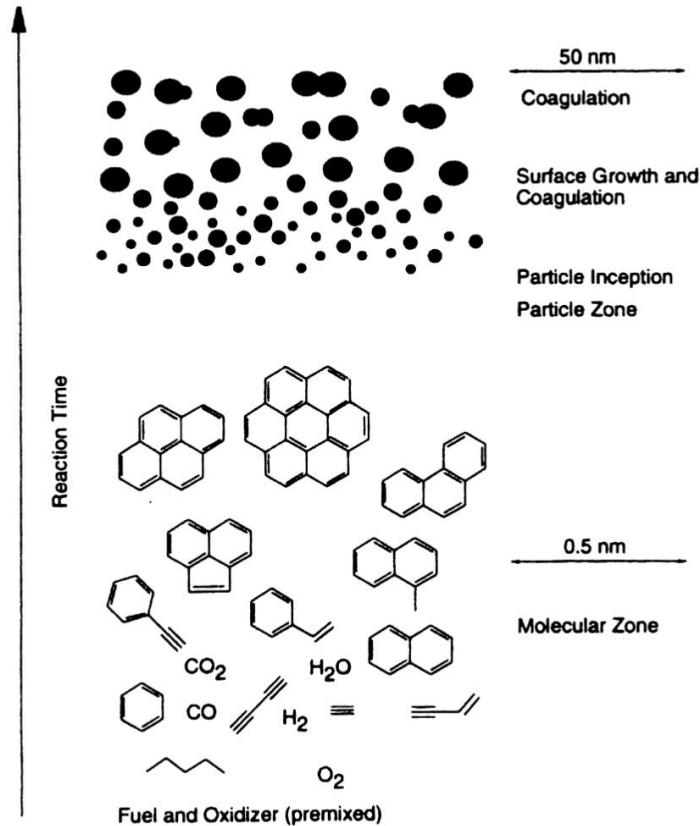
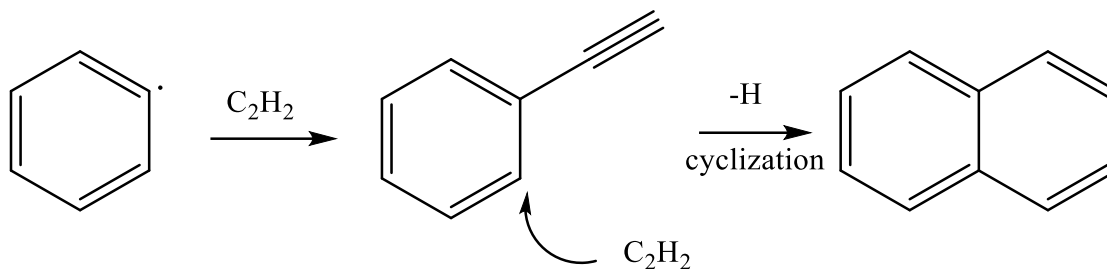


Figure 1.1 Schematic of the growth and formation of carbon particles in premixed flames. Image taken from Richter and Howard, *Prog. Energy Combust. Sci.*, 2003.¹

There are a few pathways that can lead to the formation of PAHs. Besides the direct reaction of resonantly stabilized radical species with itself and other RSRs, the most commonly accepted of growth are the HACA (Hydrogen-Abstraction-C₂H₂-Addition) and HAMA (Hydrogen-Abstraction-Methyl-Addition), HAVA (Hydrogen-Abstraction-Vinyl-Addition), among many others.^{25, 26, 27} As their name suggests, these processes involve the removal of a hydrogen atom from a molecule, likely a resonantly stabilized radical, and the subsequent addition of a C₂H₂ (in the case with HACA), a methyl group (in the case with HAMA), or a vinyl group (in the case with HAVA). These processes most often begin with single aromatic rings such as benzene and

repeat until the addition site closes in to form another ring. Scheme 1.1 depicts a schematic of the HACA mechanism starting from a benzene with an abstracted hydrogen.



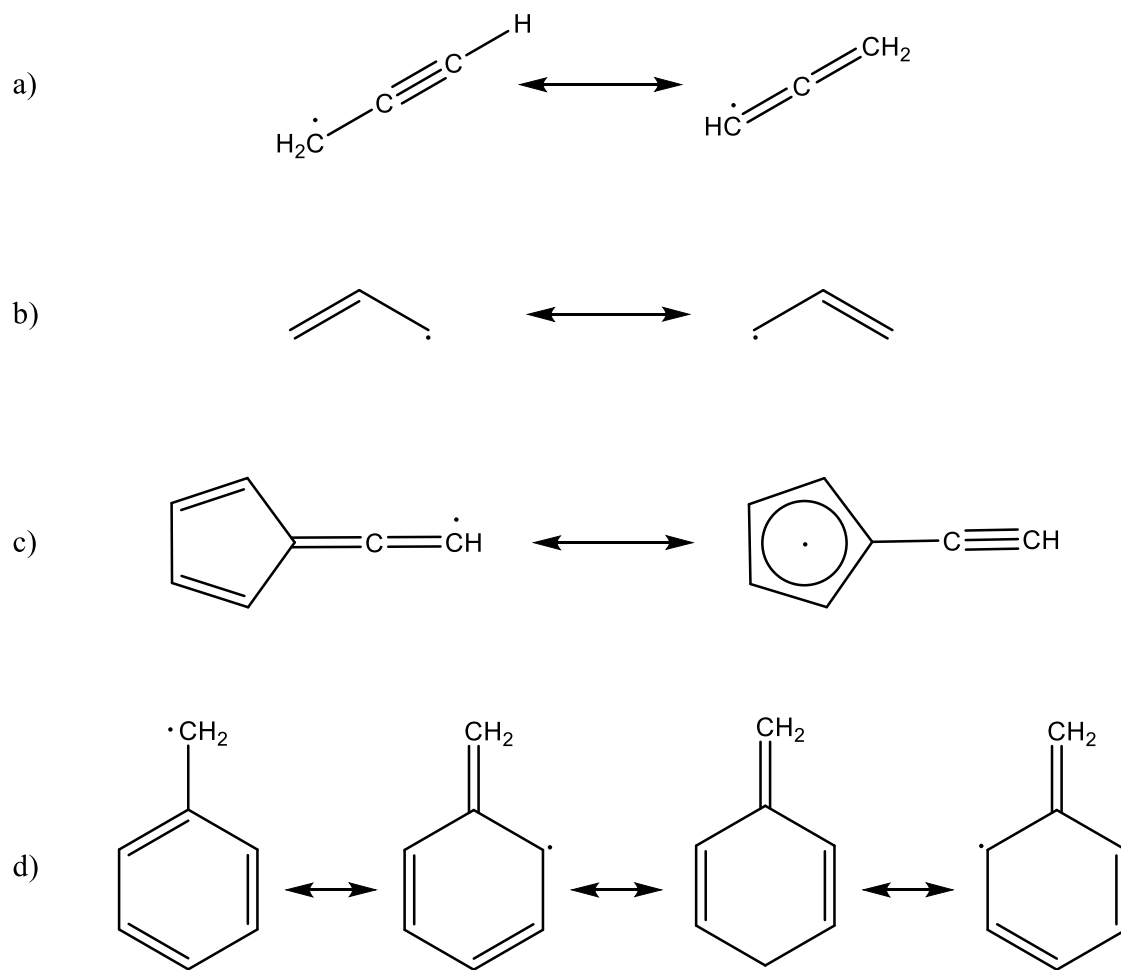
Scheme 1.1 Formation of naphthalene from benzene via the HACA mechanism. One H atom is abstracted from the benzene, allowing addition of the C_2H_2 addition to the radical site. Subsequent additions allow for ring closure.

After the initial abstraction of a hydrogen from the aromatic ring by another radical, acetylene (C_2H_2) adds to the radical site until a hydrogen atom is ejected and the ring closes. The exact mechanism by which subsequent rings are formed can depend on the species that is being added to. For example, the HACA mechanism is resistant to the formation of cyclopentaring-fused species such as acenaphthylene ($C_{12}H_8$), whereas the HAVA mechanism may be more favorable to such products due to the nature of their respective structures.²⁸

1.5 Resonantly Stabilized Radicals

Resonantly stabilized radicals have long since been theorized to be an important part in the formation of PAHs. These species must be stable enough to accumulate in combustion zones, yet reactive enough to quickly form ring species. Resonantly stabilized radicals are more stable than their alkyl radical counterparts due to resonance-stabilization. The resonance forms of select radicals are shown in scheme 1.2. This stability increases the likelihood that they will accumulate in reaction zones and play important roles in the initial formation of PAHs. Many of these resonantly stabilized radicals, such as propargyl (C_3H_3),^{29, 30, 31, 32} allyl (C_3H_5),³³

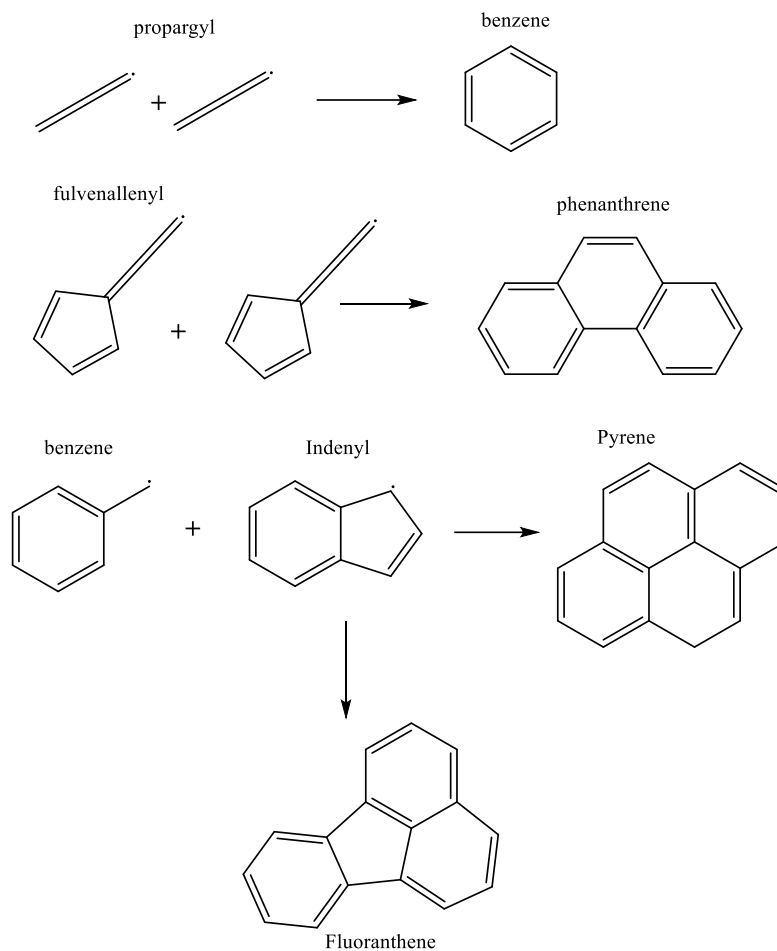
fulvenallenyl (C_7H_5),³⁴ and benzyl (C_7H_7),³⁵ are well known to exist in combustion environments and have been studied extensively. Their unsaturated structure makes them key species for study when trying to find which species are responsible for the formation and propagation of PAHs. Many of the resonantly stabilized radicals are known to react with itself, other radicals, or other molecules to form PAHs, shown in scheme 1.3. Resonantly stabilized radicals must be unreactive enough to accumulate in solution, yet reactive enough to quickly proceed down these molecular growth pathways. Because of their importance in the formation of PAHs, it is important to understand their role in combustion schemes. Determining their role in the formation of these PAHs, as well as how all the relevant reactions that consume them will add to existing models of these systems.



Scheme 1.2. Resonance structures for propargyl (a), allyl (b), fulvenallenyl (c), and benzyl (d) radicals.

A common pattern among these small resonantly stabilized radicals is their weak association with molecular oxygen.^{36, 37} The weaker interaction between this common oxidant and resonantly stabilized radicals often lead to dissociation back into RSR and O₂. Studies done by Zador et al.³⁸ shows a smaller potential energy well for the R-O₂ bond, causing a reduced amount of isomerization to peroxy radicals when compared to its alkyl counterparts. The reduced reactivity stems from the loss of resonance stabilization due to the initial bond formation with the RSR and O₂, increasing the barrier to reaction. Instead of reaction with O₂, it

is believed that the primary method by which these RSRs are consumed in reactions are through reactions with other radicals, such as the case of self-reaction, or with other small radicals such as OH, and OH₂.



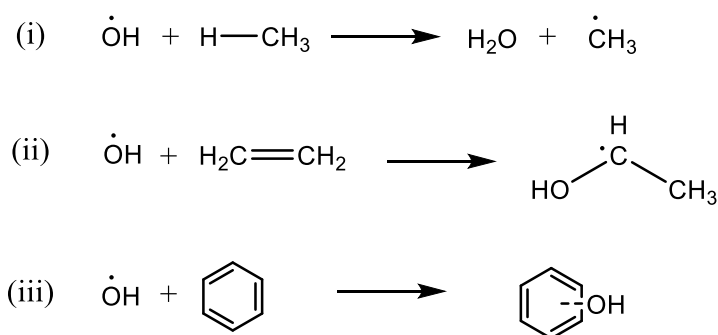
Scheme 1.3. Resonantly stabilized radical self-reaction to form polycyclic aromatic hydrocarbons (PAHs).³⁹

1.6 The OH Radical

Small radicals are essential in the propagation of chain reactions in systems like those in combustion or the atmosphere.^{19, 25, 27, 29, 40-42} Radicals such as OH, CH, and CN are important species in the propagation of reactions and the formation of important species in these environments. Such radicals can be detected spectroscopically, and their rates of reaction with

organic species of interest have long been studied.^{33, 37, 43} The OH radical in particular has long been studied as one of the most powerful oxidizing agents in many different systems and has been studied extensively.^{35, 36, 44, 45} The OH radical is known to participate in a multitude of chemical systems such as the oxidation of many different pollutants,³¹ oxidation of fuel hydrocarbon species in flames,³⁷ and oxidation of atmospheric organic species.¹⁶

The OH radical reacts through three main processes, those being the processes of abstraction, association, and addition, depicted in Scheme 1.4. Abstraction^{10, 15} is the most common mechanism of reaction, as it is the only possible mechanism when OH reacts with a saturated hydrocarbon. In this process, the OH radical abstracts a hydrogen atom from an organic species to form water and a new organic radical. The new organic radical species can then go on to propagate other reaction mechanisms. The second method by which the OH radical reacts is by addition onto an unsaturated carbon, creating an oxygenated radical. The third pathway of reaction for the OH radical is the formation of an association adduct, which can be stabilized given enough pressure. The adduct can then react and isomerize or undergo elimination reactions to form new oxygenated species.



Scheme 2.4. Hydroxyl radical reaction pathways of abstraction of a hydrogen atom (i), addition (ii) into a double bond, and association with the (iii).

1.7 The CN Radical

The CN radical has been detected in nitrogen-containing flames and engines burning nitrogenated fuels.⁴⁶ It has been identified as an important precursor in NO_x formation,⁴⁷ which subsequently can form HCN by reaction of NO_x with small hydrocarbon radicals in flames.⁴⁸ Rates coefficients for reactions involving the CN radical and unsaturated hydrocarbons have been shown to often have a small negative temperature dependence⁴⁹ due long-range interactions or the formation of pre-reaction complexes along the dominant reaction pathways. These complexes precede the activation energy barrier of any of the entrance channels on the reaction coordinate and influence the most likely reaction pathway.⁵⁰⁻⁵² These types of complexes have been found to play a significant role during the reactions of both the OH⁵³ and CN^{51, 54, 55} radicals with hydrocarbons and are shown to dissociate more readily at higher temperatures. H atom abstraction pathways of the reaction between CN and unsaturated hydrocarbons are most often endothermic with large activation energies and are not believed to be major contributors to the combustion models.^{41, 56}

1.8 The Propargyl Radical

The propargyl radical is the simplest resonantly stabilized radical and has garnered particular attention due to its ability to self-react and form benzene.^{10, 57, 58} The propargyl radical has been seen in many carbon-rich environments such as flames, planetary atmospheres, and interstellar media.^{10, 58} As the formation of the first ring is thought to be a key rate-limiting step in the carbon growth scheme, the measurement of its reaction rate with other radicals was of particular importance. In addition to self-reaction to form benzene, it has also been shown to be capable of forming larger multi-ring PAHs by adding to species such as naphthalene. The

propargyl radical also unique among radicals in that its free electron is spread out over two sites in the radical, leading to possible reactions with the “head” (the -CH₂ site) or “tail” (the -CH site). This possibility of two reactive sites has great implications for the possible products of reactions involving the propargyl radical.

Because the propargyl radical has been shown to be such an important species in the carbon growth scheme, it is important to study the species that react with the propargyl radical, as well as the rates of those reactions. Since the propargyl radical does not form strong associations with molecular oxygen, it is necessary to look to reactions with other radicals such as OH for the pathway by which the propargyl radical is consumed in combustion systems. Such reactions involving two radicals are extremely difficult to study due to their reactive nature, leading to lack of information regarding their properties.

1.9 Laval Nozzles

To understand the experimental apparatus discussed in this work and the attaining of higher experimental temperatures, it is necessary to understand principles that allow the CRESU technique to create low temperature and pressure experimental conditions⁵⁸. The CRESU technique creates a uniform, supersonic jet of gas generated by isentropic expansion of a gas by Laval nozzles. The resulting jet of gas is uniform in its Mach number (M), temperature (T), and pressure (P). The uniformity in experimental conditions is due to the specificity of the Laval nozzle, the geometry of which is dependent on the buffer gas used, the reservoir temperature, the flow pressure, and the Mach number^{3, 59}. Due to this, only one set of conditions is possible to be accurately used for any given Laval nozzle. At the low temperatures that the CRESU experiment is used for, an extraordinary amount of pumping power is necessary to maintain

uniform, isentropic “core” in the middle of the resulting gas flow. This isentropic “core” at the center of the gas flow is essential to the use of the CRESU experiment, as its uniformity is what allows measurements for values like rate coefficients to be valid.

An isentropic flow is a flow where the value of entropy remains constant. As a gas of predetermined temperature and pressure is forced through a tube, the density of the gas remains largely constant, but the flow speed increases. However, when the gas approaches the speed of sound, the compressibility effects of the gas must be considered. When the gas is then forced through a Laval nozzle with sufficient force, the resulting total entropy of the flow remains the same as prior to entering the Laval nozzle due to the gradual compression and expansion due to the change in diameter of the flow. When this threshold is reached the flow becomes “choked,” meaning the speed of the gas where the converging part of the nozzle meets the diverging part, and the speed of the gas after expansion becomes supersonic. Before defining the isentropic flow equations, it is necessary to define some elementary terms that are integral to understanding isentropic flow. The equations for speed of sound (a) and the Mach number (M), as shown in Eq. 1.1 and 1.2 below:

$$a = \sqrt{\gamma \frac{p}{\rho}} = \sqrt{\gamma RT} \quad (1.1)$$

$$M = \frac{v}{a} \quad (1.2)$$

For Eq. 1.2, γ is the specific heat ratio of the gas, p is the reservoir static pressure, or pressure prior to expansion, and ρ is the density of the gas. The ratio of pressure to density can be rewritten in the form of RT , where R is the gas constant from the equations of state, and T

is the temperature. The Mach number equation is shown as a ratio of the velocity (v) and the speed of sound (a).

The total pressure (p_t), which is the pressure when the flow is brought isentropically to rest, and the dynamic pressure (q), or pressure after the nozzle, is defined as follows:

$$\frac{p}{p_\gamma} = \frac{p_t}{p_t^\gamma} \quad (1.3)$$

$$q = \frac{\rho v^2}{2} = \frac{\gamma p M^2}{2} \quad (1.4)$$

It is then possible to define the isentropic flow equations, which are shown in the equations below:

$$\frac{p}{p_t} = \left(1 + \frac{\gamma-1}{2} M^2\right)^{\frac{-\gamma}{\gamma-1}} \quad (1.5)$$

$$\frac{T}{T_t} = \left(1 + \frac{\gamma-1}{2} M^2\right)^{-1} \quad (1.6)$$

The final equation is of particular importance for understanding the temperature of the flow. The nozzle for a CRESU experiment is constructed using these properties. The flow conditions are also validated using these same properties. Measurement of the pressure within the flow yields the temperature of the flow. Uniformity of the flow conditions are checked by measurement of the pressure in the flow at different distances from the exit of the nozzle.

1.10 High Temperature Radical Reaction Studies

One of the most important, if not the most important, parameter to consider when studying a radical reaction is the temperature. This is especially true when discussing reactions related to cold temperatures of the interstellar medium or the high temperatures of combustion. The rates of reactions, species produced, and reaction mechanisms will differ greatly depending on the temperatures of the system. For astrochemical studies, it is important to reach temperatures low enough to accurately depict the conditions that the species of interest will experience in space. To that end, many experimental devices and techniques have been developed to accurately study these species and the reactions that they undergo. One popular method to attain the low temperatures of the vacuum of space is the CRESU (Cinétique de Réaction en Ecoulement Supersonique Uniforme), shown in Figure 1.2. It involves the acceleration of gas through a convergent-divergent nozzle, also known as a Laval nozzle, which allows for the creation of a uniform, supersonic, collision free molecular beam that attains temperatures as low as 10K.^{4, 8, 10, 22, 57} The cold temperatures and low pressures attained in this experimental flow tube allows for accurate measurements and depiction of species in the interstellar medium.

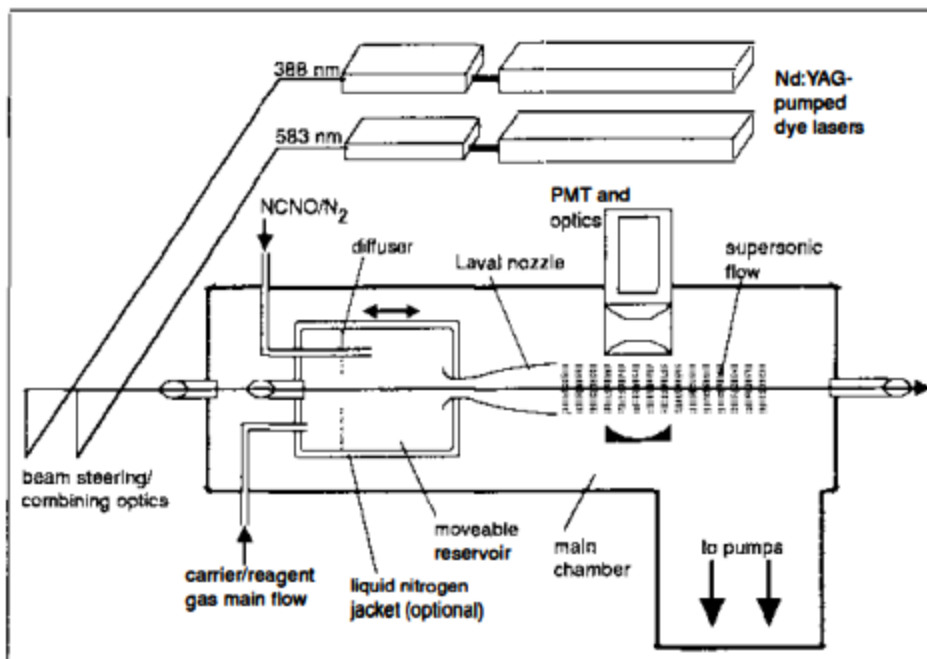


Figure 1.2. Schematic of the CRESU apparatus coupled with the PLP-LIF technique. Image taken from Sims and Smith, *Annu. Rev. Phys. Chem.*, 1995.⁶⁰

On the other end of the temperature spectrum, shock tubes are widely used to study high-temperature gas-phase reactions and is often coupled with laser spectroscopy techniques.^{61, 62} A schematic of the basic principle of a shock tube is depicted in figure 1.3. The apparatus is essentially a long tube with two sections divided by a diaphragm. One section of the tube holds the gas species of interest, while the other section is pressurized to create a large pressure differential between the two sections. The diaphragm is then removed or burst, causing a shockwave to expand towards the gas of interest, enabling high temperatures and pressures representative of combustion environments.⁶³ In addition to shock tubes, flow tubes have been used for a comparatively longer time, as the simple design of a flow tube with heated walls allow for ease of setup and construction for many groups performing research. As new discoveries and insights of molecular growth are made, new and innovative experimental

techniques will need to be made as well to accommodate the experimental needs. This method of studying high-temperature reactions comes with some disadvantages. While RSRs have been detected in shock tubes by precursor pyrolysis,⁶⁴ their exact properties are difficult to disentangle from the complex systems that are formed inside of shock tubes. Their reaction rate coefficients are often obtained by fitting the depletion of the precursor molecule signal or final product concentrations without direct measurement of the radicals themselves. Many shock tubes also have poor repeatability and difficulty in studying species with short lifetime.

Among reactions that are important to combustion, radical-radical reactions are of particular interest in recent years. These reactions are also particularly difficult to study for a multitude of reasons. The species themselves are extremely reactive, resulting in many side products being formed during experiments. Wall reactions are an especially difficult obstacle, as reaction between the walls and radical species will comprise a substantial portion of the measured rate coefficients. Achieving pseudo-first order conditions also proves a challenge due to difficulties in choosing precursors and radical production methods that provide the exact concentrations that are needed. An experimental apparatus will be discussed in this work that aims to resolve many of the issues that are present with modern-day shock tubes using principles that are used with the CRESU apparatus and modifying them for high-temperature use.

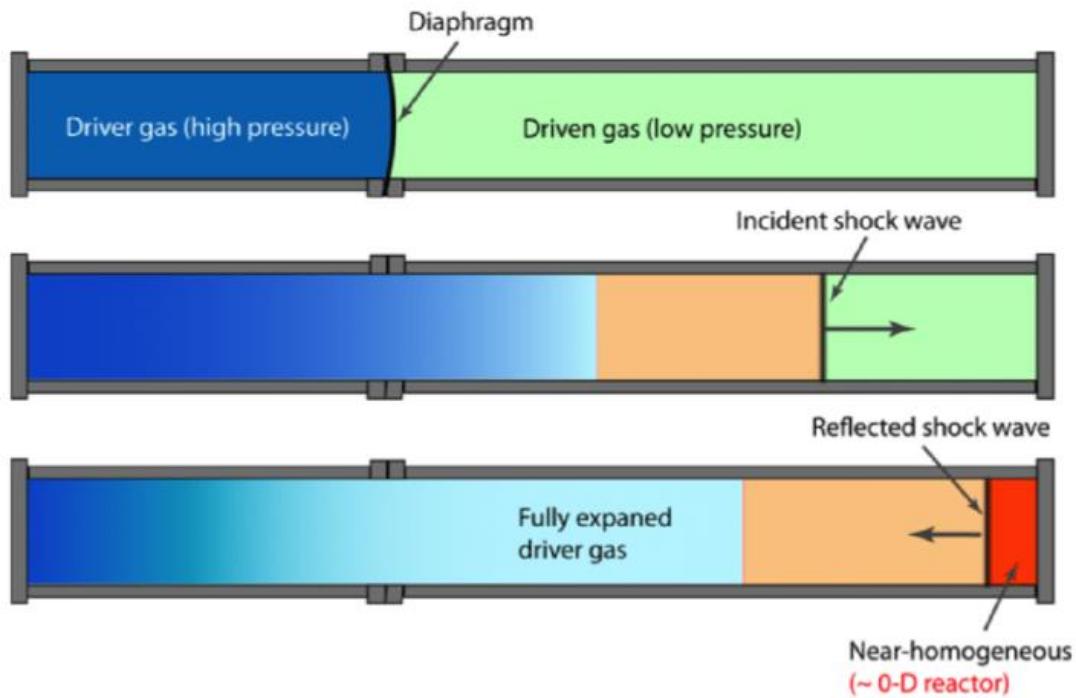


Figure 1.3. Schematic of the shock tube apparatus. The top tube depicts a shock tube prior to starting the experiment, with the reactant gas on the right and the driver gas on the left. The middle tube depicts the initiation of the experiment when the diaphragm separating the two sections is removed, creating a shockwave. The final tube depicts the established experimental condition for the shock tube. Image taken from Wang, 2016.²

1.11 Purpose of research

The aim of this work is to study the formation of the products of the OH + propargyl radical and measure the rate of reaction of the CN + 2-methylfuran reaction, as well as develop techniques to be able to study them in-house. The OH radical holds significance in combustion as the most abundant radical, as well as one of the most reactive. Because the propargyl radical plays a pivotal role in the formation of PAHs in combustion, it is necessary to determine its reaction with common radical species such as the OH radical. Other small radicals such as the CN radical hold significance in engines that use air as combustion. 2-methylfuran is a biofuel that has potential to be used as a gasoline replacement in autoignition⁶⁵ and direct injection spark engines²⁴, and therefore likely to come into contact with the CN

radical. Both of these reactions hold great importance in combustion, and their study serves to improve existing combustion models. In addition to the direct study of reactions, the development of a more robust experimental apparatus will allow a wider range of flexibility in the study of both reaction rates and the products for reactions of interest.

1.12 Significance of Research

Investigations into the product analysis of the $C_3H_3 + OH$ reaction revealed that the two radicals readily react to form products consistent with existing computational work for the reaction. There is no discernable presence of the product propargyl alcohol that would result from the OH addition to the “head” end of the propargyl radical based on photoionization spectra analysis. The smaller radical products that are formed are in good agreement with Pham and Trang,¹⁰ though additional insights are presented here as they did not consider the addition product of m/z 56 in their analysis of exit channels. Acrolein (C_3H_4O) dominates as a product in both the low and high-temperature regions studied, with the ratio of acrolein increasing with temperature.

In order to study the entirety of the $C_3H_3 + OH$ and similar reactions, a novel fast-flow apparatus is constructed to study the kinetic rate of the reaction in addition to the product analysis performed from experiments at the Advanced Light Source (ALS) at the Lawrence Berkeley National Laboratory (LBNL). This fast-flow apparatus uses similar principles of the CRESU technique but targeted for high temperatures. Obtaining kinetic data will allow more full characterizations of reactions of interest when combined with the product analysis.

1.13 References

- (1) Agúndez, M.; Cabezas, C.; Tercero, B.; Marcelino, N.; Gallego, J. D.; de Vicente, P.; Cernicharo, J. Discovery of the propargyl radical (CH₂CCH) in TMC-1: One of the most abundant radicals ever found and a key species for cyclization to benzene in cold dark clouds*. *A&A* **2021**, *647*, L10.
- (2) Slavinskaya, N. A.; Frank, P. A modelling study of aromatic soot precursors formation in laminar methane and ethene flames. *Combustion and Flame* **2009**, *156* (9), 1705-1722. DOI: 10.1016/j.combustflame.2009.04.013.
- (3) Frenklach, M.; Mebel, A. On the mechanism of soot formation. *Physical Chemistry Chemical Physics* **2020**, *22*. DOI: 10.1039/D0CP00116C.
- (4) Sinha, S.; Rahman, R. K.; Raj, A. On the role of resonantly stabilized radicals in polycyclic aromatic hydrocarbon (PAH) formation: pyrene and fluoranthene formation from benzyl-indenyl addition. *Physical Chemistry Chemical Physics* **2017**, *19* (29), 19262-19278, 10.1039/C7CP02539D. DOI: 10.1039/C7CP02539D.
- (5) Miller, J. A.; Pilling, M. J.; Troe, J. Unravelling combustion mechanisms through a quantitative understanding of elementary reactions. *Proceedings of the Combustion Institute* **2005**, *30* (1), 43-88. DOI: <https://doi.org/10.1016/j.proci.2004.08.281>.
- (6) Millar, T. J. THE CHEMISTRY OF PAH AND FULLERENE MOLECULES IN INTERSTELLAR CLOUDS. *Monthly Notices of the Royal Astronomical Society* **1992**, *259* (3), P35-P39. DOI: 10.1093/mnras/259.1.35P.
- (7) Tielens, A. The molecular universe. *Reviews of Modern Physics* **2013**, *85* (3), 1021-1081. DOI: 10.1103/RevModPhys.85.1021.
- (8) Kulmala, M.; Vehkamäki, H.; Petaja, T.; Dal Maso, M.; Lauri, A.; Kerminen, V. M.; Birmili, W.; McMurry, P. H. Formation and growth rates of ultrafine atmospheric particles: a review of observations. *Journal of Aerosol Science* **2004**, *35* (2), 143-176. DOI: 10.1016/j.jaerosci.2003.10.003.

- (9) Tobiszewski, M.; Namiesnik, J. PAH diagnostic ratios for the identification of pollution emission sources. *Environmental Pollution* **2012**, *162*, 110-119. DOI: 10.1016/j.envpol.2011.10.025. Kim, K. H.; Jahan, S. A.; Kabir, E.; Brown, R. J. C. A review of airborne polycyclic aromatic hydrocarbons (PAHs) and their human health effects. *Environment International* **2013**, *60*, 71-80. DOI: 10.1016/j.envint.2013.07.019. Qi, F. Combustion chemistry probed by synchrotron VUV photoionization mass spectrometry. *Proceedings of the Combustion Institute* **2013**, *34*, 33-63. DOI: 10.1016/j.proci.2012.09.002.
- (10) Richter, H.; Howard, J. B. Formation of polycyclic aromatic hydrocarbons and their growth to soot—a review of chemical reaction pathways. *Progress in Energy and Combustion Science* **2000**, *26* (4), 565-608. DOI: [https://doi.org/10.1016/S0360-1285\(00\)00009-5](https://doi.org/10.1016/S0360-1285(00)00009-5).
- (11) Fitzpatrick, E. M.; Bartle, K. D.; Kubacki, M. L.; Jones, J. M.; Pourkashanian, M.; Ross, A. B.; Williams, A.; Kubica, K. The mechanism of the formation of soot and other pollutants during the co-firing of coal and pine wood in a fixed bed combustor. *Fuel* **2009**, *88* (12), 2409-2417. DOI: <https://doi.org/10.1016/j.fuel.2009.02.037>.
- (12) Johansson, K. O.; Head-Gordon, M. P.; Schrader, P. E.; Wilson, K. R.; Michelsen, H. A. Resonance-stabilized hydrocarbon-radical chain reactions may explain soot inception and growth. *Science* **2018**, *361* (6406), 997-1000. DOI: 10.1126/science.aat3417 From NLM.
- (13) Parker, D. S. N.; Kaiser, R. I.; Troy, T. P.; Ahmed, M. Hydrogen Abstraction/Acetylene Addition Revealed. *Angewandte Chemie International Edition* **2014**, *53* (30), 7740-7744, <https://doi.org/10.1002/anie.201404537>. DOI: <https://doi.org/10.1002/anie.201404537> (accessed 2022/06/19).
- (14) Shukla, B.; Koshi, M. A novel route for PAH growth in HACA based mechanisms. *Combustion and Flame* **2012**, *159* (12), 3589-3596. DOI: <https://doi.org/10.1016/j.combustflame.2012.08.007>.
- (15) Rasmussen, C. L.; Skjoth-Rasmussen, M. S.; Jensen, A. D.; Glarborg, P. Propargyl recombination: estimation of the high temperature, low pressure rate constant from flame

measurements. *Proceedings of the Combustion Institute* **2005**, *30*, 1023-1031. DOI: 10.1016/j.proci.2004.08.056.

(16) Miller, J. A.; Melius, C. F. Kinetic and thermodynamic issues in the formation of aromatic compounds in flames of aliphatic fuels. *Combustion and Flame* **1992**, *91* (1), 21-39. DOI: [https://doi.org/10.1016/0010-2180\(92\)90124-8](https://doi.org/10.1016/0010-2180(92)90124-8).

(17) Emissionen der Verbrennung von Kohlenwasserstoffen. In *Technische Verbrennung: Verbrennungstechnik, Verbrennungsmodellierung, Emissionen*, Joos, F. Ed.; Springer Berlin Heidelberg, 2006; pp 591-631.

(18) Kern, R. D.; Singh, H. J.; Wu, C. H. Thermal decomposition of 1,2 butadiene. *International Journal of Chemical Kinetics* **1988**, *20* (9), 731-747, <https://doi.org/10.1002/kin.550200907>. DOI: <https://doi.org/10.1002/kin.550200907> (accessed 2022/06/19). da Silva, G.; Bozzelli, J. W. Kinetic modeling of the benzyl + HO₂ reaction. *Proceedings of the Combustion Institute* **2009**, *32*, 287-294. DOI: 10.1016/j.proci.2008.05.040. Murakami, Y.; Oguchi, T.; Hashimoto, K.; Nosaka, Y. Theoretical Study of the Benzyl + O₂ Reaction: Kinetics, Mechanism, and Product Branching Ratios. *The Journal of Physical Chemistry A* **2007**, *111* (50), 13200-13208. DOI: 10.1021/jp075369q.

(19) Burke, S. M.; Metcalfe, W.; Herbinet, O.; Battin-Leclerc, F.; Haas, F. M.; Santner, J.; Dryer, F. L.; Curran, H. J. An experimental and modeling study of propene oxidation. Part 1: Speciation measurements in jet-stirred and flow reactors. *Combustion and Flame* **2014**, *161* (11), 2765-2784. DOI: 10.1016/j.combustflame.2014.05.010.

(20) Thapa, J.; Spencer, M.; Akhmedov, N.; Goulay, F. Kinetics of the OH Radical Reaction with Fulvenallene from 298 K to 450 K. *The journal of physical chemistry letters* **2015**, *6*. DOI: 10.1021/acs.jpcllett.5b02417.

(21) Zádor, J.; Taatjes, C. A.; Fernandes, R. X. Kinetics of elementary reactions in low-temperature autoignition chemistry. *Progress in Energy and Combustion Science* **2011**, *37* (4), 371-421. DOI: 10.1016/j.pecs.2010.06.006.

- (22) Raj, A.; Al Rashidi, M. J.; Chung, S. H.; Sarathy, S. M. PAH Growth Initiated by Propargyl Addition: Mechanism Development and Computational Kinetics. *The Journal of Physical Chemistry A* **2014**, *118* (16), 2865-2885. DOI: 10.1021/jp410704b.
- (23) Frenklach, M. Reaction mechanism of soot formation in flames. *Physical Chemistry Chemical Physics* **2002**, *4* (11), 2028-2037, 10.1039/B110045A. DOI: 10.1039/B110045A.
D'Anna, A.; Violi, A. Detailed Modeling of the Molecular Growth Process in Aromatic and Aliphatic Premixed Flames. *Energy & Fuels* **2005**, *19* (1), 79-86. DOI: 10.1021/ef0499675.
- (24) Castaldi, M. J.; Marinov, N. M.; Melius, C. F.; Huang, J.; Senkan, S. M.; Pit, W. J.; Westbrook, C. K. Experimental and modeling investigation of aromatic and polycyclic aromatic hydrocarbon formation in a premixed ethylene flame. *Symposium (International) on Combustion* **1996**, *26* (1), 693-702. DOI: [https://doi.org/10.1016/S0082-0784\(96\)80277-3](https://doi.org/10.1016/S0082-0784(96)80277-3).
- (25) Gligorovski, S.; Strekowski, R.; Barbati, S.; Vione, D. Environmental Implications of Hydroxyl Radicals (center dot OH). *Chemical Reviews* **2015**, *115* (24), 13051-13092. DOI: 10.1021/cr500310b.
- (26) Yang, S. S.; Huang, Z. Y.; Wu, P. X.; Li, Y. H.; Dong, X. B.; Li, C. Q.; Zhu, N. Y.; Duan, X. D.; Dionysiou, D. D. Rapid removal of tetrabromobisphenol A by alpha-Fe₂O₃-x@Graphene@Montmorillonite catalyst with oxygen vacancies through peroxymonosulfate activation: Role of halogen and alpha-hydroxyalkyl radicals. *Applied Catalysis B-Environmental* **2020**, *260*. DOI: 10.1016/j.apcatb.2019.118129. Atef, N.; Kukkadapu, G.; Mohamed, S. Y.; Al Rashidi, M.; Banyon, C.; Mehl, M.; Heufer, K. A.; Nasir, E. F.; Alfazazi, A.; Das, A. K.; et al. A comprehensive iso-octane combustion model with improved thermochemistry and chemical kinetics. *Combustion and Flame* **2017**, *178*, 111-134. DOI: 10.1016/j.combustflame.2016.12.029.
- (27) Crouse, J. D.; Nielsen, L. B.; Jorgensen, S.; Kjaergaard, H. G.; Wennberg, P. O. Autoxidation of Organic Compounds in the Atmosphere. *Journal of Physical Chemistry Letters* **2013**, *4* (20), 3513-3520. DOI: 10.1021/jz4019207.

- (28) Curran, H. J. Developing detailed chemical kinetic mechanisms for fuel combustion. *Proceedings of the Combustion Institute* **2019**, *37* (1), 57-81. DOI: 10.1016/j.proci.2018.06.054.
- (29) Haynes, B. S.; Iverach, D.; Kirov, N. Y. The behavior of nitrogen species in fuel rich hydrocarbon flames. *Symposium (International) on Combustion* **1975**, *15* (1), 1103-1112. DOI: [https://doi.org/10.1016/S0082-0784\(75\)80375-4](https://doi.org/10.1016/S0082-0784(75)80375-4).
- (30) Cooke, I. R.; Gupta, D.; Messinger, J. P.; Sims, I. R. Benzonitrile as a Proxy for Benzene in the Cold ISM: Low-temperature Rate Coefficients for $\text{CN} + \text{C}_6\text{H}_6$. *The Astrophysical Journal* **2020**, *891* (2), L41. DOI: 10.3847/2041-8213/ab7a9c. Gardez, A.; Saidani, G.; Biennier, L.; Georges, R.; Hugo, E.; Chandrasekaran, V.; Roussel, V.; Rowe, B.; Reddy, K. P. J.; Arunan, E. High-temperature kinetics of the reaction between CN and hydrocarbons using a novel high-enthalpy flow tube. *International Journal of Chemical Kinetics* **2012**, *44* (11), 753-766, <https://doi.org/10.1002/kin.20730>. DOI: <https://doi.org/10.1002/kin.20730> (accessed 2022/06/21).
- (31) Atakan, B.; Wolfrum, J. Kinetic studies of the reactions of CN radicals with alkanes in the temperature range between 294 and 1260 K. *Chemical Physics Letters* **1991**, *186* (6), 547-552. DOI: [https://doi.org/10.1016/0009-2614\(91\)90465-L](https://doi.org/10.1016/0009-2614(91)90465-L).
- (32) Ochimizu, T.; Seki, K.; Yagi, M.; Halpern, J. B.; Okabe, H. Rate constants for the reactions of CN with C₆–C₈ unsaturated hydrocarbons: the relations between the reaction rates and the molecular lengths. *Chemical Physics Letters* **1999**, *313* (3), 451-455. DOI: [https://doi.org/10.1016/S0009-2614\(99\)00962-8](https://doi.org/10.1016/S0009-2614(99)00962-8).
- (33) Sims, I. R.; Queffelec, J.-L.; Travers, D.; Rowe, B. R.; Herbert, L. B.; Karthäuser, J.; Smith, I. W. M. Rate constants for the reactions of CN with hydrocarbons at low and ultra-low temperatures. *Chemical Physics Letters* **1993**, *211* (4), 461-468. DOI: [https://doi.org/10.1016/0009-2614\(93\)87091-G](https://doi.org/10.1016/0009-2614(93)87091-G).

- (34) Halpern, J. B.; Miller, G. E.; Okabe, H. The reaction of CN radicals with cyanoacetylene. *Chemical Physics Letters* **1989**, *155* (4), 347-350. DOI: [https://doi.org/10.1016/0009-2614\(89\)87167-2](https://doi.org/10.1016/0009-2614(89)87167-2).
- (35) Trevitt, A. J.; Goulay, F.; Taatjes, C. A.; Osborn, D. L.; Leone, S. R. Reactions of the CN Radical with Benzene and Toluene: Product Detection and Low-Temperature Kinetics. *The Journal of Physical Chemistry A* **2010**, *114* (4), 1749-1755. DOI: 10.1021/jp909633a.
- (36) Georgievskii, Y.; Klippenstein, S. J. Strange Kinetics of the C₂H₆ + CN Reaction Explained. *The Journal of Physical Chemistry A* **2007**, *111* (19), 3802-3811. DOI: 10.1021/jp068430k.
- (37) Lichtin, D. A.; Lin, M. C. Temperature dependence of the CN radical reactions with C₂H₂ and C₂H₄. *Chemical Physics* **1986**, *104* (2), 325-330. DOI: [https://doi.org/10.1016/0301-0104\(86\)80176-8](https://doi.org/10.1016/0301-0104(86)80176-8).
- (38) Lee, J.; Caster, K.; Maddaleno, T.; Donnellan, Z.; Selby, T. M.; Goulay, F. Kinetic study of the CN radical reaction with 2-methylfuran. *International Journal of Chemical Kinetics* **2020**, *52* (11), 838-851, <https://doi.org/10.1002/kin.21403>. DOI: <https://doi.org/10.1002/kin.21403> (accessed 2022/07/04).
- (39) Castro-Marcano, F.; Kamat, A. M.; Russo, M. F.; van Duin, A. C. T.; Mathews, J. P. Combustion of an Illinois No. 6 coal char simulated using an atomistic char representation and the ReaxFF reactive force field. *Combustion and Flame* **2012**, *159* (3), 1272-1285. DOI: 10.1016/j.combustflame.2011.10.022. Okafor, E. C.; Somarathne, K.; Ratthanana, R.; Hayakawa, A.; Kudo, T.; Kurata, O.; Iki, N.; Tsujimura, T.; Furutani, H.; Kobayashi, H. Control of NO_x and other emissions in micro gas turbine combustors fuelled with mixtures of methane and ammonia. *Combustion and Flame* **2020**, *211*, 406-416. DOI: 10.1016/j.combustflame.2019.10.012. Zhou, C. W.; Li, Y.; Burke, U.; Banyon, C.; Somers, K. P.; Ding, S. T.; Khan, S.; Hargis, J. W.; Sikes, T.; Mathieu, O.; et al. An experimental and chemical kinetic modeling study of 1,3-butadiene combustion: Ignition delay time and laminar flame speed measurements. *Combustion and Flame* **2018**, *197*, 423-438. DOI: 10.1016/j.combustflame.2018.08.006.

- (40) Stone, D.; Whalley, L. K.; Heard, D. E. Tropospheric OH and HO₂ radicals: field measurements and model comparisons. *Chemical Society Reviews* **2012**, *41* (19), 6348-6404. DOI: 10.1039/c2cs35140d.
- (41) Wang, J. L.; Xu, L. J. Advanced Oxidation Processes for Wastewater Treatment: Formation of Hydroxyl Radical and Application. *Critical Reviews in Environmental Science and Technology* **2012**, *42* (3), 251-325. DOI: 10.1080/10643389.2010.507698.
- (42) Ma, J. Y.; Minakata, D.; O'Shea, K.; Bai, L.; Dionysiou, D. D.; Spinney, R.; Xiao, R. Y.; Wei, Z. S. Determination and Environmental Implications of Aqueous-Phase Rate Constants in Radical Reactions. *Water Research* **2021**, *190*. DOI: 10.1016/j.watres.2020.116746. Yang, X. P.; Wang, H. C.; Tan, Z. F.; Lu, K. D.; Zhang, Y. H. Observations of OH Radical Reactivity in Field Studies. *Acta Chimica Sinica* **2019**, *77* (7), 613-624. DOI: 10.6023/a19030094. Jasper, A. W.; Klippenstein, S. J.; Harding, L. B.; Ruscic, B. Kinetics of the reaction of methyl radical with hydroxyl radical and methanol decomposition. *Journal of Physical Chemistry A* **2007**, *111* (19), 3932-3950. DOI: 10.1021/jp067585p. Atkinson, R.; Arey, J. Atmospheric Degradation of Volatile Organic Compounds. *Chemical Reviews* **2003**, *103* (12), 4605-4638. DOI: 10.1021/cr0206420.
- (43) Haynes, B. S. The oxidation of hydrogen cyanide in fuel-rich flames. *Combustion and Flame* **1977**, *28*, 113-121. DOI: [https://doi.org/10.1016/0010-2180\(77\)90017-7](https://doi.org/10.1016/0010-2180(77)90017-7). Martoprawiro, M.; Bacskay, G. B.; Mackie, J. C. Ab Initio Quantum Chemical and Kinetic Modeling Study of the Pyrolysis Kinetics of Pyrrole. *The Journal of Physical Chemistry A* **1999**, *103* (20), 3923-3934. DOI: 10.1021/jp984358h. Mackie, J. C.; Colket Iii, M. B.; Nelson, P. F.; Esler, M. Shock tube pyrolysis of pyrrole and kinetic modeling. *International Journal of Chemical Kinetics* **1991**, *23* (8), 733-760, <https://doi.org/10.1002/kin.550230807>. DOI: <https://doi.org/10.1002/kin.550230807> (accessed 2022/06/21). Luo, L.; Yao, W.; Liu, J.; Zhang, H.; Ma, J.; Jiang, X. Evolution of NO_x precursors of superfine pulverized coal with a fixed bed in N₂ and CO₂. *Fuel* **2018**, *234*, 263-275. DOI: <https://doi.org/10.1016/j.fuel.2018.07.037>. Moussa, S. G.; Leithead, A.; Li, S.-M.; Chan, T. W.; Wentzell, J. J. B.; Stroud, C.; Zhang, J.; Lee, P.; Lu, G.; Brook, J. R.; et al. Emissions of hydrogen cyanide from on-road gasoline and diesel vehicles. *Atmospheric Environment* **2016**, *131*, 185-195. DOI:

<https://doi.org/10.1016/j.atmosenv.2016.01.050>. Rao, V. S.; Chandra, A. K. Reactions of cyanogen radical with alkanes and an explanation for negative temperature dependence of rate constants. *Chemical Physics* **1995**, *192* (3), 247-254. DOI: [https://doi.org/10.1016/0301-0104\(94\)00401-U](https://doi.org/10.1016/0301-0104(94)00401-U). Czakó, G.; Bowman, J. M. CH Stretching Excitation Steers the F Atom to the CD Bond in the F + CHD₃ Reaction. *Journal of the American Chemical Society* **2009**, *131* (48), 17534-17535. DOI: 10.1021/ja906886z. Czakó, G.; Bowman Joel, M. Dynamics of the O(3P) + CHD₃(v_{CH} = 0,1) reactions on an accurate ab initio potential energy surface. *Proceedings of the National Academy of Sciences* **2012**, *109* (21), 7997-8001. DOI: 10.1073/pnas.1202307109 (accessed 2022/06/21).

(44) Skouteris, D.; Manolopoulos David, E.; Bian, W.; Werner, H.-J.; Lai, L.-H.; Liu, K. van der Waals Interactions in the Cl + HD Reaction. *Science* **1999**, *286* (5445), 1713-1716. DOI: 10.1126/science.286.5445.1713 (accessed 2022/06/21). Greenwald, E. E.; North, S. W.; Georgievskii, Y.; Klippenstein, S. J. A Two Transition State Model for Radical–Molecule Reactions: A Case Study of the Addition of OH to C₂H₄. *The Journal of Physical Chemistry A* **2005**, *109* (27), 6031-6044. DOI: 10.1021/jp058041a. Greenwald, E. E.; North, S. W.; Georgievskii, Y.; Klippenstein, S. J. A Two Transition State Model for Radical–Molecule Reactions: Applications to Isomeric Branching in the OH–Isoprene Reaction. *The Journal of Physical Chemistry A* **2007**, *111* (25), 5582-5592. DOI: 10.1021/jp071412y. Balucani, N.; Asvany, O.; Chang, A. H. H.; Lin, S. H.; Lee, Y. T.; Kaiser, R. I.; Bettinger, H. F.; Schleyer, P. v. R.; Schaefer, H. F. Crossed beam reaction of cyano radicals with hydrocarbon molecules. I. Chemical dynamics of cyanobenzene (C₆H₅CN; X1A1) and perdeutero cyanobenzene (C₆D₅CN; X1A1) formation from reaction of CN(X2Σ⁺) with benzene C₆H₆(X1A1g), and d₆-benzene C₆D₆(X1A1g). *The Journal of Chemical Physics* **1999**, *111* (16), 7457-7471. DOI: 10.1063/1.480070 (accessed 2022/06/21).

(45) Yang, D. L.; Yu, T.; Lin, M. C.; Melius, C. F. The reaction of CN with CH₄ and CD₄: an experimental and theoretical study. *Chemical Physics* **1993**, *177* (1), 271-280. DOI: [https://doi.org/10.1016/0301-0104\(93\)80195-F](https://doi.org/10.1016/0301-0104(93)80195-F).

- (46) Gladstone, G. R.; Allen, M.; Yung, Y. L. Hydrocarbon Photochemistry in the Upper Atmosphere of Jupiter. *Icarus* **1996**, *119* (1), 1-52. DOI: <https://doi.org/10.1006/icar.1996.0001>.
- Ferguson, H. C.; Sandage, A. The Spatial Distributions and Intrinsic Shapes of Dwarf Elliptical Galaxies in the Virgo and Fornax Clusters. *The Astrophysical Journal* **1989**, *346*, L53. DOI: 10.1086/185577.
- (47) Rowe, B. R.; Dupeyrat, G.; Marquette, J. B.; Gaucherel, P. Study of the reactions $N+2+2N_2 \rightarrow N+4+N_2$ and $O+2+2O_2 \rightarrow O+4+O_2$ from 20 to 160 K by the CRESU technique. *The Journal of Chemical Physics* **1984**, *80* (10), 4915-4921. DOI: 10.1063/1.446513 (accessed 2022/06/19). Dupeyrat, G.; Marquette, J. B.; Rowe, B. R. Design and testing of axisymmetric nozzles for ion-molecule reaction studies between 20 °K and 160 °K. *The Physics of Fluids* **1985**, *28* (5), 1273-1279. DOI: 10.1063/1.865010 (accessed 2022/06/19). Canosa, A.; Sims, I. R.; Travers, D.; Smith, I. W. M.; Rowe, B. R. Reactions of the methylidene radical with CH₄, C₂H₂, C₂H₄, C₂H₆, and but-1-ene studied between 23 and 295 K with a CRESU apparatus. *Astronomy and Astrophysics* **1997**, *323*, 644-651.
- (48) Smith, I. W. M. Reactions at Very Low Temperatures: Gas Kinetics at a New Frontier. *Angewandte Chemie International Edition* **2006**, *45* (18), 2842-2861, <https://doi.org/10.1002/anie.200502747>. DOI: <https://doi.org/10.1002/anie.200502747> (accessed 2022/06/19).
- (49) Potapov, A.; Canosa, A.; Jiménez, E.; Rowe, B. Uniform Supersonic Chemical Reactors: 30 Years of Astrochemical History and Future Challenges. *Angewandte Chemie International Edition* **2017**, *56* (30), 8618-8640, <https://doi.org/10.1002/anie.201611240>. DOI: <https://doi.org/10.1002/anie.201611240> (accessed 2022/06/19). Speck, T.; Mostefaoui, T. I.; Travers, D.; Rowe, B. R. Pulsed injection of ions into the CRESU experiment. *International Journal of Mass Spectrometry* **2001**, *208* (1), 73-80. DOI: [https://doi.org/10.1016/S1387-3806\(01\)00383-9](https://doi.org/10.1016/S1387-3806(01)00383-9).

- (50) Sims, I. R.; Smith, I. W. M. GAS-PHASE REACTIONS AND ENERGY-TRANSFER AT VERY-LOW TEMPERATURES. *Annual Review of Physical Chemistry* **1995**, *46*, 109-137. DOI: 10.1146/annurev.pc.46.100195.000545.
- (51) Hanson, R. K.; Davidson, D. F. Recent advances in laser absorption and shock tube methods for studies of combustion chemistry. *Progress in Energy and Combustion Science* **2014**, *44*, 103-114. DOI: 10.1016/j.pecs.2014.05.001.
- (52) Sung, C. J.; Curran, H. J. Using rapid compression machines for chemical kinetics studies. *Progress in Energy and Combustion Science* **2014**, *44*, 1-18. DOI: 10.1016/j.pecs.2014.04.001.
- (53) Burke, M. P.; Chaos, M.; Ju, Y. G.; Dryer, F. L.; Klippenstein, S. J. Comprehensive H₂/O₂ kinetic model for high-pressure combustion. *International Journal of Chemical Kinetics* **2012**, *44* (7), 444-474. DOI: 10.1002/kin.20603. Zhou, Y. Rayleigh-Taylor and Richtmyer-Meshkov instability induced flow, turbulence, and mixing. II. *Physics Reports-Review Section of Physics Letters* **2017**, *723*, 1-160. DOI: 10.1016/j.physrep.2017.07.008.
- (54) Burcat, A.; Dvinyaninov, M. Detailed kinetics of cyclopentadiene decomposition studied in a shock tube. *International Journal of Chemical Kinetics* **1997**, *29* (7), 505-514, [https://doi.org/10.1002/\(SICI\)1097-4601\(1997\)29:7<505::AID-KIN4>3.0.CO;2-Y](https://doi.org/10.1002/(SICI)1097-4601(1997)29:7<505::AID-KIN4>3.0.CO;2-Y). DOI: [https://doi.org/10.1002/\(SICI\)1097-4601\(1997\)29:7<505::AID-KIN4>3.0.CO;2-Y](https://doi.org/10.1002/(SICI)1097-4601(1997)29:7<505::AID-KIN4>3.0.CO;2-Y) (accessed 2022/06/20).
- (55) Fridlyand, A.; Lynch, P. T.; Tranter, R. S.; Brezinsky, K. Single Pulse Shock Tube Study of Allyl Radical Recombination. *The Journal of Physical Chemistry A* **2013**, *117* (23), 4762-4776. DOI: 10.1021/jp402391n. Tranter, R.; Yang, X.; Kiefer, J. Dissociation of C₃H₃I and rates for C₃H₃ combination at high temperatures. *Proceedings of the Combustion Institute* **2011**, *33*, 259-265. DOI: 10.1016/j.proci.2010.05.030.
- (56) Fernandes, R.; Brassat, A.; Thewes, M.; Müther, M.; Pischinger, S. Analysis of the Effects of Certain Alcohol and Furan-Based Biofuels on Controlled Auto Ignition. *SAE International Journal of Fuels and Lubricants* **2012**. DOI: 10.4271/2012-01-1135. Thewes, M.; Muether, M.;

Pischinger, S.; Budde, M.; Brunn, A.; Sehr, A.; Adomeit, P.; Klankermayer, J. Analysis of the Impact of 2-Methylfuran on Mixture Formation and Combustion in a Direct-Injection Spark-Ignition Engine. *Energy & Fuels* **2011**, *25* (12), 5549-5561. DOI: 10.1021/ef201021a.

(57) Pham, T. V.; Tue Trang, H. T. Combination Reactions of Propargyl Radical with Hydroxyl Radical and the Isomerization and Dissociation of trans-Propenal. *The Journal of Physical Chemistry A* **2020**, *124* (30), 6144-6157. DOI: 10.1021/acs.jpca.0c05106.

(58) Osborn, D. L.; Zou, P.; Johnsen, H.; Hayden, C. C.; Taatjes, C. A.; Knyazev, V. D.; North, S. W.; Peterka, D. S.; Ahmed, M.; Leone, S. R. The multiplexed chemical kinetic photoionization mass spectrometer: A new approach to isomer-resolved chemical kinetics. *Review of Scientific Instruments* **2008**, *79* (10), 104103. DOI: 10.1063/1.3000004 (accessed 2022/06/23).

(59) Savee, J.; Soorkia, S.; Welz, O.; Selby, T.; Taatjes, C.; Osborn, D. Absolute photoionization cross-section of the propargyl radical. *The Journal of chemical physics* **2012**, *136*, 134307. DOI: 10.1063/1.3698282.

(60) Suzuki, H.; Yamamoto, S.; Ohishi, M.; Kaifu, N.; Ishikawa, S.; Hirahara, Y.; Takano, S. A SURVEY OF CCS, HC3N, HC5N, AND NH3 TOWARD DARK CLOUD CORES AND THEIR PRODUCTION CHEMISTRY. *Astrophysical Journal* **1992**, *392* (2), 551-570. DOI: 10.1086/171456.

(61) Vandishoeck, E. F.; Blake, G. A.; Jansen, D. J.; Groesbeck, T. D. MOLECULAR ABUNDANCES AND LOW-MASS STAR-FORMATION .2. ORGANIC AND DEUTERATED SPECIES TOWARD IRAS-16293-2422. *Astrophysical Journal* **1995**, *447* (2), 760-782. DOI: 10.1086/175915. Monthly Energy Review. Administration, U. S. E. I., Ed.; 2022. Energy, U. S. D. o. *Where the Energy Goes: Gasoline Vehicles*. 2022. <https://www.fueleconomy.gov/feg/atv.shtml> (accessed).

(62) Frisch, M., Trucks G., Schlegel H, et al. Gaussian 09. Gaussian Inc: Wallingford, CT, 2016, 2022.

(63) Guelin, M.; Cernicharo, J. Organic Molecules in Interstellar Space: Latest Advances. *Frontiers in Astronomy and Space Sciences* **2022**, *9*. DOI: 10.3389/fspas.2022.787567.

(64) Marinov, N. M.; Castaldi, M. J.; Melius, C. F.; Tsang, W. Aromatic and polycyclic aromatic hydrocarbon formation in a premixed propane flame. *Combustion Science and Technology* **1997**, *128* (1-6), 295-342. DOI: 10.1080/00102209708935714. Mebel, A. M.; Kaiser, R. I. Formation of resonantly stabilised free radicals via the reactions of atomic carbon, dicarbon, and tricarbon with unsaturated hydrocarbons: theory and crossed molecular beams experiments. *International Reviews in Physical Chemistry* **2015**, *34* (4), 461-514. DOI: 10.1080/0144235x.2015.1075280. Lindstedt, R. P.; Skevis, G. Chemistry of acetylene flames. *Combustion Science and Technology* **1997**, *125* (1-6), 73-137. DOI: 10.1080/00102209708935656.

(65) Anitescu, G.; Bruno, T. J. Fluid properties needed in supercritical transesterification of triglyceride feedstocks to biodiesel fuels for efficient and clean combustion - A review. *Journal of Supercritical Fluids* **2012**, *63*, 133-149. DOI: 10.1016/j.supflu.2011.11.020.

Chapter 2: Experimental and Methods

When studying species involved in molecular growth, the low temperature to room temperature regime is well studied by CRESU experiments and standard flow experiments. The CRESU technique can achieve temperatures as low as 10K to mimic temperatures that you would find in the interstellar medium and gaseous clouds⁵¹. On the other end of the temperature spectrum, shock tubes can cover the extreme elevated temperatures and pressures. In shock tube experiments, the initial conditions for the shock can be set such that any range of high pressure and temperature conditions can be produced. While both techniques have been used in experiments for the high and low extremes of temperature and pressure, there is a noticeable lack of information for many species of interest in the temperature range between 300 K – 1000 K. To fill this void of information, this chapter covers the development of a novel experimental apparatus designed by Bertrand Rowe using many of the same principles as the CRESU technique, addressing many of the shortcomings of other experimental techniques. The purpose of the new experimental apparatus is to perform kinetic and product detection studies in-house.

2.1 High-Temperature Fast-Flow

To try and compensate for these shortcomings, a high-temperature fast-flow flow tube is designed for the purpose of studying RSRs and their involvement in radical-radical reactions between the extreme ends of the temperature regimes that are more commonly studied. This novel reactor allows for generation of radicals at the center of the gas flow, much like the CRESU technique, removing the possibility with reaction of the walls and radical species. Heating of the gas is done far from the optical equipment that is used to measure radical

concentrations, and the pulsed flow tube nature of the apparatus allows for repeatability while reducing the overall volume flow rate and pumping power required.

A schematic of the fast flow is shown in Figure 2.1. The target temperature range for the flow reactor is 300 K to 750 K with a flow velocity of 100 m s^{-1} , corresponding to a reaction time of up to 10 ms for kinetic studies. The main buffer gas of argon is used with a constant mass flow rate of 5 standard liters per minute (SLM) enters a small double walled reservoir with a volume of 50 cm^3 . The gas is heated by conduction with the walls, which are heated by thermal tape and regulated externally. The total power required to heat 5 SLM of argon to 750 K is on the order of 34 W (including gas and heat loss). The reservoir is connected to a larger buffer reservoir of 3.7 L in volume to maintain constant pressure. This reservoir maintains contact with the ambient conditions of the room and remains at room temperature. A rotating disk called the “chopper” allows gas from the reservoir to enter the custom designed Laval nozzle and then flow down the tube. The purpose of the chopper is to limit the gas flow to maintain the instantaneous conditions matching that of a continuous flow. The Mach 5 Laval nozzle is designed with a short convergent and elongated divergent section. The sole purpose of the nozzle is to restrict the instantaneous mass flow rate during the opening of the chopper while increasing flow diameter to match that of the flow tube of 8cm in diameter. The Laval nozzle in conjunction with the chopper allow for the same flow conditions that would be present in a continuous flow of gas, but with a greatly decreased gas flow and pumping requirement. The flow tube is connected to a 200L reservoir that serves a similar purpose of making sure the pressure of the flow is not perturbed by the opening of the chopper. A roots pump evacuates the flow tube far downstream of the nozzle.

In order to have a proper supersonic expansion through the Laval nozzle, the driving force for the gas must be sufficient between the reservoir and the flow tube, which is specific to the temperature and identity of the gas. The driving force is obtained through a differential of pressure between the reservoir and the flow tube, separated by the Laval nozzle. When supersonic expansion conditions are met, the flow of gas through the nozzle becomes choked, and supersonic expansion occurs after the throat of the nozzle. According to the isentropic expansion equations mentioned above, the supersonic expansion of the gas leads to both a cooling and a decrease in pressure along the length of the nozzle. Up to this point, the technique is similar to what has been done with the CRESU technique in low temperature experiments.

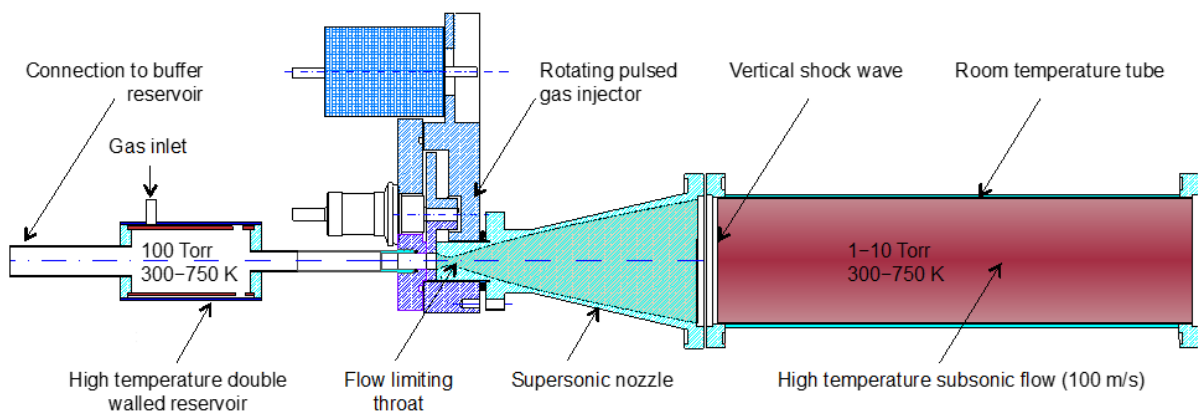


Figure 2.1. Schematic of the high-temperature pulsed flow reactor. Temperatures of up to 750 K are attainable for the purpose of kinetic and product detection studies.

Simulations performed by El Ghazaly Moulay Ismail in a master's thesis of the temperature and Mach number along the length of the nozzle are depicted in figure 2.2. During the expansion of the gas through the Laval nozzle, the heat that the gas obtained from the reservoir is converted to translational energy, resulting in a cold and supersonic gas at the exit of the nozzle. In order to reobtain the temperatures of the reservoir gas to achieve the

temperatures necessary to perform chemical studies, the pressure of the flow tube is adjusted to well above the pressure of the expanding gas in the nozzle. This generates a stationary normal shock wave at the boundary between the nozzle and the flow tube, converting most of the translational energy gained during the expansion back into thermal energy. The energy that is not converted into heat for the gas is in the translational motion of the gas down the flow tube. This process, unlike the expansion through the Laval nozzle, is adiabatic instead of isentropic. After the expansion has passed through the shockwave, nearly all of the temperature prior to expansion is recovered, where the difference in temperature is attributed to the energy needed for the movement of the flow of gas itself.

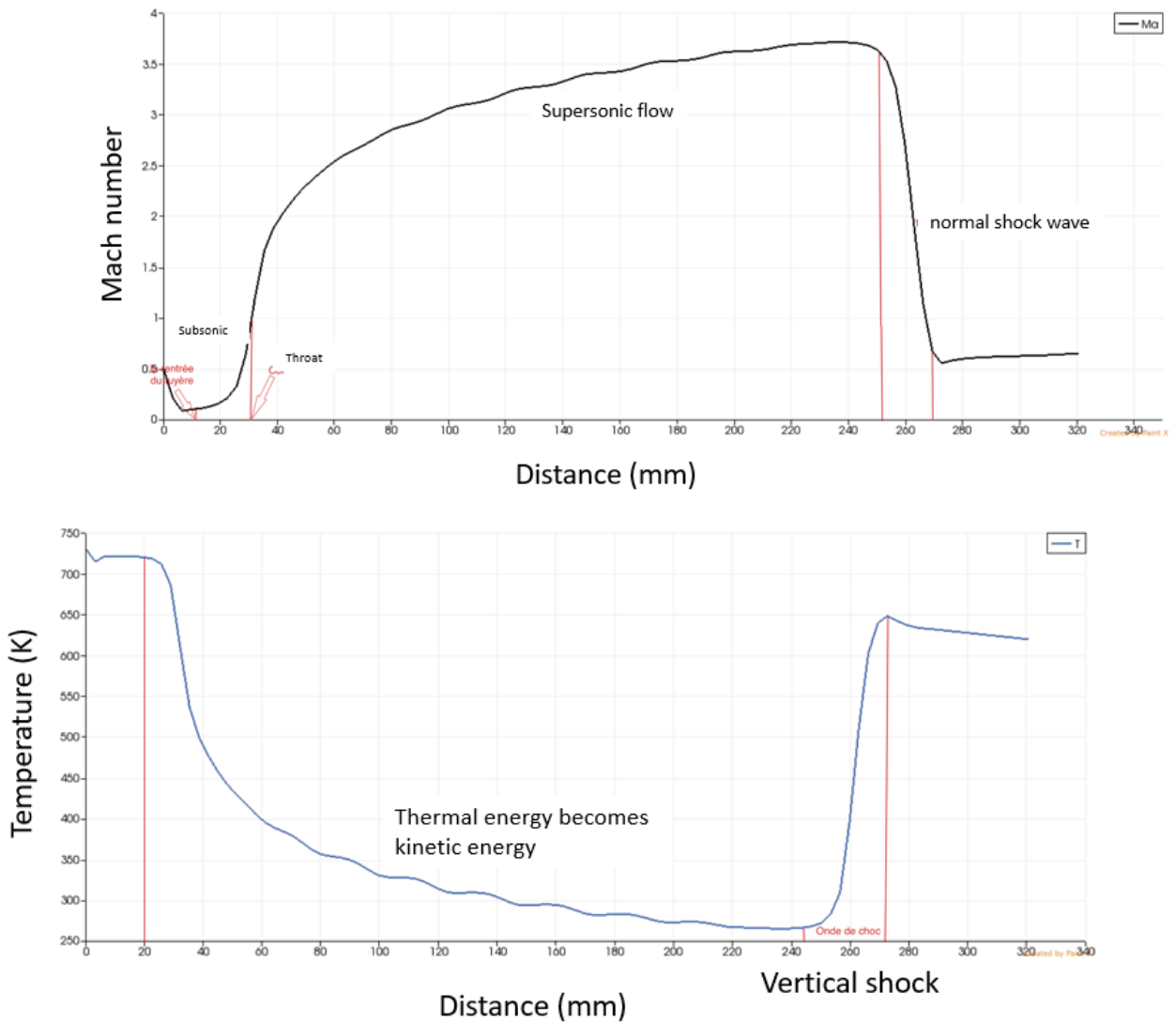


Figure 2.2. Mach and temperature profiles along the length of the Laval nozzle depicting the vertical shockwave.

The resulting gas flow after the shock wave is a subsonic ($M \approx 0.3$) gas with temperatures nearly equal to that of the reservoir, with some energy loss due to the conversion through the shockwave. The length of the resulting uniform, hot, subsonic flow is defined by equation 2.1:

$$L = \frac{0.6Q_m}{\eta} \quad (2.1)$$

where L is the hydrodynamic length of the high-temperature flow, η is the gas viscosity, and Q_m is the mass flow rate. The hydrodynamic length of the high-temperature flow must be sufficiently long for the detection of the species in the kinetic and product detection studies. As the gas travels down the flow tube, a boundary layer forms as the hot gas makes contact with the room temperature walls of the flow tube, shown in figure 2.3. The hydrodynamic length represents the distance at which the boundary layer fully collapses in on the high-temperature flow created by the shockwave. This flow will be referred to as the high-temperature flow for clarity. The loss of experienced through the shockwave is defined as follows in equation 2.2:

$$\Delta S = \frac{\delta Q}{T} + dS_{irrev} \quad (2.2)$$

where S is entropy, T is temperature, and S_{irrev} is the entropy lost through the irreversible process of passing through the shockwave. The changes across a normal shock wave is depicted in equation 2.3 below:

$$\frac{T_1}{T_0} = \frac{[2\gamma M^2 - (\gamma - 1)][(\gamma - 1)M^2 + 2]}{(\gamma + 1)^2 M^2} \quad (2.3)$$

Where T_1 is the temperature after the shockwave and T_0 is the temperature of the supersonic flow. The pressure change across the shockwave is depicted in equation 2.4:

$$\frac{\rho_1}{\rho_0} = \frac{(\gamma + 1)M^2}{(\gamma - 1)M^2 + 2} \quad (2.4)$$

Where ρ_1 is the pressure after the shockwave and ρ_0 is the pressure before the shockwave. The speed of the gas is depicted in equation 2.5 below:

$$(M_1)^2 = \frac{(\gamma-1)M^2+2}{2\gamma M^2-(\gamma-1)} \quad (2.5)$$

Where M_1 is the speed after the shockwave.

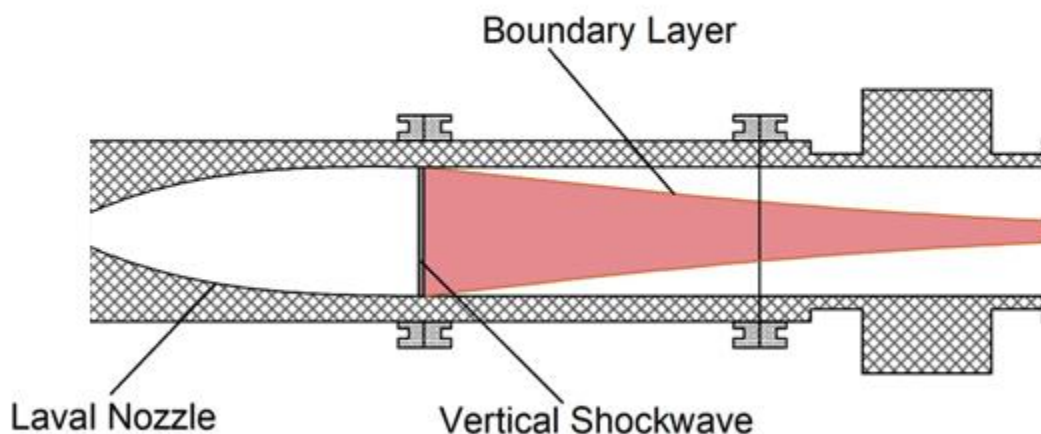


Figure 2.3: Boundary layer formation after supersonic expansion through a standing normal shockwave, resulting in a subsonic, high-temperature flow

The exact timing of all the moving parts of the fast flow is necessary to perform kinetic studies inside of the apparatus. Toluene was flowed through the cell at low flow rates to prevent supersonic expansion of the nozzle from occurring. A 266 nm Nd:YAG laser was used to excite the toluene along the length of the flow. The toluene signal increases as the chopper is open and more toluene is let into the cell. A depiction of the theoretical timing of the experiment as it relates to kinetic studies and the PLP-LIF technique is shown in figure 2.4.

The chopper rotates to open at $t = 0$. When the flow is uniform and established, which occurs shortly after 5 ms has passed, the photolysis laser is fired along the flow and creates the radical species of interest. At the same time, excitation laser the is fired perpendicular to the flow to excite the reactant radicals. The radical fluorescence signal observed is proportional to the unreacted radicals in the flow. The timing between the excitation and photolysis laser is increased, allowing the plotting of k_{2nd} rate coefficient curves for the reaction.

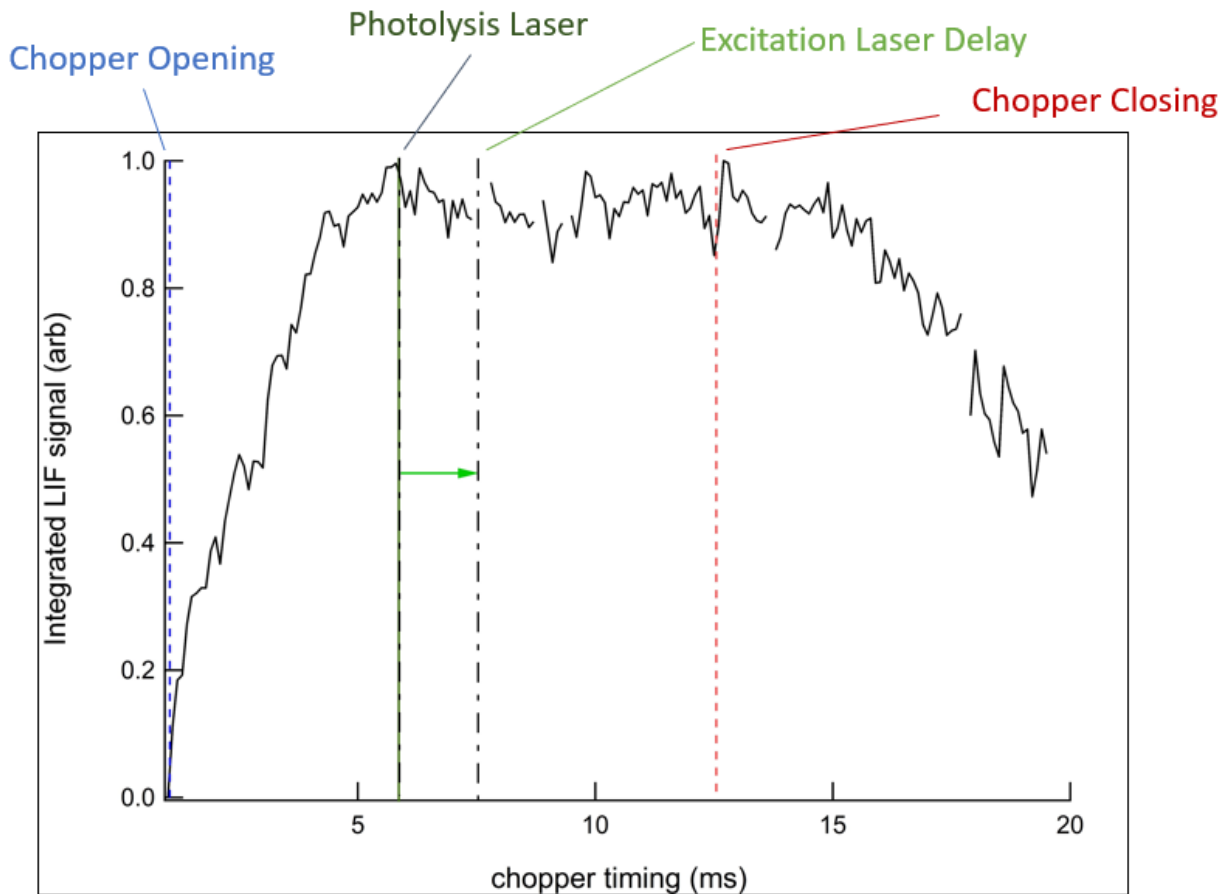


Figure 2.4. Kinetic experimental timing for the high-temperature fast-flow cell.

2.2 Validation of Flow Conditions

2.2.1 Pitot Tube Measurements

In order to make sure that the conditions in the high-temperature flow are as they were designed to be, it is necessary to validate the operating pressure and temperature conditions within the gas flow inside of the flow tube. Confirming the proper expansion of gas through the nozzle, the temperature of the resulting gas after the shockwave, and the uniformity of the high-temperature flow are required to be able to obtain reliable experimental data. To make proper pressure measurements inside of the flow cell, a custom set of two pitot tubes were constructed to measure the impact pressure of the high-temperature flow along the length of

the tube. Figure 2.5 depicts a diagram of the pitot tube. Pitot tubes have been verified to be accurate tools in characterizing the properties of a gas flow.⁶⁶ The pitot tubes itself is comprised

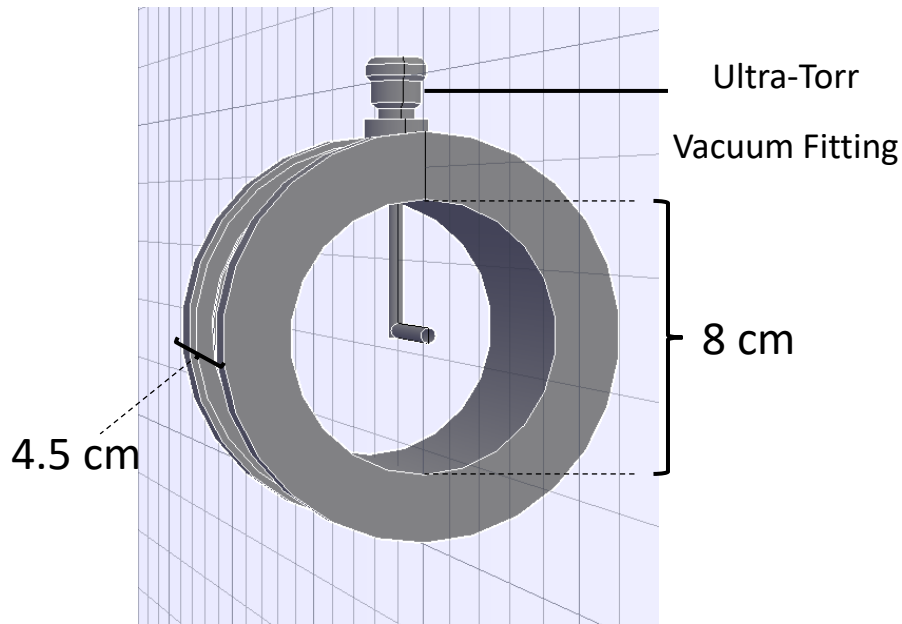


Figure 2.5. Pitot tube insert used to measure the impact pressure of the flow at subsonic and supersonic conditions.

of stainless steel, with a 2 mm opening. The inner diameter of the pitot tube increases to 4 mm to increase volume, allowing for more accurate measurements of the impact pressure. Tube is fitted to an Ultra-Torr stainless steel Swagelok that holds vacuum while allowing the pitot tube to be adjusted into or out of the path of gas. The other end of the pitot tube is attached to a pressure gauge. The Ultra-Torr fitting is attached to a Teflon insert with an inner diameter of 8cm and a length of 4.5cm, matching the diameter of the fast flow cell itself. The pitot tube opening extends 1 cm past the plane of the Teflon insert, enabling probing of the supersonic expansion inside of the Laval nozzle.

The Laval nozzle is designed to have a maximum expansion at Mach 5, assuming free expansion out of the Laval nozzle (no standing normal shock wave). Given proper expansion, the minimum Mach number that can be obtained is the value of $M = 0.414$. This is the value that is calculated for the uniform, high-temperature flow given the speed of the nozzle and the preset flow condition pressures. The speed of the gas after the nozzle should be subsonic to confirm that the kinetic energy of the expansion was transformed back into thermal energy by the standing shock wave. Verifying the proper expansion of the gas through the Laval nozzle comes with additional challenges due to a bow shock being created at the opening of the pitot tube. This complicates the measurement of the flow inside of the Laval nozzle as the shock will decrease the apparent pressure measurement. A depiction of this phenomenon is shown in figure 2.6.

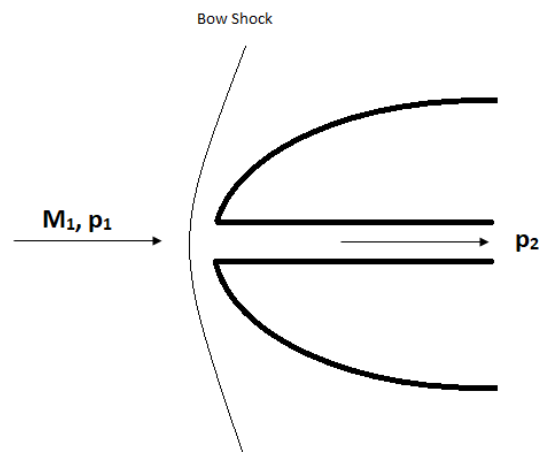


Figure 2.6. Bow shock formation at the entrance of a pitot tube due to supersonic gas flow

A new formula is needed to determine the Mach number by using a pitot tube in a supersonic flow, shown in equation 2.6:

$$\frac{P_i}{P_0} = \left[\frac{\gamma + 1}{2} M_1^2 \right]^{\frac{\gamma}{\gamma-1}} \left[\frac{\gamma + 1}{2\gamma M_1^2 - (\gamma - 1)} \right]^{\frac{1}{\gamma-1}} \quad (2.6)$$

This equation is called the Rayleigh-Pitot tube formula. Using this equation, it is possible to verify the proper expansion of the gas in the Laval nozzle using pitot tube measurements. The

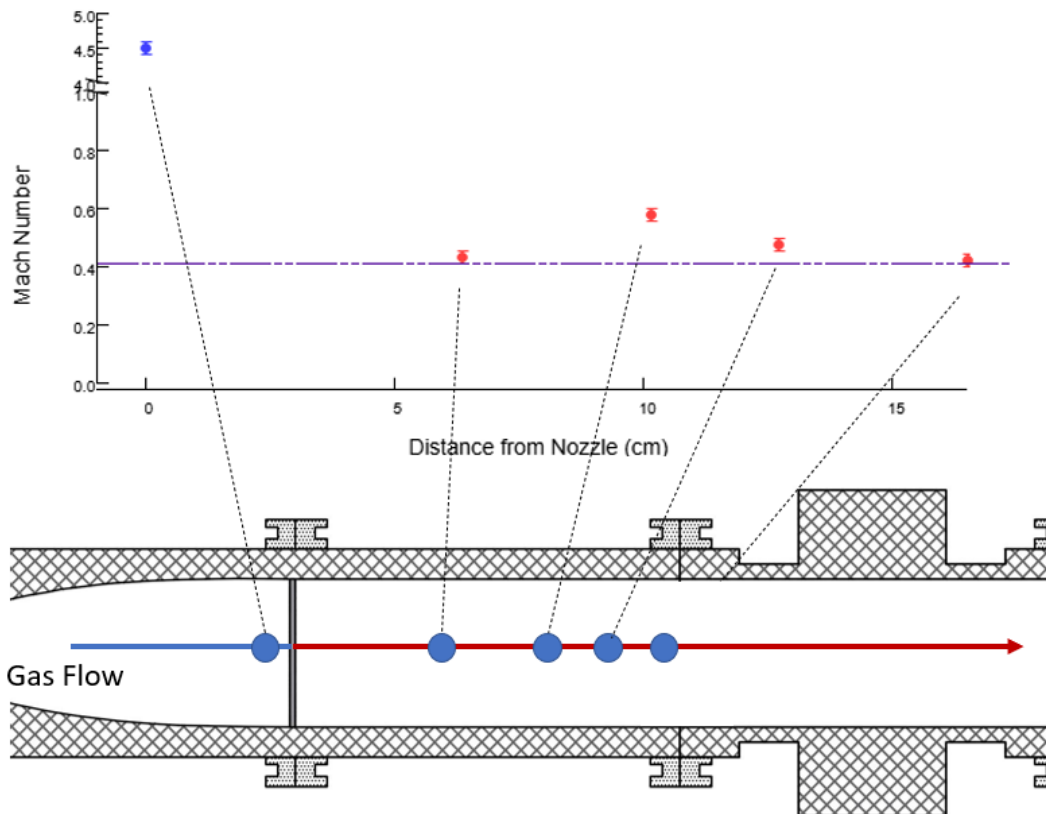


Figure 2.7. Mach number profile as a function of distance from the exit of the nozzle at 450 K reservoir temperature, 4 SLM flow rate, and 60 Torr reservoir pressure. The horizontal blue line is the minimum expected Mach number after the gas has undergone supersonic expansion and passed through the shockwave.

isentropic flow equation for pressure can be used for measurements after the exit of the nozzle, as the flow has changed from supersonic to the high-temperature flow.

The Mach number measurements obtained for a set length of the flow tube is shown in figure 2.7. The conditions of the flow reactor were set at 60 Torr in the reservoir, with a mass

flow rate of 4 SLM, and a reservoir temperature of 450K. The pitot tube was set at various distances relative to the Laval nozzle exit at increments of 4.5 cm corresponding to the length of the pitot tube Teflon housing. At the exit of the nozzle, the pitot tube recorded Mach number of the expansion is approximately 4.5, which is very close to the designed expansion speed of the nozzle at $M = 5$. After the nozzle, the gas will interact with the standing shockwave and become a subsonic and uniform flow of gas until the boundary layers close in on the high-temperature flow.

Pressure profiles of the pulsed fast-flow reactor are shown in figure 2.8. The figure depicts 2 cycles of the 10 Hz pulsed flow. As the pressure inside of the flow tube is set to lower than is required for the establishment of the shock wave shown by the black lines, the experienced impact pressure by the pitot tube is extremely high, as is expected by a supersonic expansion. At pressures near 2 – 3 Torr, the supersonic flow is disturbed, and no discernable pressure pattern can be seen. As the pressure is set experimentally closer to the necessary pressure for the establishment of the standing shockwave at approximately 4 Torr post-nozzle pressure, the flow becomes uniform and stable.

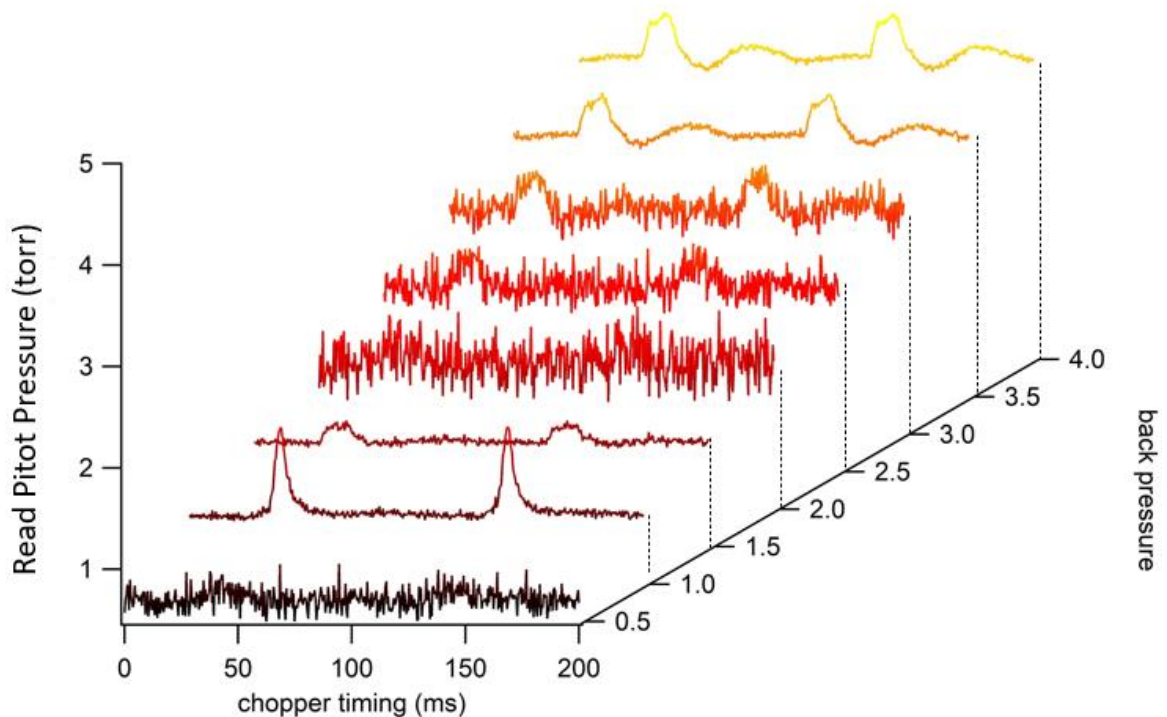


Figure 2.8. Time-resolved pressure measurements of the pitot tube at 750 K and 4 SLM total flow as a function of the throttled back pressure of the cell. Establishment of flow conditions can be seen at approximately 3.5 – 4 Torr back pressure.

2.3 Temperature Determination of the High-temperature Flow

It is possible using the isentropic expansion equation 1.4 and the pitot tube measurements to determine the temperature of the flow, as the pressure measurements give us the Mach number which allows solving for the temperature. Doing so from the pressure measurements shown in figure 2.7 for 450 K reservoir temperature yields a temperature of ≈ 415 K. While this method of temperature determination does provide a satisfactory temperature result, a more direct measurement of the temperature itself would provide more certainty that the flow conditions are correct. Due to the pulsed nature of the flow, no physical temperature probe exists that has a time resolution precise enough to accurately determine the temperature. To this end, the rotational temperature of a radical species will be used to validate the exact temperature of the flow.

2.4 Kinetic and Product Detection Studies

Figure 2.9 shows the detection zone for the measurement of rate coefficients in the flow reactor.

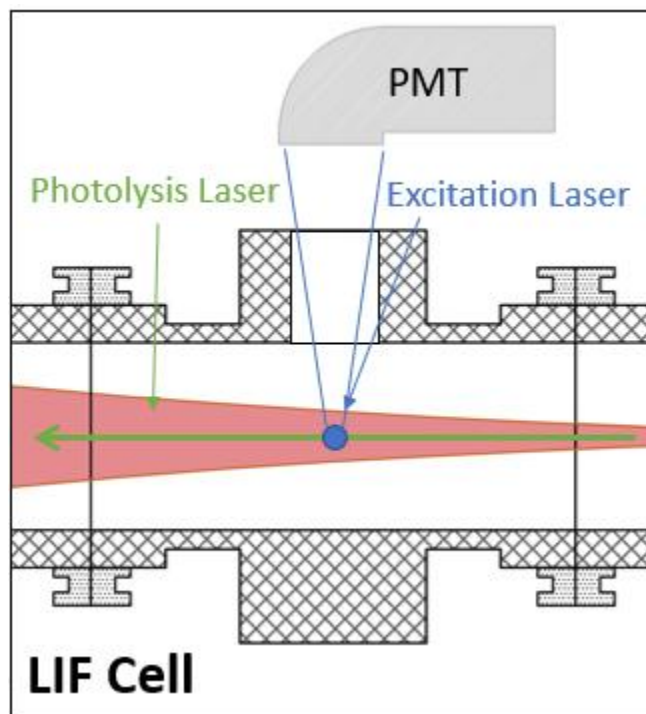


Figure 2.9 Schematic of the detection cell coupled to the pulsed flow. The detection zone for the laser-induced fluorescence occurs downstream of the nozzle while the time-of-flight mass spectrometer samples the flow downstream after the reaction has occurred.

The flow tube is connected to a 6-way optical cell similar to what is described in Kailasanathan et al.⁶⁷ As both products and rate kinetics need to be studied and understood to have a complete understanding of a reaction, the flow reactor was designed to include both a laser-induced fluorescence (LIF) system and a mass spectrometer probing the flow. This two-pronged approach of the study of the products and kinetics of a given reaction, in conjunction with computational work, will allow for the complete understanding of a reaction. The mass

spectrometer attachment is planned for the near future to set up. The laser-induced fluorescence system and the specifics of kinetic studies will be discussed in the next chapter.

2.5 Quasi-Static Reaction Cell

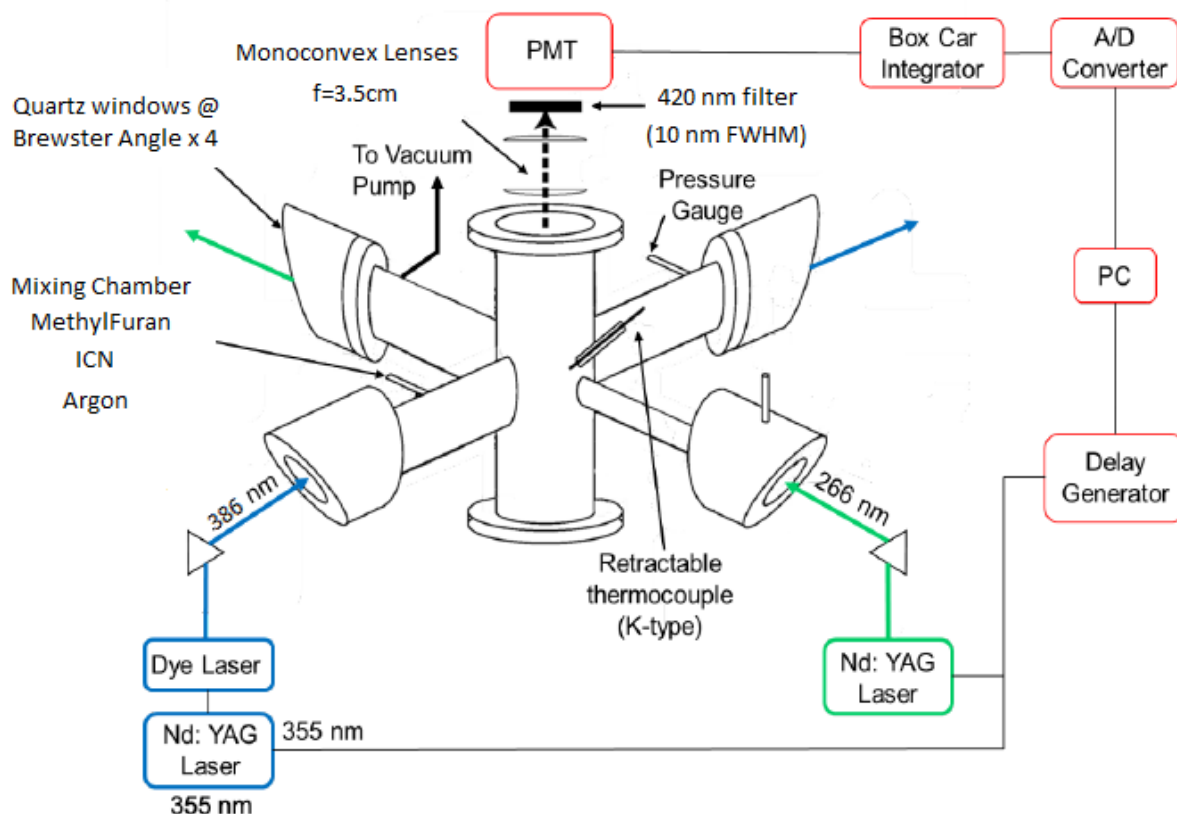


Figure 2.10. Schematic of the quasi-static reaction cell used in the CN determination of temperature by CN rovibrational excitation as well as the kinetic study of CN + 2-methylfuran

The study described here provides a method for determining the temperature within a quasi-static reaction cell, shown in figure 2.10. The cell was chosen to test the temperature probing method that will be used in the fast flow because the cell has been validated in other kinetic studies.⁶⁷ The reactions are conducted in a pressure-adjustable, heatable, six-way cross stainless-steel reaction cell. The pressure is adjusted from approximately 2–10 Torr using a butterfly valve, while the temperature is varied from 304–440 K using heating tape. Laser windows placed at Brewster-angle are positioned at the four horizontal ports while a

photomultiplier tube (PMT) is placed above a fused-silicate window located at the top of the reaction cell. Calibrated mass flow controllers regulate all gases into a 50 cm³ mixing volume prior to flowing into the reaction cell. The gaseous ICN precursor is introduced into the system by passing argon through a sample of solid ICN (Acros Organics, 98%), which is nested in porous glass wool and placed in a stainless-steel cylinder. The 2-MF/Ar (approx. 6% 2-MF) gas mixtures are prepared and stored in a custom-made (5.39 L) gas collection cylinder. Liquid 2-MF (Acro Organics, 99%) is vacuum transferred into the empty cylinder until the pressure reaches approximately 60 Torr. The tank is then filled with argon to a total pressure of approximately 1000 Torr. The mixture is tested for purity using a 25 cm³ double-pass gas cell (Mettler Toledo) with an FTIR spectrometer attachment (Mettler Toledo, ReactIR ic 15), specifically for the presence of CO₂ (from ambient air). The ICN and 2-MF flows are mixed prior to entering the experimental gas cell to ensure uniformity. The total mass flow rate of 1.529 slm is set to assure that the detection zone is replenished with new gas between each photolysis laser pulse.

This cell will be used to confirm the accuracy of the temperature obtained from the rotational temperature of the CN radical, and further validated using a pulsed laser photolysis/laser-induced fluorescence (PLP/LIF) technique to study a radical reaction involving the CN radical

2.6 Pulsed Laser Photolysis/Laser-Induced Fluorescence

The spectroscopic technique of Pulsed Laser Photolysis/Laser-Induced Fluorescence (PLP/LIF) is a widely used technique spanning many different fields.^{1, 11, 20, 25, 40, 50, 54, 67, 68} Figure 2.11 depicts an energy diagram of a rovibrational transition that can be measured via PMT. Pulsed laser

photolysis occurs with the firing of a high-powered laser pulse in the UV region to break the bond of the precursor, creating the radical. The second laser is then tuned to the excitation wavelength specific to the radical, causing excitation to a higher rovibronic state through photon absorption. After excitation, the radical will relax spontaneously back to a lower rovibronic state to emit a photon of lower energy than it was excited with. This photon can be collected and viewed using a photosensitive device such as a photomultiplier tube (PMT) or a photodiode, which translates the captured photon into an electrical signal.

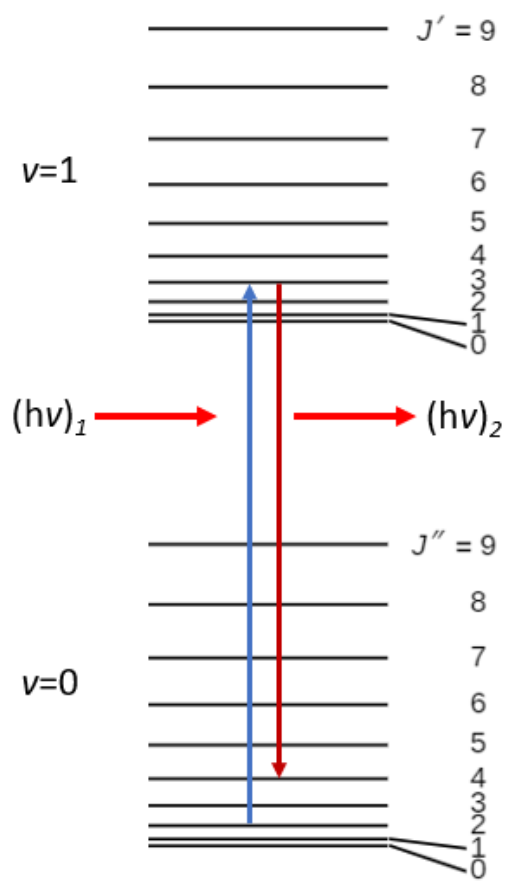


Figure 2.11. Rovibrational transition from the $v=0$ state to $v=1$

2.7 Pseudo-First Order Kinetics

Kinetic studies on the CN ($B^2\Sigma^+$) + 2-methylfuran reaction were performed in a quasi-static reaction cell over the pressure ranges of 2.7 – 7.6 Torr and temperature range of 304 – 440 K. Experiments are performed under pseudo-first order conditions with the $[MF] \gg [CN]$. The LIF signal decay is fit to the following equations:

$$[CN]_t = [CN]_0 e^{-k_{1st}\Delta t} \quad (2.4)$$

$$k_{1st} = k_{2nd}[MF] + k'_{1st} \quad (2.5)$$

where Δt is the time delay between the excitation and photolysis lasers, k_{1st} is the pseudo-first order rate constant for the radical decay of CN, k_{2nd} is the overall second-order reaction rate constant of the CN + 2-MF reaction, $[CN]_0$ and $[CN]_t$ refer to the CN radical concentrations initially and at time Δt , $[MF]$ is the number density of 2-MF, and k'_{1st} is the first-order rate constant for loss of the CN radical with side products such as I_2 , I, or with its precursor ICN. The concentration of ICN remains constant during data collection.

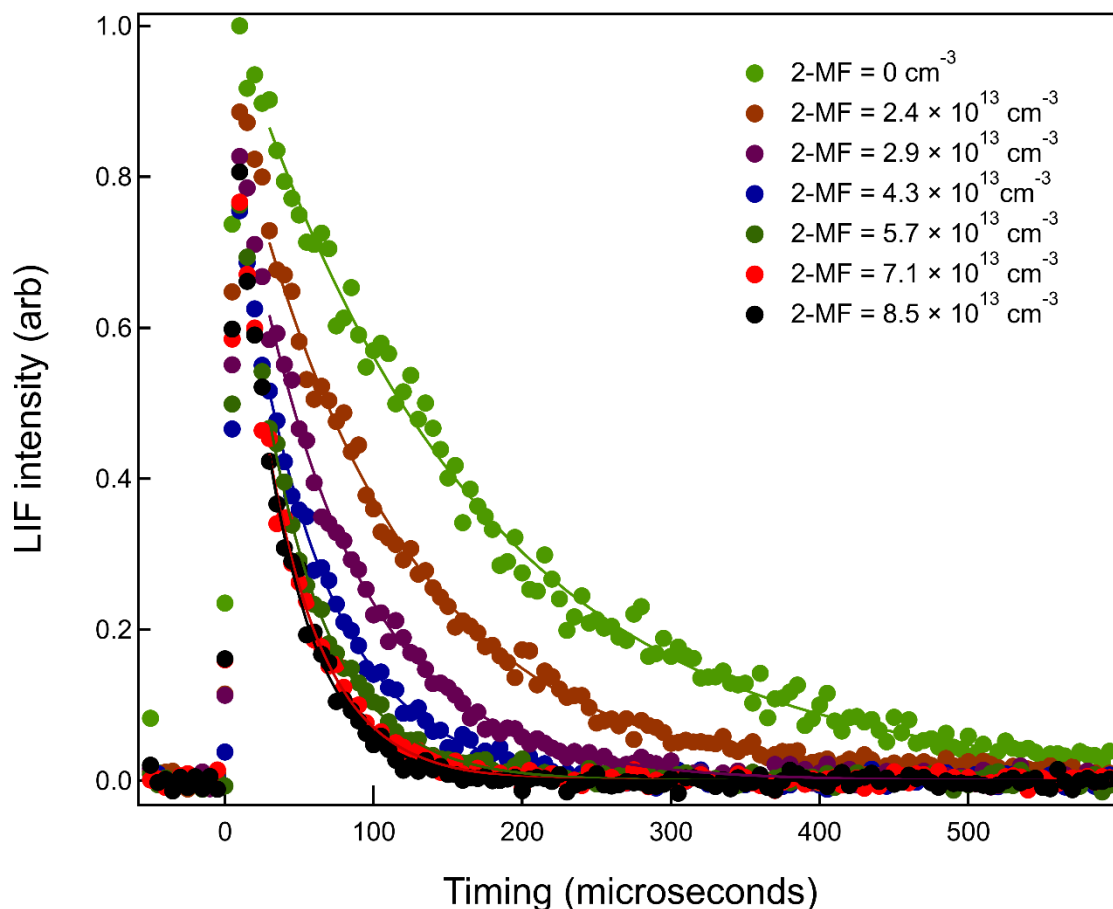


Figure 2.12. CN LIF-signal temporal trace at different 2-MF number densities as follows: $0.0 \text{ molecules cm}^{-3}$ (light green), $2.4 \times 10^{13} \text{ molecules cm}^{-3}$ (brown), $2.9 \times 10^{13} \text{ molecules cm}^{-3}$ (purple), $4.3 \times 10^{13} \text{ molecules cm}^{-3}$ (blue), $5.7 \times 10^{13} \text{ molecules cm}^{-3}$ (dark green), $7.1 \times 10^{13} \text{ molecules cm}^{-3}$ (red), $8.5 \times 10^{13} \text{ molecules cm}^{-3}$ (black). The lines are exponential fit to the experimental data from 30 to 600 μs .

The CN LIF signal is integrated and plotted against the delay time between the two lasers.

Figure 2.12 displays the decay of the CN LIF signal at different 2-MF number densities as follows:

$0.0 \text{ molecules cm}^{-3}$, $2.4 \times 10^{13} \text{ molecules cm}^{-3}$, and $4.3 \times 10^{13} \text{ molecules cm}^{-3}$, $2.9 \times 10^{13} \text{ molecules cm}^{-3}$, $5.7 \times 10^{13} \text{ molecules cm}^{-3}$, $7.1 \times 10^{13} \text{ molecules cm}^{-3}$, $8.5 \times 10^{13} \text{ molecules cm}^{-3}$. An exponential function (thin lines) is used to fit the radical decay and obtain the k_{1st} value using Equation 1.

2.8 CN Radical as a Temperature Proxy

The CN radical was chosen for its proven use as a temperature probe⁶⁹ and its clear rovibronic transition spectra. The quasi-static cell was used to confirm the viability of the CN radical as a temperature probe for use in the fast-flow cell. The cell temperature is monitored and controlled using a type-K thermocouple placed near the laser overlap area. Heating tape is wrapped around the reaction cell to resistively heat the reaction zone. Waiting 1 hour between the temperature changes is required for the temperature to stabilize. The temperature readout from the thermocouple is confirmed by rotational line fitting of the R_{21} branch of the $B^2\Sigma^+ (v' = 0) \leftarrow X^2\Sigma^+ (v'' = 0)$ rovibronic transition of the CN radical with the PGOPHER.⁷⁰ Rotationally resolved vibronic spectra are obtained at 30 μ s laser delay time by scanning from 386.0 nm to 387.8 nm at increments of 0.001 nm. The laser power over the wavelength range varies less than 5%, for which the overall signal has been normalized for prior to fitting by PGOPHER. Each data point in a spectrum represents the average of 10 laser shots.

2.8.1 PGOPHER Simulations and Fitting of Experimental Spectra

PGOPHER is a rotational spectral simulation and fitting program that has been used successfully to fit rotational spectra and determine temperatures from other chemical species.^{62,63} A simulated spectrum is first generated by using the published ground and excited state rotational constants of the radical. The rotational constants needed for the PGOPHER program is the rotational constant B , the energies of the ground and excited states of the radical, and the temperature. The value of the rotational constant B for the ground $B^2\Sigma^+$, ($v = 0$) state⁷¹ is 1.8997 cm^{-1} while B and minimum electronic energy of the excited state is 1.9739 cm^{-1} , and 25752.0 cm^{-1} ,⁷² respectively.

The simulated transitions are then assigned to the experimental spectrum. The rotational constant values are then allowed to float in order to obtain the best fit of the transition frequencies. The optimum values of both B and the electronic energy are within $\sim 1\%$ of the initial literature values. Following the transition assignments, the rotational constants are held fixed. The experimental transition intensities and widths are then fit by floating the temperature and gaussian line widths. Approximately 20 rotational transitions of the R -branch are used in order to determine the rotational temperature. Figure 2.13 shows a comparison of an experimental spectrum (top) with the PGOPHER fit (bottom) resulting in an experimentally determined temperature of 440 ± 5 K. The temperatures reported are the average of the fit temperature of at least three separate laser power normalized CN spectra with the error reported to 2σ . It is of note that the temperature reading of the thermocouple has a positive bias when compared to the CN rotational temperature which increases considerably with temperature.

Figure 2.14 shows the rotationally fit temperature as a function of the temperature read from the thermocouple. Room temperature spectra return fit temperature of approximately 300 K while at higher temperature, the bias between the thermocouple reading and the spectral temperature appears to be proportional to the CN rotational temperature. The spectroscopically determined temperature of 440 K had a thermocouple reading of 500 K. The positive bias is likely to be due to the combination of the position of the thermocouple slightly off from the intersection of the lasers and the inability to fully heat the center of the gas flow where spectra are taken. Similar heating issues been observed in a high-pressure gas reactor with a laminar flow of nitrogen.

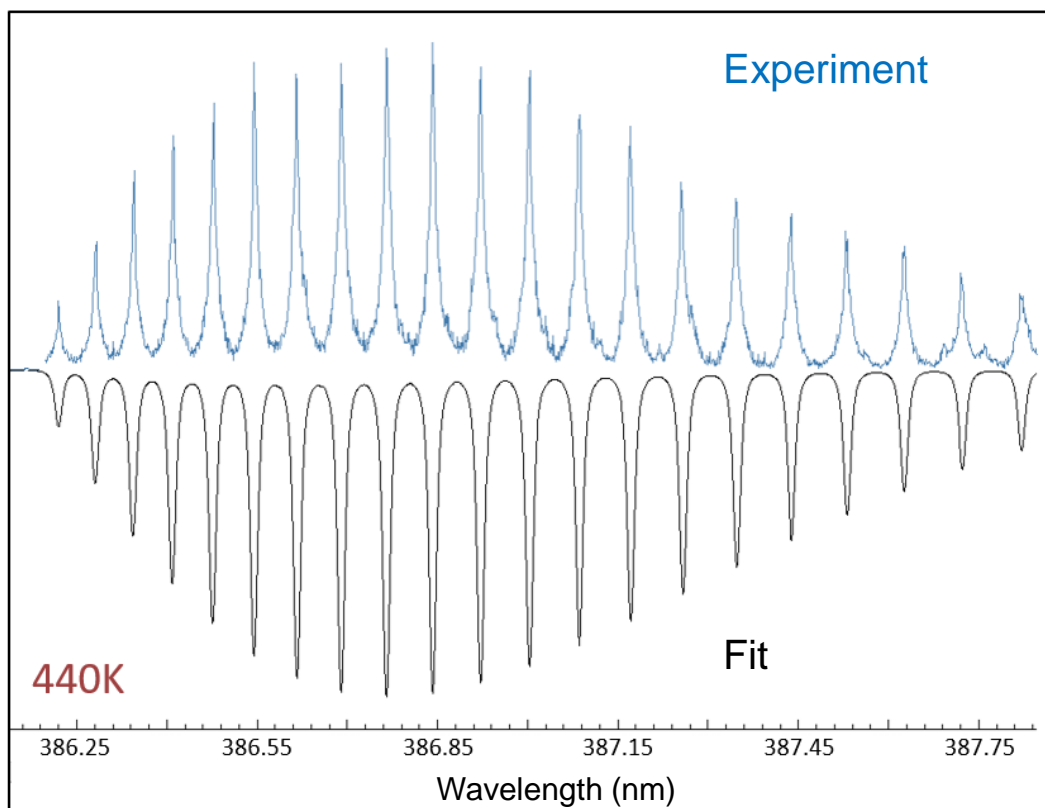


Figure 2.13. Experimental (top) and simulated (bottom) CN LIF spectrum of the R-branch of the $B^2\Sigma^+, v=0 \leftarrow X^2\Sigma^+, v=0$ transition. The CN radical is produced from the photolysis of ICN at 266 nm in Ar at 5 Torr and detected at 420 nm. The simulation returns a rotational temperature of 440 K.

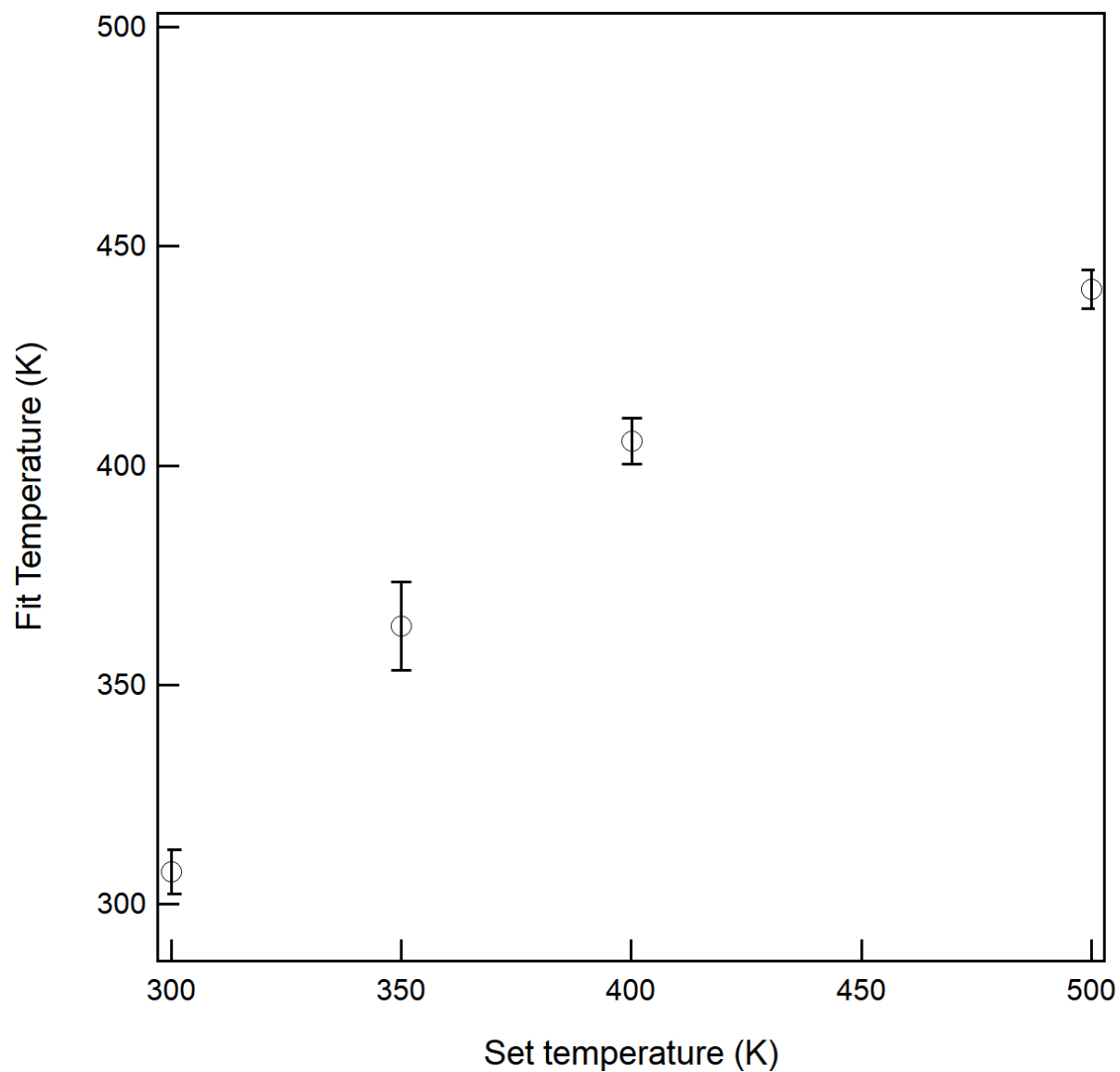


Figure 2.14. Temperature characterization of the quasi-static small cell using PGOPHER fits of experimental rovibronic spectra of the CN radical.

2.9 Computational Methods

More and more studies are being performed with the intent of understanding the underlying mechanisms and properties of the reactions in addition to the measurement of rate coefficients and products. To this end, theoretical calculations are performed for the CN + 2-methylfuran radical using the Gaussian 09 suite of programs. The Gaussian 09 suite of programs⁶² is a

computational chemistry software that is used to calculate the energetics of various chemical species. In this work, it is used to calculate a part of the $\text{CN}(\text{X}^2\Sigma^+) + 2\text{-MF}$ potential energy surface. Geometry optimizations and frequency calculations of stationary points are performed using DFT methods at the B3LYP/CBSB7 level.⁷³ All stationary points are characterized as first-order saddle points or local minima from the resulting vibrational frequencies. Single-point energy calculations are performed using the composite CBS-QB3 method. Transition states are confirmed by the presence of an imaginary frequency. Intrinsic Reaction Coordinate (IRC) calculations are performed at the B3LYP/6-31G(d) to confirm the validity of the transition state after single-point energy calculations. No transition states were located for the entrance channels of the reaction.

2.10 MESMER

The simple modelling of the energetics of a reaction cannot accurately predict the course that a reaction will take. The Master Equation is used to determine probabilistic states for the steps of a given reaction using the potential energy surface obtained from gaussian. Mesmer⁷⁴ is an open-source Master Equation solver that provides solutions to the Master Equation and gives valuable information about the reaction such as the relative ratios of products. Mesmer performs simulations over multi-well molecular energy surfaces that can take into account variables such as bath gas effects in conjunction with temperature. Figure 2.15 depicts a description of the probabilistic process involved in MESMER calculations. To put it simply, MESMER predicts the probability of moving between any energy state well for all energy wells, allowing for time-resolved representation of a chemical reaction.

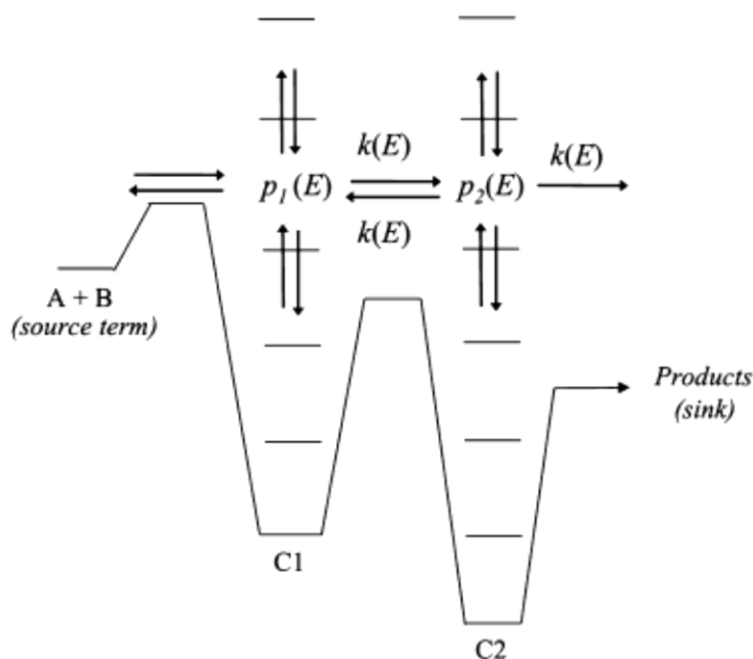


Figure 2.15. Schematic of MESMER probability calculations. Variables such as the energy of the species, temperature of the gas, and effect of the bath gas are taken into account to determine the probabilities of proceeding down certain reaction pathways.

2.11 Product Detection Experiments

A complete understanding of a reaction involves knowledge of the products as well as the rates of reaction. A powerful technique that is well suited to the study of bimolecular reactions is the technique of multiplexed photoionization mass spectrometry (PIMS), performed in the facilities of the Advanced Light Source (ALS) at Lawrence Berkeley National Laboratories. While product detection is possible by using standard mass spectrometry, it can be difficult or impossible to identify multiple species of the same atomic mass, even with very high mass resolution. The PIMS technique provides the ability to differentiate isomers for chemical reactions in the gas phase by identification of ionization patterns unique to each species. The synchrotron also provides a wide spectrum of wavelengths available where in-house labs would need to identify specific wavelengths of interest. The PIMS apparatus was developed by Osborn et al.⁵⁸ and has

been used extensively for the study of gas phase reactions involving both neutral and radical species. This work involves the use of the PIMS for the purpose of studying radical-radical reactions, which are a class of reactions that has rarely been explored due to the difficulty in experimental setup.

2.12 Multiplexed Photoionization Mass Spectrometry (PIMS)

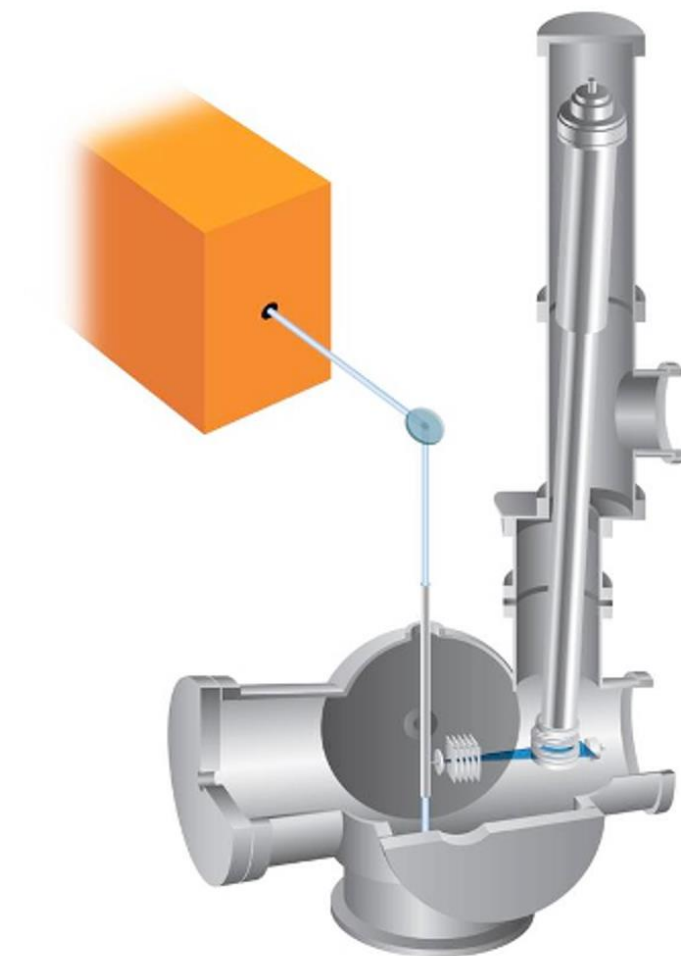


Figure 2.16. Schematic of the multiplexed photoionization mass spectrometer at the Advanced Light Source. Image source from Osborn et al.²

Figure 2.16 depicts a schematic depiction of the experiment shown in Osborn et al.⁵⁸ The reaction apparatus comprises four main sections: the reactor and vacuum system, the photoionization source, the time-of-flight mass spectrometer, and the ion detector and data

acquisition system. The reactor consists of a 62 cm long quartz tube with a 1.05 cm inner diameter whose flow is controlled by calibrated mass flow controllers. Pressure in the reactor tube measured by a capacitive manometer and controlled with a feedback valve throttling a Roots pump. A pinhole in the side of the quartz tube forms an effusive molecular beam that is ionized by the VUV quasi-continuous synchrotron radiation. The ions are detected using an orthogonal-acceleration time-of-flight mass spectrometer (TOF-MS) when they strike the active time- and position-sensitive microchannel plate (MCP) detector.

The reactor tube is wrapped in nichrome heating tape and regulated through a thermocouple able to reach temperatures between 300 – 1050 K. Experimental conditions in the tube were put between 298 K and 500 K with a total flow of 100 sccm and maintain a number density of $1 \times 10^{17} \text{ cm}^{-3}$. The experiment is synced to a KrF excimer laser that pulses at 4 Hz or 10 Hz that fires along the length of the flow tube to generate the reactant radical species. The KrF excimer laser can be tuned to 193 nm, 248 nm, and 351 nm with a fluence range of 10 – 60 mJ cm^{-2} . The resulting signal is background-subtracted and normalized by the photon flux which is monitored by a VUV photodiode.

2.14 3D Data Collection

The experimental apparatus at the ALS allows collection of information along three variables: Ion intensity vs mass-to-charge ratio (m/z), kinetic time (t), and photon energy (E). Time resolved concentration data and photoionization spectra can be obtained at specific masses using the 3D data, allowing for isomeric resolution at masses of interest. When photoion data is obtained for a specific mass, the signal contains contributions from the weighted photoionization spectra of all isomers present. The identities and relative concentrations of the

isomers produced by a reaction can be obtained from using their known or calculated photoionization spectra by fitting the weighted contributions of each isomer to the experimental data at that mass. If the absolute ionization cross sections are known, it is possible to obtain branching ratios of the products.

References

- (1) Agúndez, M.; Cabezas, C.; Tercero, B.; Marcelino, N.; Gallego, J. D.; de Vicente, P.; Cernicharo, J. Discovery of the propargyl radical (CH₂CCH) in TMC-1: One of the most abundant radicals ever found and a key species for cyclization to benzene in cold dark clouds*. *A&A* **2021**, *647*, L10.
- (2) Slavinskaya, N. A.; Frank, P. A modelling study of aromatic soot precursors formation in laminar methane and ethene flames. *Combustion and Flame* **2009**, *156* (9), 1705-1722. DOI: 10.1016/j.combustflame.2009.04.013.
- (11) Fitzpatrick, E. M.; Bartle, K. D.; Kubacki, M. L.; Jones, J. M.; Pourkashanian, M.; Ross, A. B.; Williams, A.; Kubica, K. The mechanism of the formation of soot and other pollutants during the co-firing of coal and pine wood in a fixed bed combustor. *Fuel* **2009**, *88* (12), 2409-2417. DOI: <https://doi.org/10.1016/j.fuel.2009.02.037>.
- (20) Thapa, J.; Spencer, M.; Akhmedov, N.; Goulay, F. Kinetics of the OH Radical Reaction with Fulvenallene from 298 K to 450 K. *The journal of physical chemistry letters* **2015**, *6*. DOI: 10.1021/acs.jpcllett.5b02417.
- (25) Gligorovski, S.; Strekowski, R.; Barbati, S.; Vione, D. Environmental Implications of Hydroxyl Radicals (center dot OH). *Chemical Reviews* **2015**, *115* (24), 13051-13092. DOI: 10.1021/cr500310b.
- (40) Stone, D.; Whalley, L. K.; Heard, D. E. Tropospheric OH and HO₂ radicals: field measurements and model comparisons. *Chemical Society Reviews* **2012**, *41* (19), 6348-6404. DOI: 10.1039/c2cs35140d.
- (50) Sims, I. R.; Smith, I. W. M. GAS-PHASE REACTIONS AND ENERGY-TRANSFER AT VERY-LOW TEMPERATURES. *Annual Review of Physical Chemistry* **1995**, *46*, 109-137. DOI: 10.1146/annurev.pc.46.100195.000545.

(51) Hanson, R. K.; Davidson, D. F. Recent advances in laser absorption and shock tube methods for studies of combustion chemistry. *Progress in Energy and Combustion Science* **2014**, *44*, 103-114. DOI: 10.1016/j.pecs.2014.05.001.

(54) Burcat, A.; Dvinyaninov, M. Detailed kinetics of cyclopentadiene decomposition studied in a shock tube. *International Journal of Chemical Kinetics* **1997**, *29* (7), 505-514, [https://doi.org/10.1002/\(SICI\)1097-4601\(1997\)29:7<505::AID-KIN4>3.0.CO;2-Y](https://doi.org/10.1002/(SICI)1097-4601(1997)29:7<505::AID-KIN4>3.0.CO;2-Y). DOI: [https://doi.org/10.1002/\(SICI\)1097-4601\(1997\)29:7<505::AID-KIN4>3.0.CO;2-Y](https://doi.org/10.1002/(SICI)1097-4601(1997)29:7<505::AID-KIN4>3.0.CO;2-Y) (accessed 2022/06/20).

(58) Osborn, D. L.; Zou, P.; Johnsen, H.; Hayden, C. C.; Taatjes, C. A.; Knyazev, V. D.; North, S. W.; Peterka, D. S.; Ahmed, M.; Leone, S. R. The multiplexed chemical kinetic photoionization mass spectrometer: A new approach to isomer-resolved chemical kinetics. *Review of Scientific Instruments* **2008**, *79* (10), 104103. DOI: 10.1063/1.3000004 (accessed 2022/06/23).

(62) Frisch, M., Trucks G., Schlegel H, et al. Gaussian 09. Gaussian Inc: Wallingford, CT, 2016, 2022.

(66) Spelay, R.; Adane, K. F.; Sanders, R.; Sumner, R.; Gillies, R. The effect of low Reynolds number Flows on pitot tube Measurements. *Flow Measurement and Instrumentation* **2015**, *45*. DOI: 10.1016/j.flowmeasinst.2015.06.008. Mironov, S. G.; Aniskin, V. M.; Korotaeva, T. A.; Tsyryulnikov, I. S. Effect of the Pitot Tube on Measurements in Supersonic Axisymmetric Underexpanded Microjets. *Micromachines (Basel)* **2019**, *10* (4), 235. DOI: 10.3390/mi10040235 PubMed.

(67) Abhinavam Kailasanathan, R. K.; Thapa, J.; Goulay, F. Kinetic Study of the OH Radical Reaction with Phenylacetylene. *The Journal of Physical Chemistry A* **2014**, *118* (36), 7732-7741. DOI: 10.1021/jp506160p.

(68) Wollenhaupt, M.; Carl, S. A.; Horowitz, A.; Crowley, J. N. Rate coefficients for reaction of OH with acetone between 202 and 395 K. *Journal of Physical Chemistry A* **2000**, *104* (12), 2695-2705. DOI: 10.1021/jp993738f.

- (69) Howle, C. R.; Arrowsmith, A. N.; Chikan, V.; Leone, S. R. State-Resolved Dynamics of the CN(B $2\Sigma^+$) and CH(A 2Δ) Excited Products Resulting from the VUV Photodissociation of CH₃CN. *The Journal of Physical Chemistry A* **2007**, *111* (29), 6637-6648. DOI: 10.1021/jp068544w.
- (70) Western, C. M. PGOPHER: A program for simulating rotational, vibrational and electronic spectra. *Journal of Quantitative Spectroscopy and Radiative Transfer* **2017**, *186*, 221-242. DOI: <https://doi.org/10.1016/j.jqsrt.2016.04.010>. Western, C. M.; Billinghurst, B. E. Automatic assignment and fitting of spectra with pgopher. *Physical Chemistry Chemical Physics* **2017**, *19* (16), 10222-10226, 10.1039/C7CP00266A. DOI: 10.1039/C7CP00266A.
- (71) Thomson, R.; Dalby, F. W. Experimental determination of the dipole moments of the X($2\Sigma^+$) and B($2\Sigma^+$) states of the CN molecule. *Canadian Journal of Physics* **1968**, *46* (24), 2815-2819. DOI: 10.1139/p68-652 (accessed 2022/06/21).
- (72) Engleman, R. The $\Delta v = 0$ and +1 sequence bands of the CN violet system observed during the flash photolysis of BrCN. *Journal of Molecular Spectroscopy* **1974**, *49* (1), 106-116. DOI: [https://doi.org/10.1016/0022-2852\(74\)90100-3](https://doi.org/10.1016/0022-2852(74)90100-3).
- (73) Becke, A. D. A new mixing of Hartree–Fock and local density-functional theories. *The Journal of Chemical Physics* **1993**, *98* (2), 1372-1377. DOI: 10.1063/1.464304 (accessed 2022/06/21).
- (74) Glowacki, D. R.; Liang, C.-H.; Morley, C.; Pilling, M. J.; Robertson, S. H. MESMER: An Open-Source Master Equation Solver for Multi-Energy Well Reactions. *The Journal of Physical Chemistry A* **2012**, *116* (38), 9545-9560. DOI: 10.1021/jp3051033.

Chapter 3: Reaction of the CN $X^2\Sigma^+$ ($v'' = 0$) Radical with 2-methylfuran

3.1 Generation of the CN Radical

The CN radical in its ground electronic state ($X^2\Sigma^+$) is generated by photodissociation of ICN at 266 nm by the fourth harmonic of a Nd:YAG laser. The CN radical is then excited on the $B^2\Sigma^+$ ($v' = 0$) $\leftarrow X^2\Sigma^+$ ($v'' = 0$) vibronic band at 386.3 nm using a frequency doubled and 355-nm pumped dye laser with LDS 765 dye (Exciton). The $B^2\Sigma^+$ ($v' = 0$) $\rightarrow X^2\Sigma^+$ ($v' = 1$) emission from the excited state CN radical is collected by the PMT through a 420 ± 2 nm band-pass filter. The time-resolved fluorescence is collected 500 ns after the pump laser and averaged (SRS 250 Boxcar integrator) within a 250 μ s gate. Radical concentration temporal profiles are obtained by changing the time delay between the pump and probe lasers using a delay generator (SRS DG535). Timing for the firing of the two lasers are controlled by a pulse generator (Stanford Research DG535). Delay intervals are increased by 5- μ s steps with delay times starting at -50 μ s and ending at 1500 μ s with respect to the photolysis laser. The decays are fit to an exponential function from 30 μ s to 1500 μ s. Though the vibrationally excited CN $X^2\Sigma^+$ ($v = 1$) state is only approximately 1.2% of the radicals produced from the laser,⁵³ delay times shorter than 30 μ s are not included in the exponential fit to avoid any effect from relaxation of the vibrationally excited state. The 2-methyl furan concentrations are varied for different trials of the experiment to obtain the second-order rate coefficient at fixed temperature and pressure. The experimental procedure and setup have been validated by determination of the second-order reaction rate coefficient of the CN radical with propene (C_3H_6). The second order k_{2nd} value for

the reaction between the CN radical and propene is measured to be $2.39 (\pm 0.04) \times 10^{-10} \text{ cm}^3$ molecules s^{-1} and is in good agreement with previous studies.^{33,35,36,39,47,51}

3.1 CN Radical + 2-Methylfuran Kinetic Study

Figure 3.1 displays measured pseudo-first order rates k_{1st} as a function of the 2-MF number density ranging from 0.0 to 7.4×10^{13} molecules cm^{-3} at room temperature and 5.34 Torr. The resulting plot shows a clear linear trend, validating the use of the pseudo-first order approximation. Each data point represents the average of at least three independent data set k_{2nd} values reported with 2σ error bars. The overall second-order rate constant is obtained by

fitting the data to Eq. 2.5.

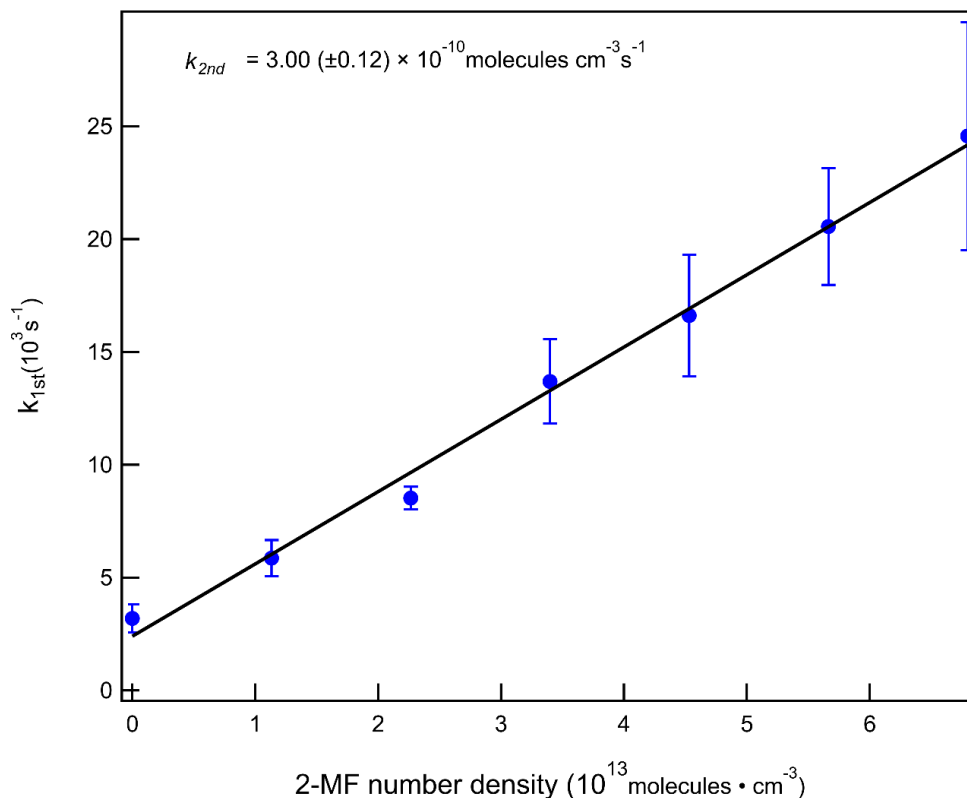


Figure 3.1. Pseudo-first order rate coefficients of the CN + 2-MF reaction as a function of 2-MF number density at 304 K and 5.34 Torr. The vertical error bars are reported to 2σ . The black solid line is a linear fit of k_{1st} values resulting in a 2nd order rate coefficient

3.2 Fluence Dependence

Photodissociation of 2-MF may lead a decrease of the 2-MF concentration and bias the measurement of the rate coefficient. In addition, the photolysis decomposition products may also react with the CN radical and interfere with the kinetic measurements. The absorption cross section of 2-MF has been measured to be $2.82 \times 10^{-19} \text{ cm}^2$ at 266 nm.⁶⁷ At the highest 266-nm fluence (total energy per unit surface area) used in this experiment (62 mJ cm^{-2}), the amount of 2-MF photodissociation is estimated to be less than 1%. Nonetheless, in order to confirm the lack of 2-MF photodissociation, the k_{2nd} values are measured as a function of laser fluence. Figure 3.2 displays the measured rate coefficients as a function of laser fluence over the 19–62 mJ cm^{-2}

range. Laser fluence was varied by increasing the time delay between the flash lamp and Q-switch of the Nd:YAG laser at 266 nm and measuring the power of the resulting beam. The laser fluence was measured before the reaction cell and is likely to be lower at the reaction zone. Within the 2σ error bars and over the experimental fluence range, the rate coefficient shows no apparent laser fluence dependence.

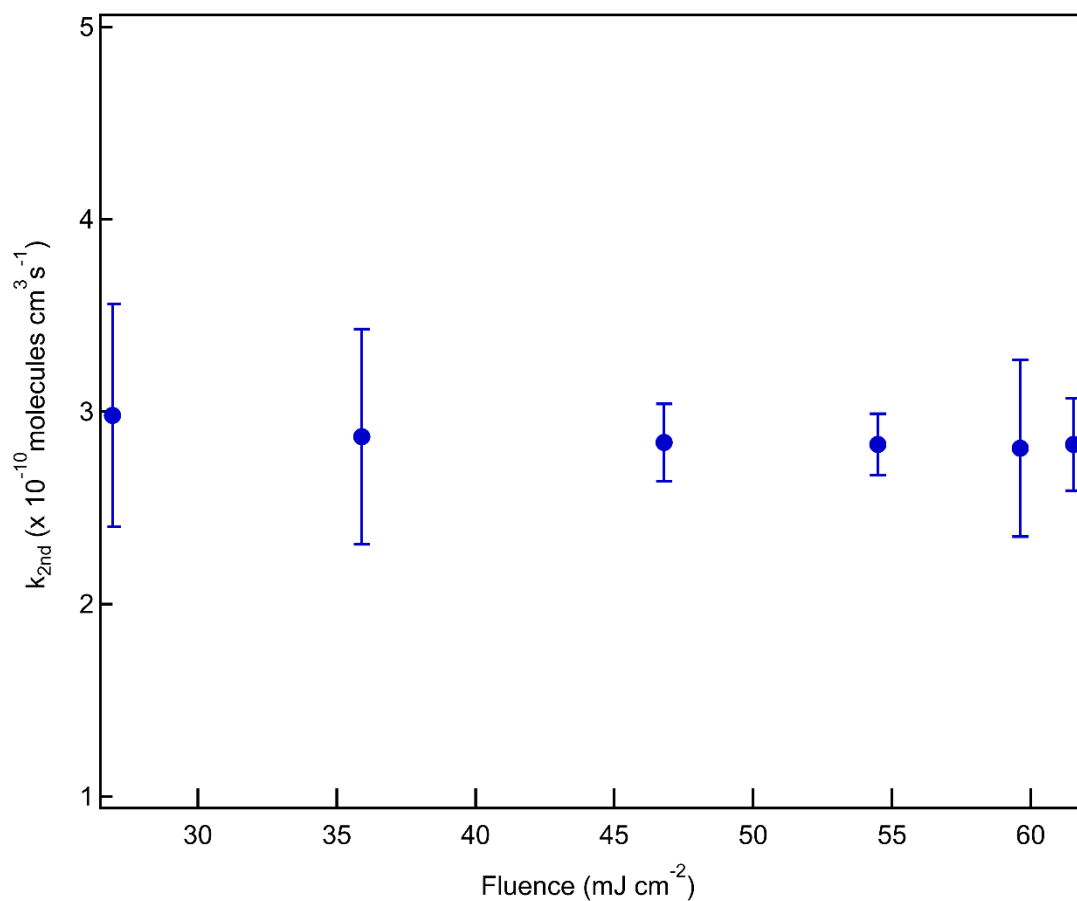


Figure 3.2. Second order rate coefficients of the CN + 2-Methylfuran reaction as a function of laser fluence at 304 K and 5.34 Torr. The vertical error bars are reported to 2σ .

3.3 Pressure and Temperature Dependence

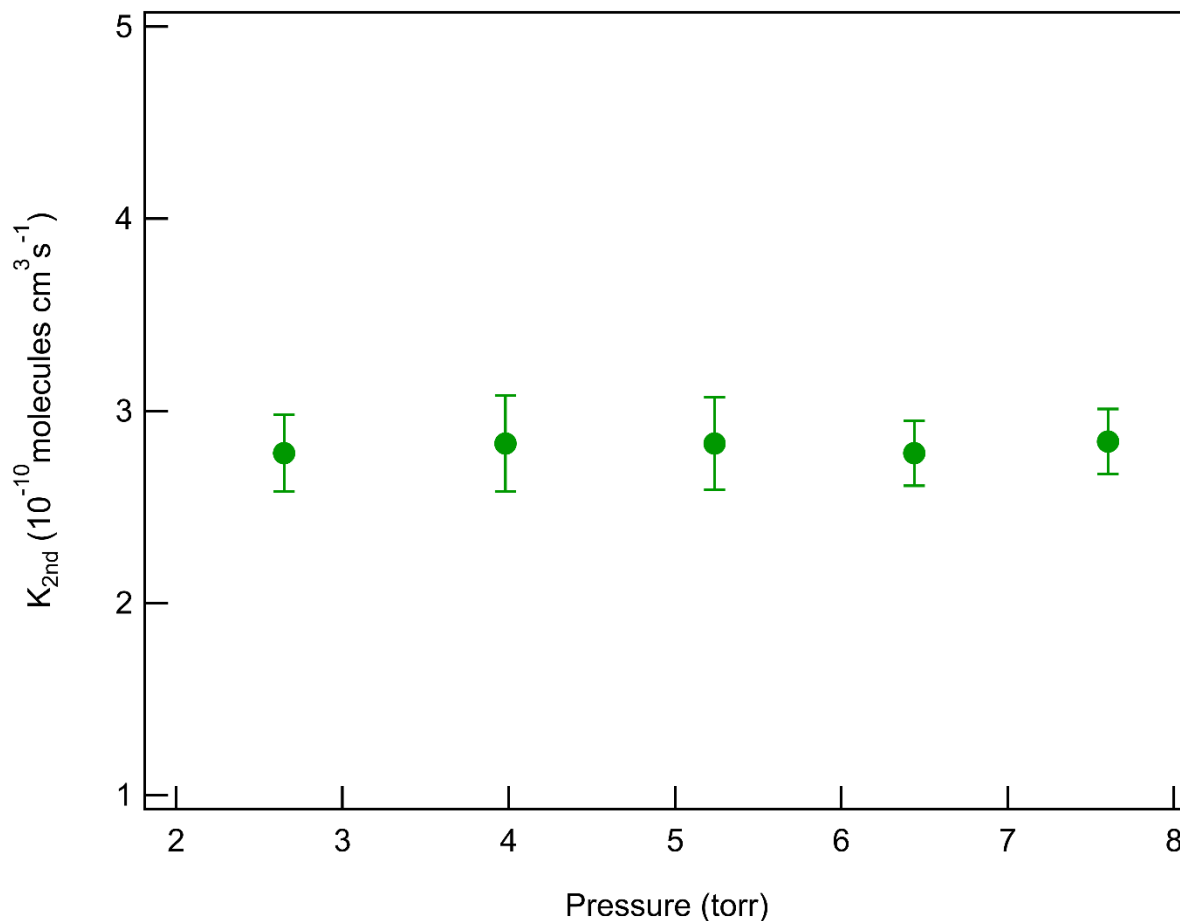


Figure 3.3. Second order rate coefficients of the CN + 2-Methylfuran reaction as a function of pressure at 304 K. The vertical error bars are reported to 2σ .

Figure 3.3 displays the pressure dependence of the CN + 2-MF rate coefficient over the 2.7–7.6 Torr range at room temperature. The measurements are in good agreement within 2σ error. Figure 3.4 displays the temperature dependence of the CN + 2-MF rate coefficient over the 304–440 K range, reported to 2σ error. Horizontal error bars represent the rate obtained from the average of at least 3 rotational temperatures. Each value represents the average of at least three separate data points with error bars of 2σ . There is good agreement of the rate constants within the error over the specified temperature range, suggesting no temperature dependence within that experimental range.

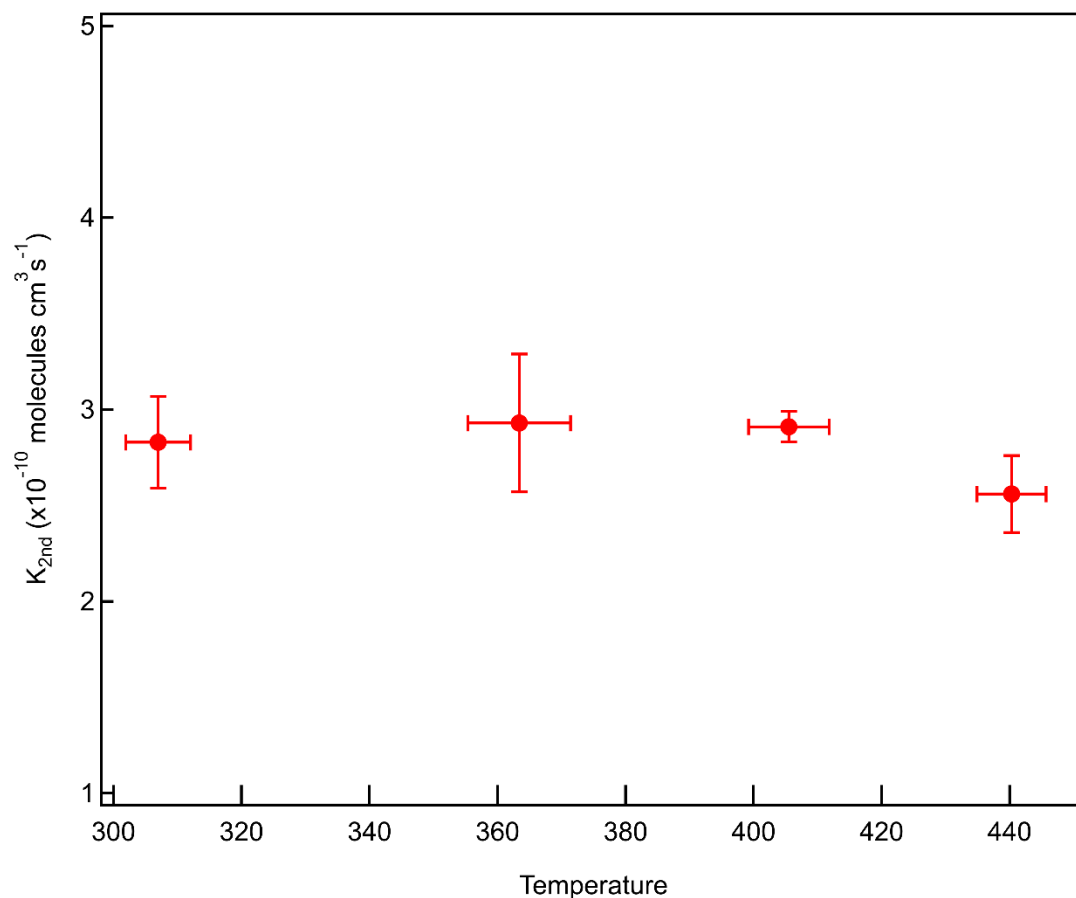


Figure 3.4. Second order rate coefficients of the CN + 2-methylfuran reaction as a function of temperature at 5.44 Torr. The vertical and horizontal error bars are reported to 2σ precision.

3.4 CN ($B^2\Sigma^+$) + 2-methylfuran Potential Energy Surface

A portion of the 2-MF potential energy surface (PES) is calculated for the CN radical addition and insertion reaction mechanisms at the CBS-QB3 level of theory. Figure 3.5 displays the PES for the addition-elimination pathways of the CN radical into the C1 and C3 double bonds (See SI for carbon numbering). The addition mechanism is found to proceed through four barrierless entrance channels to form nitrile-substituted intermediates: INT1, INT2, INT3, and INT4. The reaction pathways culminate in four exit channels that proceed through either H elimination to form 5-methyl-2-furonitrile (P1), 5-methyl-3-furonitrile (P2), and 5-methyl-4-furonitrile (P3), or

CH₃ elimination to form 2-furonitrile (P4). Formation of INT1 and INT4 are the most exothermic due to resonance in the structures. INT1, INT2, and INT3 can proceed through the correspondingly numbered transition states to eliminate a hydrogen atom and form the isomeric products P1, P2, and P3, respectively. INT4 can form product P4 through methyl elimination with a transition state TS4. The formation of 5-methyl-2-furonitrile (P1) is the highest energy product of the H-elimination pathways. Formation of 2-furonitrile (P4) is the most thermodynamically feasible product with an energy 112.2 kJ mol⁻¹ lower than the reactants.

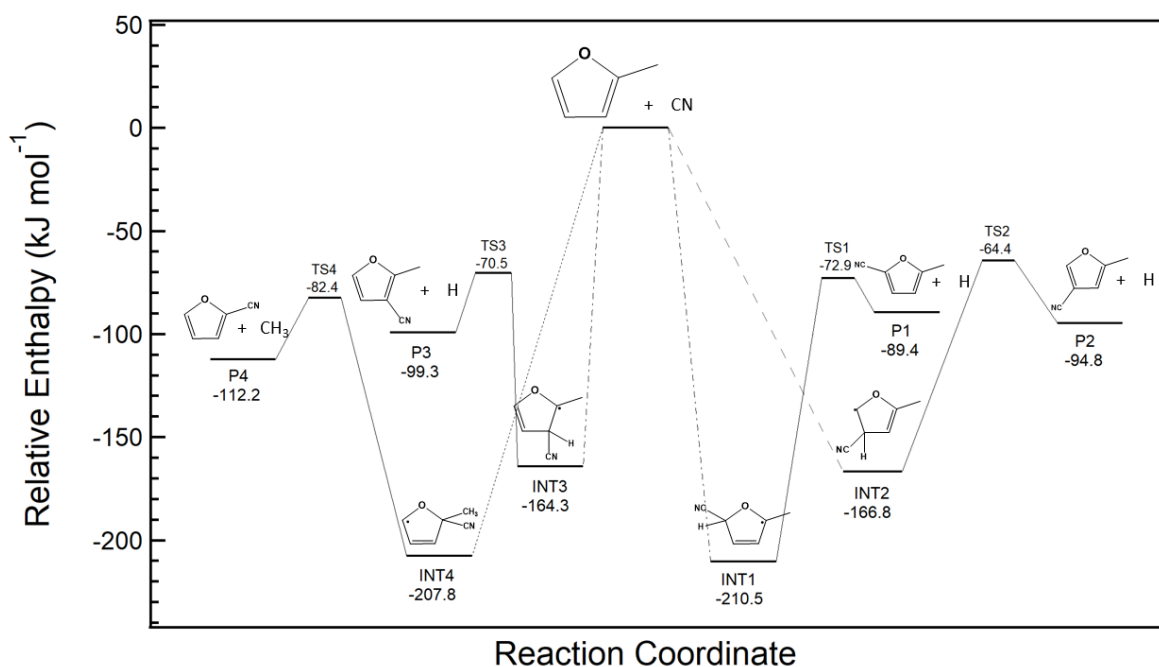
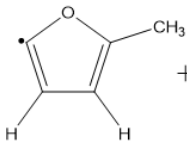
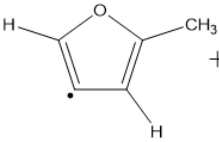
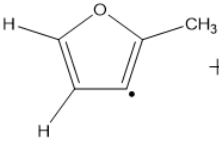
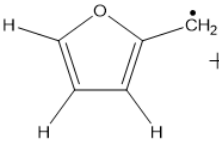


Figure 3.5. A portion of the CN + 2-MF potential energy surface for addition of the CN radical onto 2-methylfuran unsaturation.

The products and enthalpies of reaction for the CN abstraction pathways are displayed in Table 3.1. All four abstraction products are thermodynamically favorable compared to the reactants. H-abstraction from C2, C3, and C4 sites result in products of similar enthalpies while H-abstraction from the methyl substituent (C1) forms the most enthalpically stable product with

a reaction enthalpy of $-170.0 \text{ kJ mol}^{-1}$ relative to the reactants. This is due to the delocalization of the electron from C2 to the ring and resonance stabilization.

Table 3.1. Abstraction pathways for the CN + 2-methylfuran reaction with corresponding enthalpies

H Abstraction Products	$\Delta_r H$ (298)(kJ mol ⁻¹)
	-28.8
	-28.3
	-27.8
	-170.0

3.5 Discussion of Reaction Characteristics

The CN ($X^2\Sigma^+$) + 2-MF reaction is studied over the 2.7–7.6 Torr pressure and 304–440 K temperature ranges. There are no apparent pressure and temperature dependencies, with a measured average rate coefficient of $2.83 (\pm 0.18) \times 10^{-10} \text{ cm}^3 \text{ molecules s}^{-1}$ over both pressure and temperature ranges. The CN radical temporal decays are well fit to exponential functions,

demonstrating that there is negligible back dissociation of the adduct, compared to the nonexponential decays observed by Trevitt et al.³⁵ in the case of the reactions with toluene. Figure 3.6 displays the rate coefficients for reaction of the CN radical with a series of unsaturated hydrocarbons from previous studies.^{32, 37, 75} The CN + 2-MF reaction rate coefficient is found to be similar to that of the CN radical reactions with propylene and ethylene but lower than the reaction rate coefficient measured for CN with other species with conjugated π -bonds. This shows that the additive trend suggested by Yang and Lin⁴⁵ does not seem to apply to the CN + 2-MF reaction.

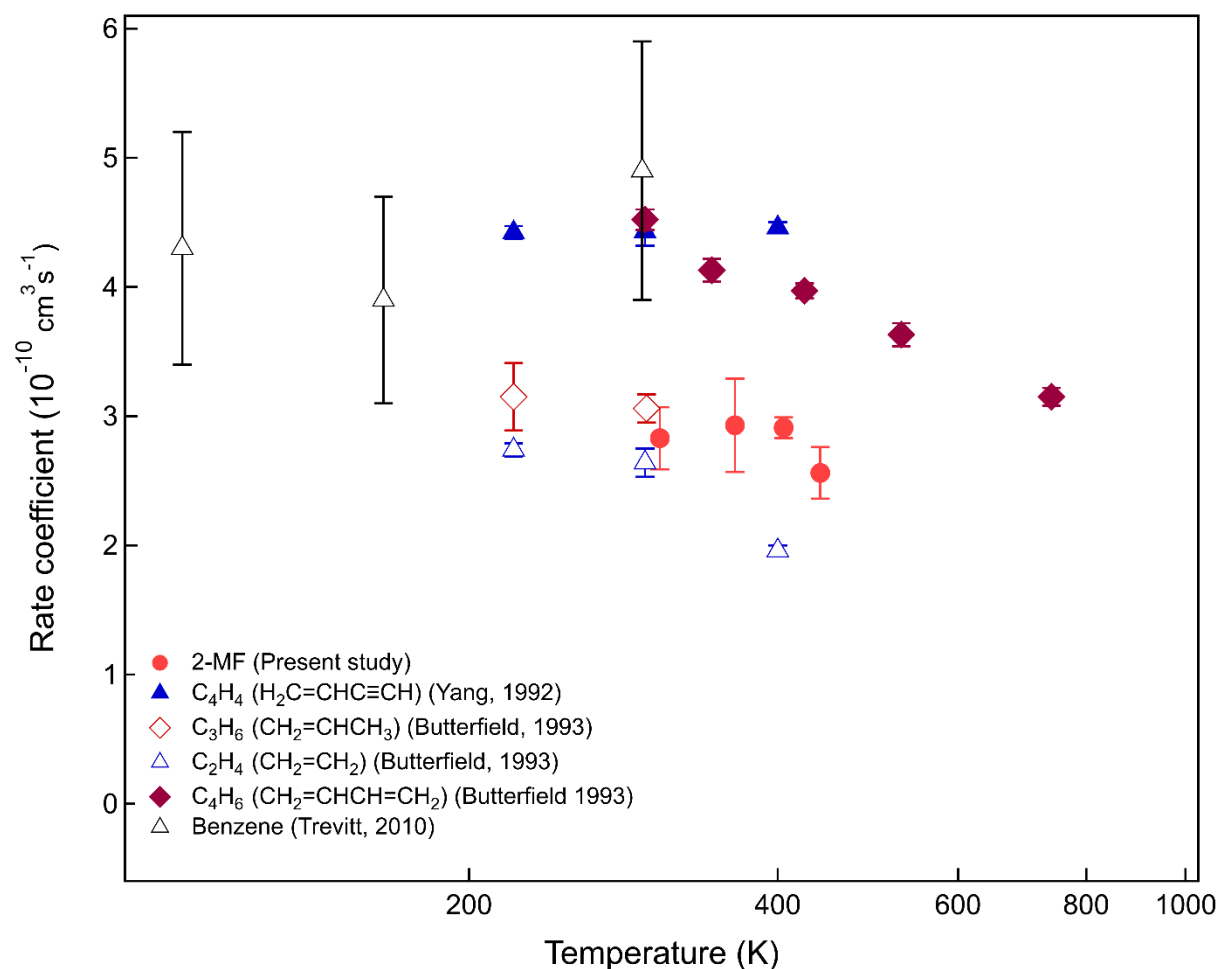


Figure 3.6. Experimental bimolecular rate constants of CN vs. temperature for selected hydrocarbons.

The reaction rate coefficient of the CN + 2-MF is also slightly lower than that for reactions with benzene at room temperature. In the case of the OH radical, the reaction with 2-MF at room temperature⁷⁶ is found to be faster than the reactions with both benzene⁷⁷ and toluene.⁷⁸ This may be explained by an increased reactivity of the 2-MF toward OH due to the increased stabilization of intermediates from the electron donating effect of the ether group.⁷⁹ This difference in trend between the CN and the OH radicals is likely to be due to the difference in initial adduct formation between the two radicals. The OH radical is known to form pre-reactive complexes with aromatic rings.⁶⁷ As observed in the case the CN + benzene reaction,³⁵ the radical is more likely to directly add on one of the carbon atoms⁸⁰ without formation of a pre-reactive complex, therefore minimizing the electron donating effect of the ether group observed for OH association reactions.

Kinetic measurements of OH radical reactions with furan, 2-MF, and 2,5-dimethylfuran performed by Bierbach et al.⁷⁶ show an increase in rate coefficients from least to most substituted reactant. This is due to the electron donating effect of the alkyl groups on the resonance stabilized ring. Although there is no kinetic data available for the CN + furan reaction, such a trend is unlikely to be observed because of the difference in reaction mechanism between the two radicals. In the case of benzene and toluene, substitution of an H atom for a methyl group decreased the reaction rate coefficient by a factor of ~3. One possible explanation is the increased attractive dipole-dipole potential between the CN radical and the methyl group drawing the CN radical to the methyl group but failing to overcome the barrier involved in abstraction. Similar processes may explain why the rate of CN + 2-MF has a lower rate coefficient than that of CN + benzene or other conjugated hydrocarbons, as observed in Figure 3.6. Kinetic

studies of CN + furan would give greater insight into the dominant reaction mechanism of CN + 2-MF and similar species.

The most highly exothermic pathways for the CN + 2-MF reaction are addition-elimination pathways (see Table 3.1 and Figure 3.5). Of these exothermic pathways, the most enthalpically favorable are the pathways with intermediates that have the nitrile group on the carbons adjacent to the oxygen atom (INT1 and INT4). INT 1 and INT4 both have 2 resonance forms that allow for increased stabilization while both INT2 and INT3 have no additional forms. One of the resonance forms of INT1 has the radical positioned on the methyl-substituted vinyl carbon which allows both the oxygen and methyl groups to stabilize the structure through electron donation. The radical site in INT4 is stabilized only by the oxygen atom, leading to a slightly decreased stabilization relatively to INT1. While the stability of INT1 and INT4 are similar, the methyl elimination pathway is lower in energy when compared to H-elimination pathways, leading to the formation of 2-furonitrile (P4) as the most thermodynamically favorable pathway. In this case, the larger exothermicity of the methyl leaving group can alleviate the steric strain from the CN addition.³²

No apparent experimental temperature dependence of the reaction is found over the range of 304–440 K, indicating a very small or nonexistent potential energy barrier. The absence of a transition state on the computed potential energy surface for the entrance channel is consistent with this result, though the level of theory employed is insufficient to definitively determine the presence of a small energy barrier. Kinetics studies on the reaction of the CN radical with unsaturated hydrocarbons (Figure 3.6) report little to no negative temperature dependence^{32, 37, 45, 75} in agreement with the present measurements.

Abstraction pathways for reactions with the CN radical and unsaturated hydrocarbons are typically endothermic with positive activation energies.^{32, 37, 45, 75} The abstraction of an H-atom from 2-MF is found to be less enthalpically favorable compared to CN addition to the π -bonds. The exception is H-abstraction from the methyl substituent, shown in Table 3.1, the products of which are made more thermodynamically favorable by resonance stabilization. While the transition states for these entrance channels are not found with the level of theory used in this study, other computational and experimental studies support the presence of a small positive activation energy and general unfavourability of the abstraction pathway, even at higher temperatures.^{32, 37, 81} At temperatures above room temperature, most CN reactions with unsaturated hydrocarbons continue to exhibit the negative temperature dependence.^{32, 37, 81} Figure 3.6 shows that the rate coefficients of the CN + C₂H₂ and CN + C₂H₄ reactions were similar and exhibited negative temperature dependencies throughout the temperature ranges studied (294–706 K), implying abstraction does not play a major part even at higher temperatures. It is then unlikely that the CN + 2-MF reaction will proceed through any of the abstraction pathways, and therefore unlikely that the rate coefficient will change with increasing temperature, at least up to 800 K. While the lack of temperature dependence found in this study suggests the rate coefficient will remain temperature independent at higher temperatures, it is difficult to comment with accuracy on the temperature dependency of this reaction outside of the studied range without further studies requiring product detection and Master Equation.

3.6 Conclusion

Pump–probe LIF studies of the rates coefficients for CN + 2-MF reactions are conducted over the temperature range of 304 K to 440 K and the pressure range of 2.2 Torr to 7.6 Torr in a quasi-

static cell reactor. Rate coefficients are observed to be comparable to that of other reactions of the CN radical with unsaturated hydrocarbons and provide valuable insight into the behavior of the CN radical during the combustion of new biofuels. The rate coefficient of the CN + 2-MF reaction at room temperature is pressure independent, which is characteristic of a reaction that occurs at near the collisional limit and lacks a pre-reactive complex. The reaction coefficient is predicted to remain fast even at the higher temperatures of combustion environments. Computational calculations showed submerged energy barriers for the addition-elimination mechanism involving the π -bonds of 2-MF. While there was no temperature dependence found for CN + 2-MF, it is difficult to comment outside the range studied here due to the lack of information regarding the mechanism of reaction. Because the study of CN + toluene was found to be distinctly slower than CN + benzene, there exists an effect of the methyl substituent on the ring. It is likely that CN reactions with unsubstituted furan molecules may occur with rate coefficient higher than those for methyl substituted furans and of the order of those observed for non-cyclic conjugated dienes.

This study provides the experimental reaction rate for the CN + 2-MF reaction to give kinetic insight for a promising fuel alternative. Although further experimental and theoretical studies are necessary to fully quantify the reaction products, the cyano-substitution products are predicted to be the most likely products. 2-MF provides many advantages over both gasoline and ethanol, including high energy density, lack of miscibility in water, and high knock suppression in direct injection engines. The generation 2-MF from nonfood biomass as well as from the combustion of dimethylfuran⁸² gives new urgency to understand the implications of its use. A more complete characterization of the fate of 2-MF in combustion systems is needed prior

to implementation as a replacement fuel. The necessary transition away from fossil fuels to more sustainable sources of energy gives particular significance to this study and warrants the study of similar species.

3.7 References

(32) Ochimizu, T.; Seki, K.; Yagi, M.; Halpern, J. B.; Okabe, H. Rate constants for the reactions of CN with C6–C8 unsaturated hydrocarbons: the relations between the reaction rates and the molecular lengths. *Chemical Physics Letters* **1999**, *313* (3), 451-455. DOI:

[https://doi.org/10.1016/S0009-2614\(99\)00962-8](https://doi.org/10.1016/S0009-2614(99)00962-8).

(35) Trevitt, A. J.; Goulay, F.; Taatjes, C. A.; Osborn, D. L.; Leone, S. R. Reactions of the CN Radical with Benzene and Toluene: Product Detection and Low-Temperature Kinetics. *The Journal of Physical Chemistry A* **2010**, *114* (4), 1749-1755. DOI: 10.1021/jp909633a.

(37) Lichtin, D. A.; Lin, M. C. Temperature dependence of the CN radical reactions with C₂H₂ and C₂H₄. *Chemical Physics* **1986**, *104* (2), 325-330. DOI: [https://doi.org/10.1016/0301-0104\(86\)80176-8](https://doi.org/10.1016/0301-0104(86)80176-8).

(45) Yang, D. L.; Yu, T.; Lin, M. C.; Melius, C. F. The reaction of CN with CH₄ and CD₄: an experimental and theoretical study. *Chemical Physics* **1993**, *177* (1), 271-280. DOI: [https://doi.org/10.1016/0301-0104\(93\)80195-F](https://doi.org/10.1016/0301-0104(93)80195-F).

(67) Abhinavam Kailasanathan, R. K.; Thapa, J.; Goulay, F. Kinetic Study of the OH Radical Reaction with Phenylacetylene. *The Journal of Physical Chemistry A* **2014**, *118* (36), 7732-7741. DOI: 10.1021/jp506160p.

(75) Butterfield, M. T.; Yu, T.; Lin, M. C. Kinetics of CN reactions with allene, butadiene, propylene and acrylonitrile. *Chemical Physics* **1993**, *169* (1), 129-134. DOI: [https://doi.org/10.1016/0301-0104\(93\)80047-D](https://doi.org/10.1016/0301-0104(93)80047-D).

(76) Bierbach, A.; Barnes, I.; Becker, K. H. Rate coefficients for the gas-phase reactions of hydroxyl radicals with furan, 2-methylfuran, 2-ethylfuran and 2,5-dimethylfuran at 300 ± 2 K. *Atmospheric Environment. Part A. General Topics* **1992**, *26* (5), 813-817. DOI: [https://doi.org/10.1016/0960-1686\(92\)90241-C](https://doi.org/10.1016/0960-1686(92)90241-C).

- (77) Anderson, R. S.; Czuba, E.; Ernst, D.; Huang, L.; Thompson, A. E.; Rudolph, J. Method for Measuring Carbon Kinetic Isotope Effects of Gas-Phase Reactions of Light Hydrocarbons with the Hydroxyl Radical. *The Journal of Physical Chemistry A* **2003**, *107* (32), 6191-6199. DOI: 10.1021/jp034256d.
- (78) Bohn, B. Formation of Peroxy Radicals from OH-Toluene Adducts and O₂. *The Journal of Physical Chemistry A* **2001**, *105* (25), 6092-6101. DOI: 10.1021/jp0033972.
- (79) Bruice, P. *Essential Organic Chemistry*; Pearson, 2010.
- (80) Trevitt, A. J.; Goulay, F. Insights into gas-phase reaction mechanisms of small carbon radicals using isomer-resolved product detection. *Physical Chemistry Chemical Physics* **2016**, *18* (8), 5867-5882, 10.1039/C5CP06389B. DOI: 10.1039/C5CP06389B.
- (81) Sayah, N.; Li, X.; Caballero, J. F.; Jackson, W. M. Laser induced fluorescence studies of CN reactions with alkanes, alkenes and substituted aliphatic species. *Journal of Photochemistry and Photobiology A: Chemistry* **1988**, *45* (2), 177-194. DOI: [https://doi.org/10.1016/1010-6030\(88\)80127-8](https://doi.org/10.1016/1010-6030(88)80127-8).
- (82) Lamoureux, N.; Western, C. M.; Mercier, X.; Desgroux, P. Reinvestigation of the spectroscopy of the A³Π_u-X³Σ_g⁻ transition of the NCN radical at high temperature: Application to quantitative NCN measurement in flames. *Combustion and Flame* **2013**, *160* (4), 755-765. DOI: <https://doi.org/10.1016/j.combustflame.2012.12.009>.

Chapter 4: OH + Propargyl Radical Reaction

Product detection of the OH($X^2\Pi$) + propargyl radical reaction were performed using the multiplexed photoionization mass spectrometry (PIMS) at the Advanced Light Source (ALS) located in the Lawrence Berkeley National Laboratories. The experimental apparatus provides sufficient sensitivity needed to study the OH + propargyl radical reaction. There have been few radical-radical reaction experiments as this type of reaction pose multiple logistical challenges to set up. The necessity to create two radicals as reactants creates many more side products than most other reactions due to the creation of two extremely reactive species instead of one. The increased number of products formed through reactions between radicals and precursors and photolysis products makes it difficult to discern which products are formed through the reaction of interest or side products. Optimal conditions were chosen involving the high sensitivity of the PIMS apparatus coupled with precursors that will produce the fewest number of side products.

This study focuses on the product mass of m/z 56 and its isomers at the temperatures of 298 K and 500 K. Identification of the isomers and relative concentrations at m/z 56 are given. The mechanism of reaction is discussed based on the products formed. Branching ratios of the products for m/z 56 as well as other smaller radicals are given and discussed. Comparison between previous computational studies by Pham et al.⁵⁷ and the experimental data obtained are made and discussed.

4.1 OH + Propargyl Radical

Reaction of the OH radical with the propargyl radical were studied under the conditions of 298 K and 500 K, and pressures of 2, 4, 6, and 8 Torr. There was no discernable difference between

pressures on the signal, and as such the information reported in this work were all obtained at 4 Torr. The precursors were irradiated inside of the flow tube at 193 nm for all experimental conditions. The absorption cross section of the propargyl radical is 9 Megabarn or Mb (1 Mb = 10^{-28} m²) at 10.6 eV. The products are sampled from the flow reactor and detected using tunable vacuum ultraviolet photoionization and time-of-flight mass spectrometry. The product mass at m/z 56 of the reaction OH + propargyl is analyzed and the isomers and mechanism discussed.

4.2 Potential Energy Surface of the OH + Propargyl Radical Reaction

The potential energy surface in figure 4.1 is adapted from the work done by Pham et al.⁵⁷ on their computational work of the OH + propargyl radical reaction. The reaction proceeds down an addition pathway and has two barrierless entrance channels available. The OH addition to the “head” side results in the formation of propargyl alcohol forms while the “tail” addition forms allenol. There exists a trans and cis form of allenol that is separated by a small energy barrier of -79.58 kcal/mol. There exists one radical exit channel and two molecular exit channels from propargyl alcohol. The radical exit channel is above the energy of the reactants while the molecular exit channels have transition states just below the energy of the reactants. Allenol can isomerize to form a total of 8 isomers including allenol and not including conformational isomers such as trans or cis forms. The most thermodynamically stable isomer at m/z 56 is trans-acrolein which isomerizes directly from the cis-form of allenol. The most thermodynamically favorable molecular and radical exit channel is C₂H₄ + CO at -107.88 kcal/mol while the most thermodynamically favorable radical channel is the CH₃CH + CO exit channel. The exit channels for the decomposition of these isomers were discussed in detail by

Pham et al.⁵⁷ between the pressures of 100 – 7600 Torr and temperatures between 300 – 2000 K. The overall most abundant product of this reaction at all temperatures and pressures is CO. While Pham et al. discussed the rate coefficients and branching ratios of the potential decomposition channels of the OH + propargyl radical channels, they did not address the intermediates themselves as exit channels for the reaction. The various exit channels observed experimentally during the experiments at the ALS will be discussed the experimental results will be compared to the computational work in the literature.

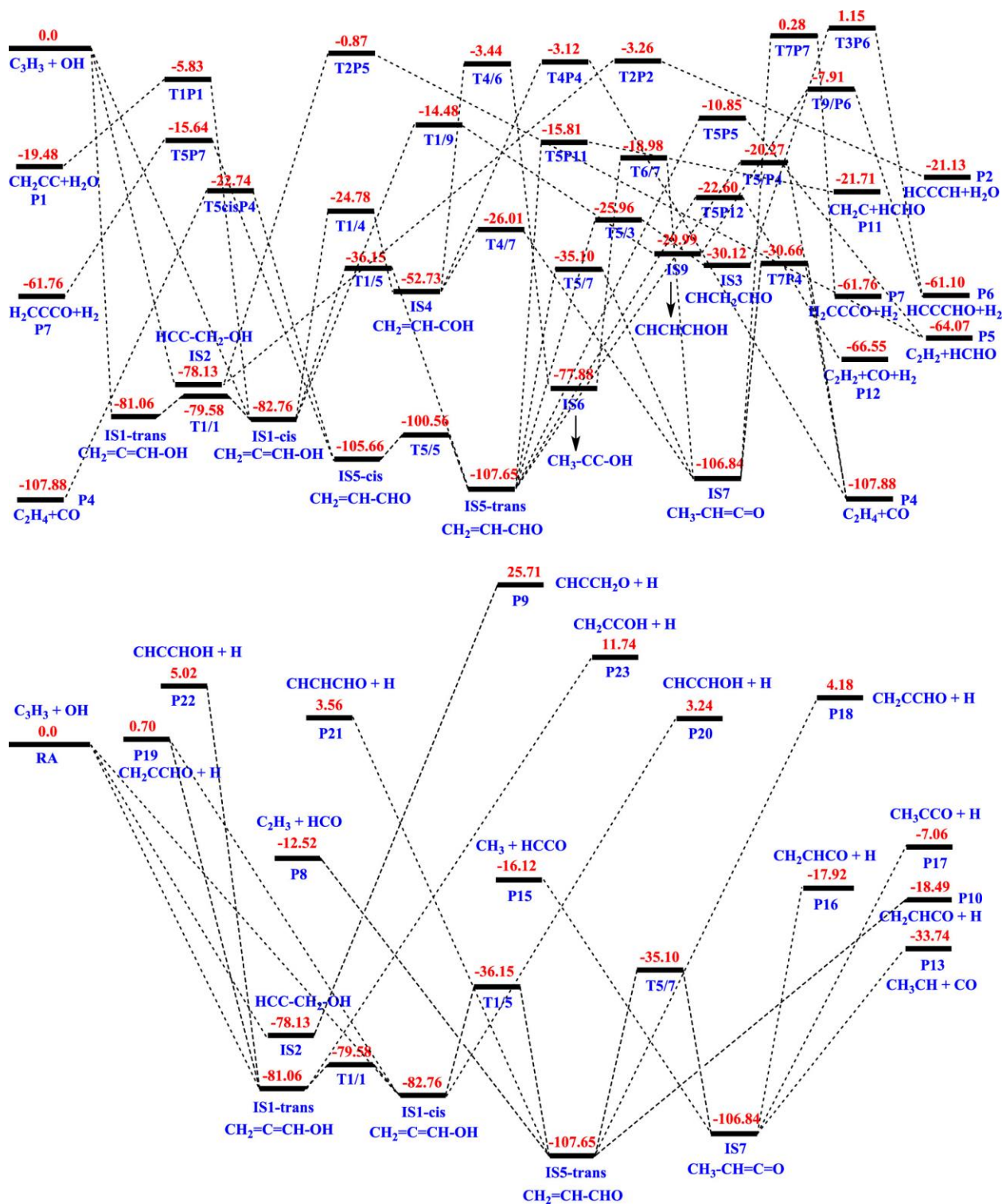


Figure 4.1. Potential Energy Surface for the molecular exit channels (top) and radical exit channels (bottom) adapted from Pham et al.⁵⁹

4.3 Photodissociation of Propargyl Chloride at 193 nm

The mass spectrum for propargyl chloride dissociation without and with the OH radical at 298 K is shown in figure 4.2. The mass spectrum was integrated over the kinetic time of 0 – 20 ms and an energy range of 8.3 – 10.6 eV. Propargyl chloride provides a relatively clean mass spectrum with good signal. The signal at m/z 39 is the propargyl radical, identified by the distinct autoionization patterns in the photoionization spectrum of m/z 39 after 9.0 eV compared with Savee et al.⁵⁹ The photoionization spectra begin to diverge at higher energies, likely due to fluctuations in flow conditions between experiments that were experienced during data acquisition for this experiment. No strong signal is present at m/z 56 which is expected to be the product mass of the reaction. The signal at m/z 78 is assigned to benzene and is the result of the self-recombination reaction with two propargyl radicals, identified by the ionization energy at 9.24 eV.⁸³ The addition of the OH produces additional mass peaks at m/z 26, 27, 28, 29, 30, 54, and 56.

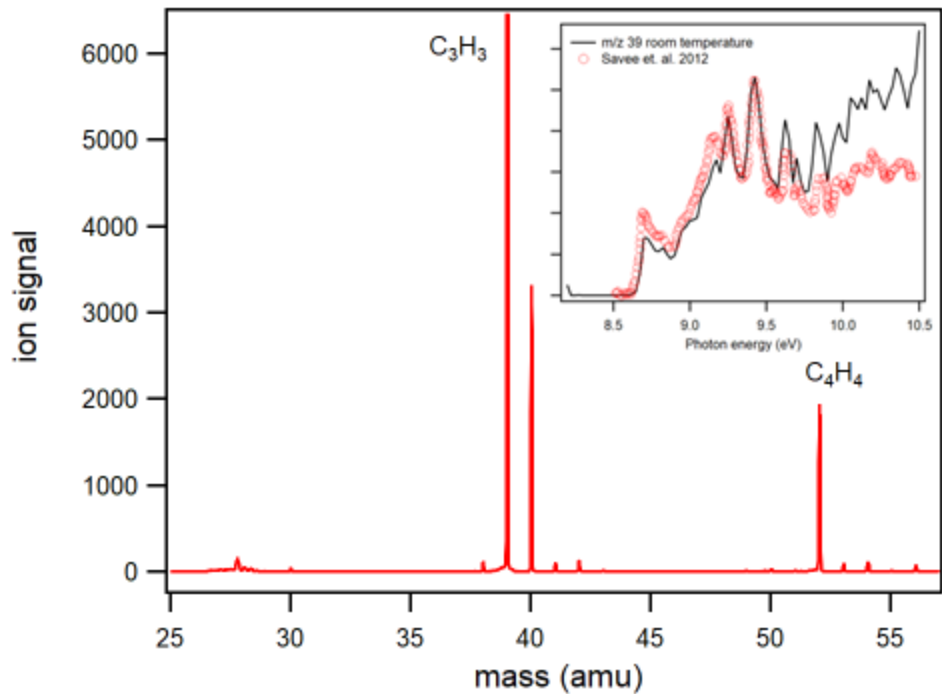


Figure 4.2. Mass spectrum of the photodissociation of C_3H_3Cl with the photoionization spectrum of the propargyl radical.

Figure 4.3 shows the depletion of the signal m/z 39 and the increase of the product mass at m/z 56. M/z 39 shows a clear difference in signal with the addition of the OH radical, while there is a clear increase in signal for m/z 56 with the addition of the OH. The confirmation of the formation of m/z 56 by the reaction between OH and the propargyl radical instead of a reaction with a precursor is confirmed by similar signal formation using other precursors.

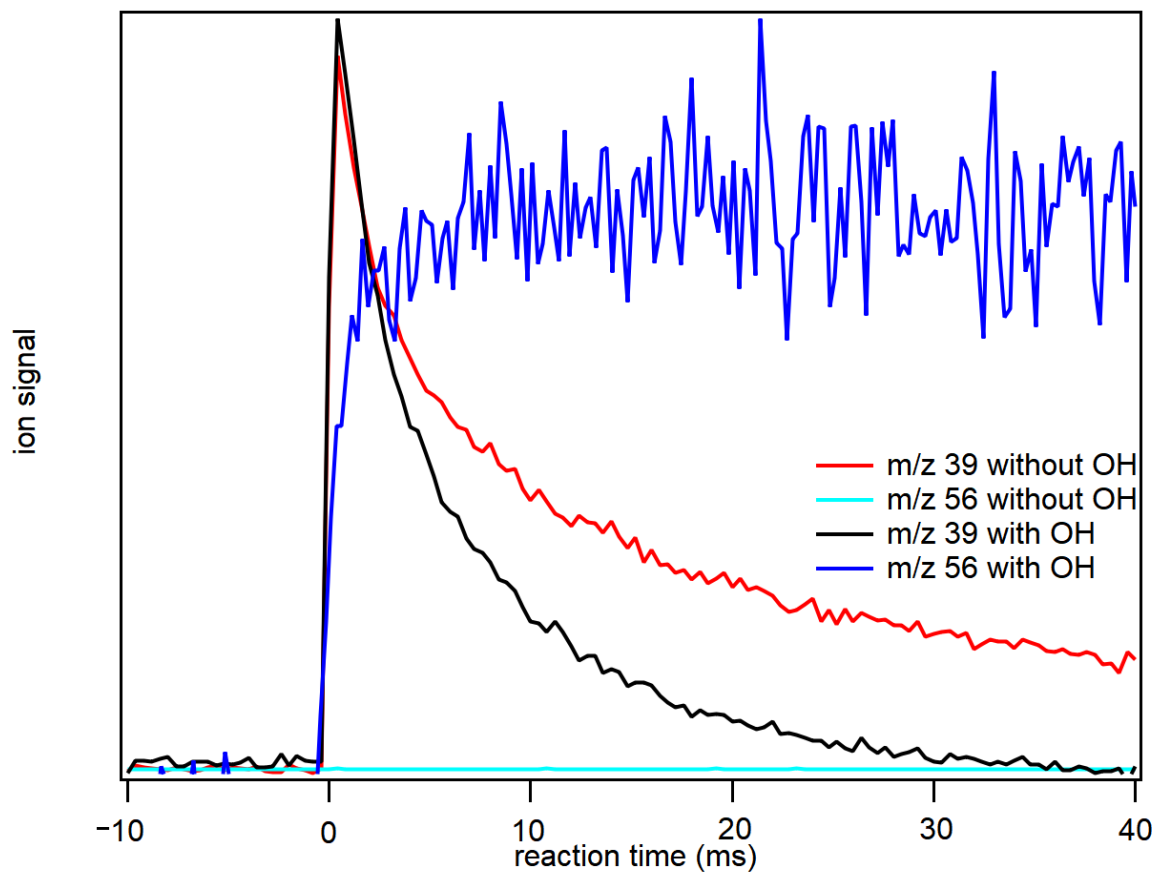


Figure 4.3. Depletion of m/z 39 with and without the OH radical coincidental with the m/z 56 signal increase

4.4 Addition of OH

4.4.1 m/z 56 Isomers at 298 K

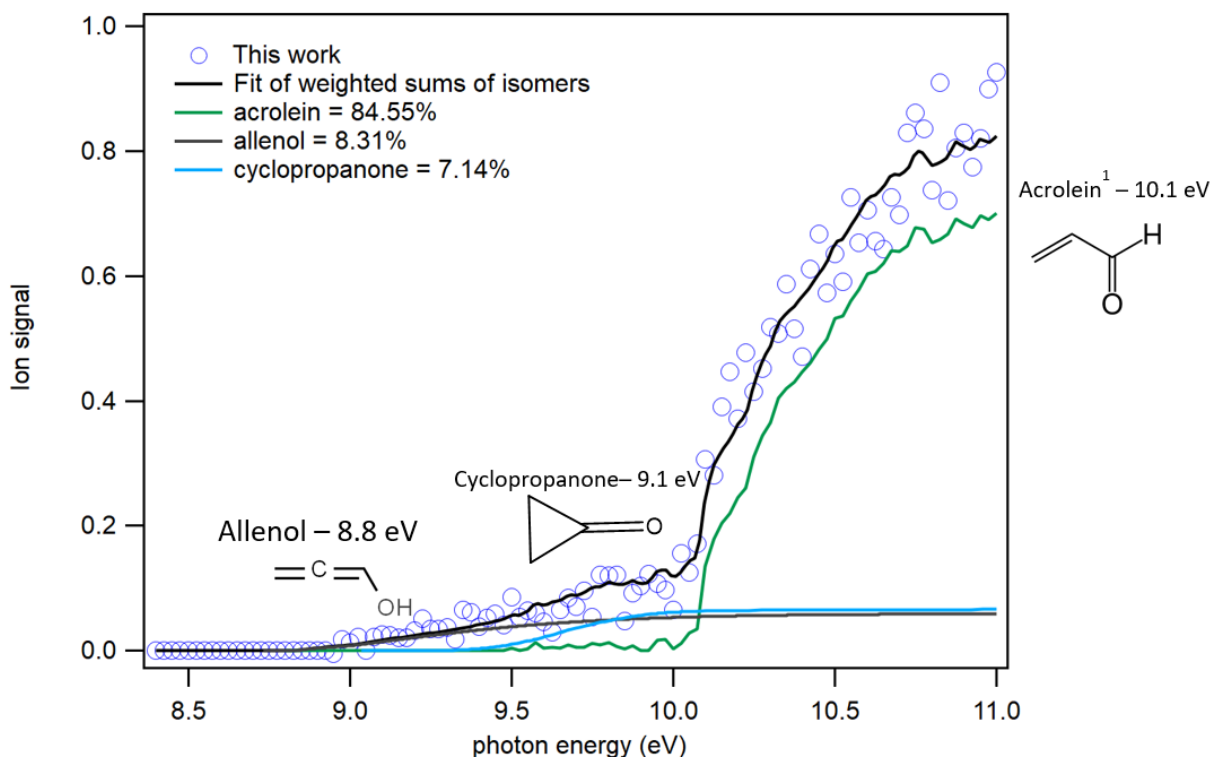


Figure 4.4. Photoionization spectrum (open circles) of m/z 78 ion signal obtained by photolysis of C_3H_3Cl and urea-peroxide complex integrated over 0-80 ms time range. The green line shows the three isomers of acrolein, allenol, and cyclopropanone that were fit to the experimental spectrum. Branching fractions are obtained based on the weighted fit of the m/z 56 signal.

Figure 4.4 shows the photoionization spectrum for the isomers at m/z 56 from the signal. The spectrum is interpolated with a least-squares fitting method weighted to the sum of the absolute photoionization spectra of several C_3H_3OH isomers obtained from the potential energy surface, given by Vanuzzo et al.⁸⁴ and Pham et al.⁵⁷ It was determined that the most abundant isomer of m/z 56 is acrolein with allenol and cyclopropanone at lower contributions. The isomers that were fit to the experimental spectrum obtained at m/z 56 are allenol, acrolein, methyl ketene, cyclopropanone, methyleneoxirane, and propargyl alcohol. The absolute photoionization spectra of the fitted isomers of m/z 56 is show in figure 4.5.

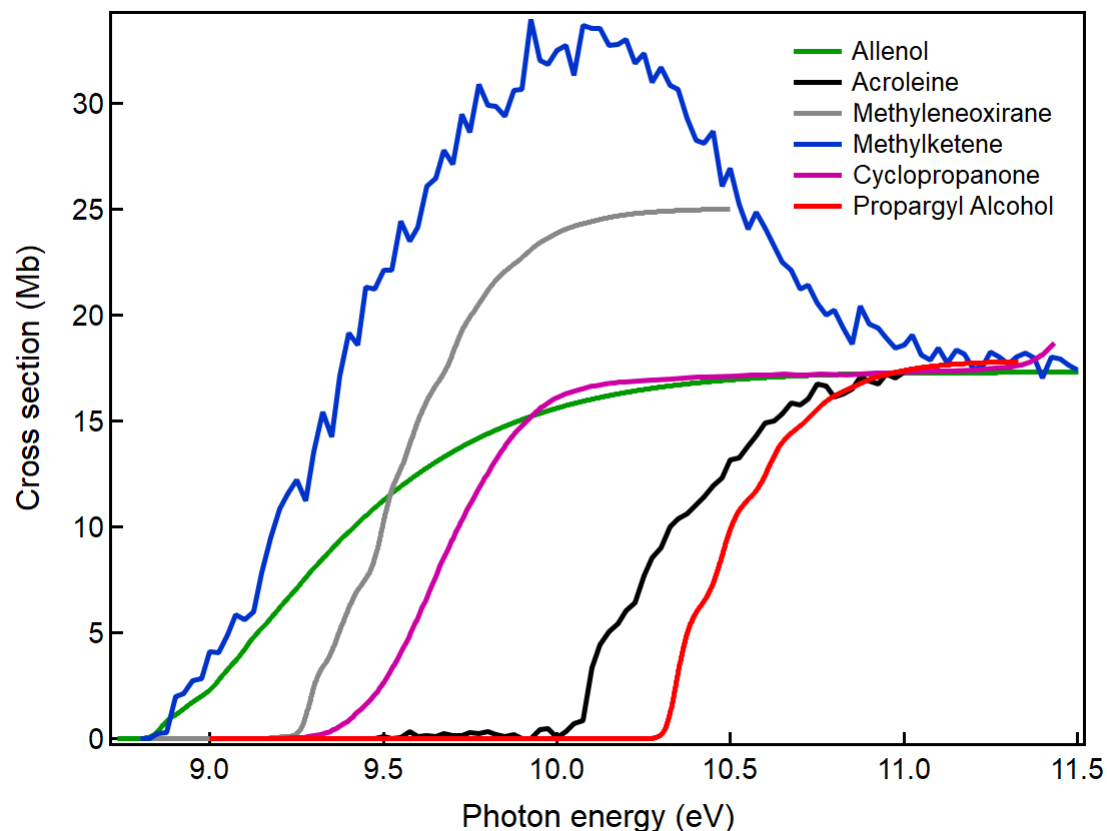


Figure 4.5. Absolute and calculated photoionization spectra of the potential isomers of m/z 56. Franck-Condon factors are calculated using the Gaussian⁶² suite of programs for cyclopropanone and propargyl alcohol. Allenol, acrolein, and methylketene absolute photoionization cross sections are experimentally determined by Savee et al.⁵⁹

4.4.2 High Signal Masses

The significant signals that appear with the addition of OH and their ionization energies are displayed in table 4.1. The identities of these species are confirmed by ionization onset. Of the masses that appear with the addition of the OH radical, m/z 42 of ethynol and ketene, and m/z 44 of acetaldehyde do not appear on the potential energy surface⁸⁴ and are not predicted products by computational studies⁵⁷. The signal at m/z 26 is assigned to acetylene at the higher ionization energy of 11.41 eV. m/z 27 is assigned to the viny radical by ionization signal onset. The signal at m/z 28 is assigned to ethylene by the photoionization spectrum and ionization

energy. The signals and 29 and 30 are assigned to the formyl radical and formaldehyde, respectively. Mass 54 is assigned to 2-propynal and propadienal by onset of ionization.

4.4.3 Determination of Branching Ratios of the Products of the OH + Radical Reaction

The branching ratios of the products for the OH + Radical reaction and their corresponding ionization cross sections are given in table 4.1. The relative concentrations of the molecular products are determined by taking the signal after 40 ms of reaction time has passed. All product concentrations are stable after the 40 ms of reaction time and can be compared to the relative concentration of the other species. Radical signals decay immediately after formation and cannot be quantified in the same way that molecular species are quantified due to the immediate decay of the radical signal. The time-dependent signal of the radical is fit to a function that takes into account the transient nature of the radical signal, shown as follows:

$$S_i(t) = \left(\frac{S'_i \cdot c_{1,i}}{c_{2,i} - c_{1,i}} \right) (e^{-c_{1,i}t} - e^{-c_{2,i}t})$$

Where, S'_i is the amount of precursor consumed, $c_{1,i}$ is the pseudo first-order rate coefficient for the formation of species "i", $c_{2,i}$ is the pseudo first-order rate coefficient for loss of the radical signal, and t is the reaction time. An example of a fit is shown in figure Figure 4.6. Some species that are expected to be formed are unable to be quantified due to known short lifetimes as is the case with $\text{CH}_3\text{CH}^{\bullet}$, and the lack of ionization cross section information being available as is the case with propynal at m/z 54.

Table 4.1. Table of experimentally validated species and their relative branching ratios at 298 K and 4 Torr.

Species	cross section (Mb)	Branching Ratio (298 K)
<chem>HC#CH</chem>	25	18.32%
<chem>H2C=C[CH]</chem>	11	17.70%
<chem>H2C=CH2</chem>	14	12.69%
HCO	13	15.55%
H ₂ CO	18.5	6.51%
<chem>C=CC=O</chem>	10	22.35%
<chem>C=C[OH]</chem>	4	6.04%
<chem>C1CC1=O</chem>	24.71	0.84%

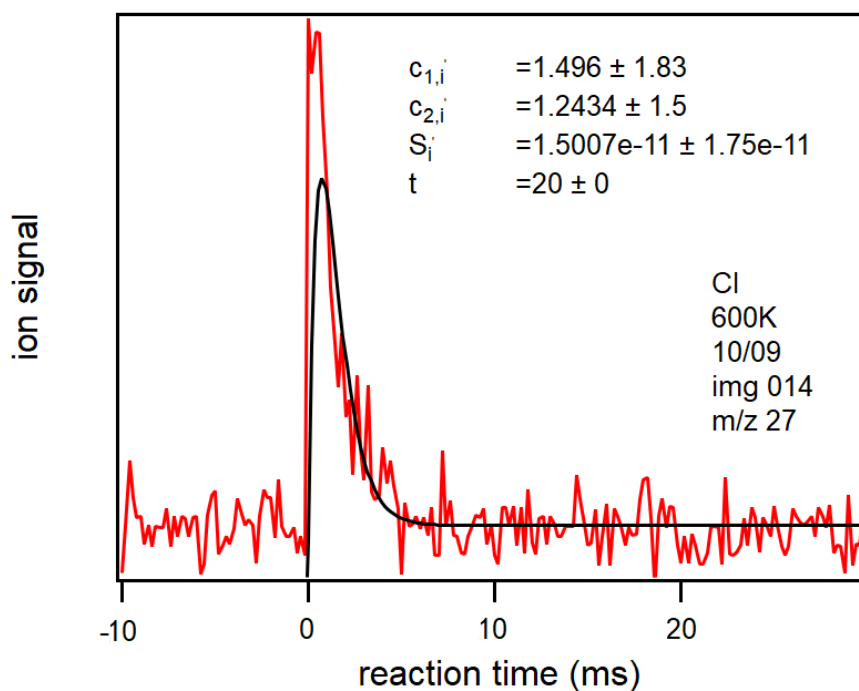


Figure 4.6. Fit of the radical signal at m/z 29. S'_i is the amount of precursor consumed, $c_{1,i}$ is the pseudo first-order rate coefficient for the formation of species "I", $c_{2,i}$ is the pseudo first-order rate coefficient for loss of the radical signal, and t is the reaction time. The fit to function allows determination of the theoretical radical signal without the radical decay.

4.4.4 500 K Reaction Conditions

The temperature was controlled by a Variac variable transformer. Flows were increased proportionally to compensate for the change in the number density of the flow due to the change in temperature. The branching ratios were unable to be quantified due to an intense signal coincidental with the laser pulse that is likely electrical interference from the Variac. The branching ratios of the product mass of m/z 56 at 500 K is shown in figure 4.7.

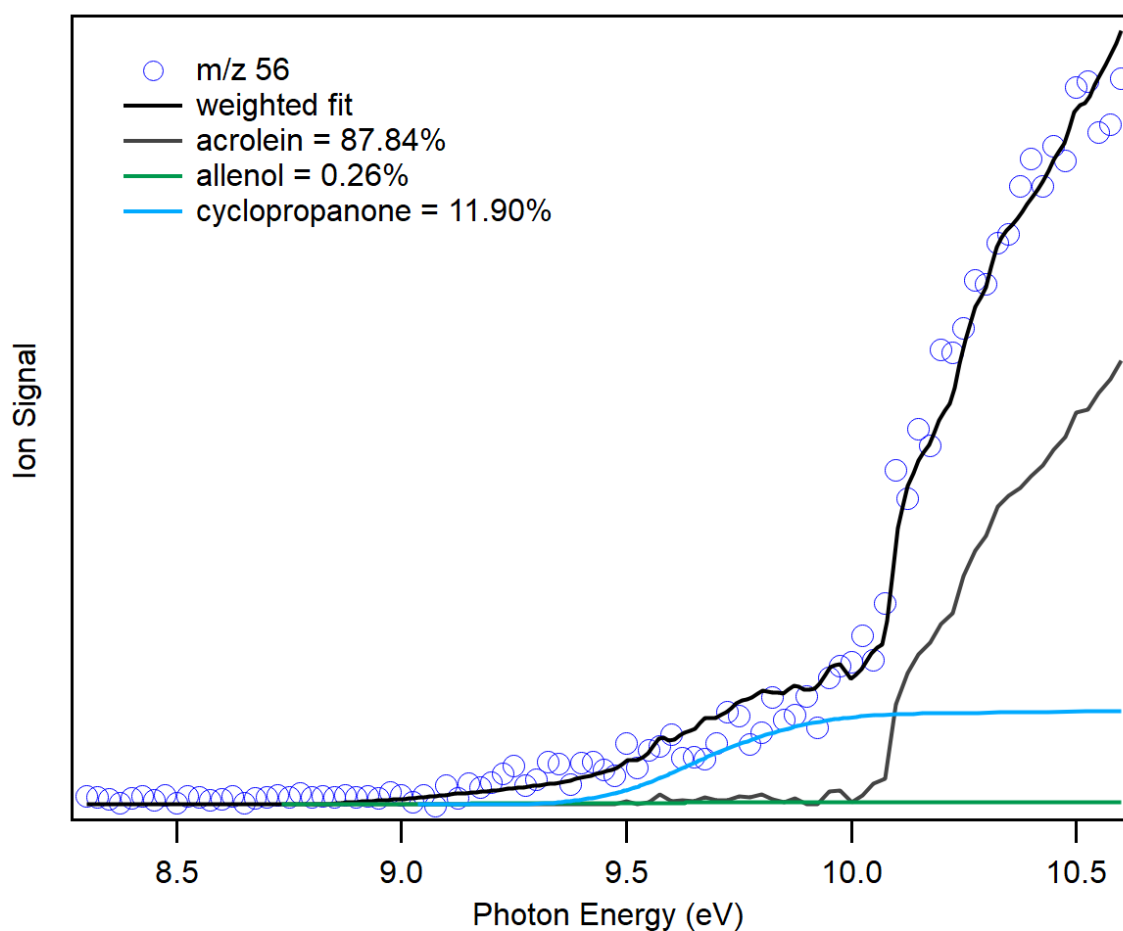


Figure 4.7. Fit of the m/z 56 signal at 500 K with the weighted cross sections of acrolein, allenol, and cyclopropanone.

The relative proportion of acrolein seems to remain approximately the same while the amount of allenol decreases and cyclopropanone increases.

4.5 Discussion

The most abundant product in the OH + propargyl alcohol is determined to be acrolein, which comprises 22 % of the species that were quantified by the analysis in this work. Acrolein is the lowest energy species in the PES and contributes the most to the signal at m/z 56. Allenol is the second largest contributor at m/z 56 and the more energetically favorable of the two entrance channel intermediates according to Pham et al. Pham et al concluded that the methyl ketene is the more favorable intermediate when compared to cyclopropanone in contrast to this work's finding that cyclopropanone is a better fit when the sum of the weighted photoionization spectra are compared to the signal at m/z 56. Due to the close ionization energy of cyclopropanone and methyl ketene (9.1 and 8.95 eV respectively), as well as the relatively low contribution of the third species at m/z 56 when compared to acrolein and allenol, it is difficult to determine whether or not this is simply due to experimental error. Pham et al. posits that the formation of C_2H_2 , C_2H_4 , C_3H_3 , HCO, and C_3H_3O are the most crucial paths in the OH + propargyl radical reaction. Though there exists a small signal for the m/z 55 that would correspond to the C_3H_3O radical, there does not exist cross section data to be able to fully quantify the species in the experiment. The most energetically favorable product of $C_2H_4 + CO$ is seen experimentally and comprises 12.69 % of the species that are quantified in this study. The acetylene formation pathway is another energetically favorable pathway on the PES and comprises 18.32% of the products quantified experimentally. The discrepancy in the ratio of C_2H_2 and its coproduct H_2CO indicates that a large proportion of C_2H_2 is produced via the $C_2H_2 + CO + H_2$ exit channel. The two isomers of propynal and propadienal are likely large contributors to the product, as represented by the large signal at m/z 54. These two products are formed by the ejection of H_2 with propynal being the more energetically and kinetically favorable

conformational isomer when compared to propadienal according to Pham et al.⁵⁷ Pham et al. depicts the four radical product pairs of $C_2H_3 + HCO$, $CH_2CHCO + H$, $CH_2CCHO + H$, and $CHCHCHO + H$ are all formed barrierlessly from the trans form of acrolein. C_2H_3 comprises 17.70% of the products quantified in this study. The radical isomers at m/z 55 have very little information regarding their cross sections and therefore are not able to be quantified in this study.

4.6 Conclusion

The products of the $OH(X^2\Pi)$ radical with the propargyl radical (C_3H_3) were studied using the multi multiplexed photoionization mass spectrometer at the Advanced Light Source of Lawrence Berkeley National Labs. Product analysis was performed at the pressures of 2, 4, 6, and 8 Torr with little variation due to pressure within the pressure range studied. Temperature was varied between 298 K and 500 K to observe the effect on the distribution of products. It was determined that acrolein is the most abundant closed-shell product at all temperatures, while the vinyl radical is the most abundant radical species that was detectable. The calculation from Pham et al.⁵⁷ is difficult to verify due to the inability to detect the ethylidene radical (C_2H_3) due to its extremely short lifespan.⁸⁵

References 4.7

(57) Pham, T. V.; Tue Trang, H. T. Combination Reactions of Propargyl Radical with Hydroxyl Radical and the Isomerization and Dissociation of trans-Propenal. *The Journal of Physical Chemistry A* **2020**, *124* (30), 6144-6157. DOI: 10.1021/acs.jpca.0c05106.

(59) Savee, J.; Soorkia, S.; Welz, O.; Selby, T.; Taatjes, C.; Osborn, D. Absolute photoionization cross-section of the propargyl radical. *The Journal of chemical physics* **2012**, *136*, 134307. DOI: 10.1063/1.3698282.

(62) Frisch, M., Trucks G., Schlegel H, et al. Gaussian 09. Gaussian Inc: Wallingford, CT, 2016, 2022.

(83) Nemeth, G. I.; Selzle, H. L.; Schlag, E. W. Magnetic ZEKE experiments with mass analysis. *Chemical Physics Letters* **1993**, *215* (1), 151-155. DOI: [https://doi.org/10.1016/0009-2614\(93\)89279-Q](https://doi.org/10.1016/0009-2614(93)89279-Q).

(84) Vanuzzo, G.; Balucani, N.; Leonori, F.; Stranges, D.; Falcinelli, S.; Bergeat, A.; Casavecchia, P.; Gimondi, I.; Cavallotti, C. Isomer-Specific Chemistry in the Propyne and Allene Reactions with Oxygen Atoms: CH₃CH + CO versus CH₂CH₂ + CO Products. *The Journal of Physical Chemistry Letters* **2016**, *7*. DOI: 10.1021/acs.jpcllett.6b00262.

(85) Datta, S.; Davis, H. F. Direct Observation of Ethylidene (CH₃CH), the Elusive High-Energy Isomer of Ethylene. *The Journal of Physical Chemistry Letters* **2020**, *11* (24), 10476-10481. DOI: 10.1021/acs.jpcllett.0c03282.

Chapter 5: Concluding Remarks

Understanding the role of radical chemistry is imperative to improving the models for the processes of molecular growth. Processes like those that occur in the interstellar medium and in the formation of PAHs. This body of work provides a novel experimental setup and its potential use as a means to study high-temperature chemistry as well as the product analysis of the OH + propargyl reaction, both of which are especially important molecules in regard to combustion chemistry.

There is still much work to be done with the finalizing of the conditions for the high-temperature fast flow reactor, as the temperature within the flow must be validated spectroscopically. Analysis of the rovibronic spectrum of CN radical in conjunction with the PGOPHER program was proven to be a viable method in determining the temperature of a gas. This is the only viable way to determine the temperature of the gas within the fast flow as the pulses are faster than any fast response thermocouple can record. The CN or OH radical must be used to determine whether or not the temperature is uniform for various lengths away from the establishment of the high-temperature flow. After the temperature of the experimental setup is validated, kinetic studies regarding a known reaction must be performed using the novel flow cell to confirm that the flow cell is operational for kinetic studies. After the temperature and flow conditions are fully validated using spectroscopic studies and kinetic studies, the final step to completing the experimental setup is to attach a mass spectrometer to the end of the flow to allow for product detection experiments to be performed without the need for travel to outside facilities.

The OH + propargyl reaction is an extremely important reaction in the study of combustion systems and PAH formation due to propargyl's well established role in the formation of the first aromatic ring. It was shown that there is little to no reaction of the OH radical to the "head" side of the propargyl radical. This sentiment is echoed in the work by Pham et al.⁵⁷ as the pathway to form allenol and its subsequent exit products is more favorable than that of propargyl alcohol. The OH + propargyl reaction is a viable reaction in combustion, as the radical is shown in this study to readily react to form primarily acrolein as a product, with many decomposition pathways available for the isomer at m/z 56 to proceed through. This work establishes that it is possible given the proper conditions to perform radical-radical experiments, allowing many previously unexplored reactions to be accessible for study. A more comprehensive study of the temperature dependency of the OH + propargyl reaction would do much in illuminating the effect of temperature on the relative concentration of the products that are formed in the reaction. Additional Master Equation and RRKM calculations performed with the m/z 56 isomers included in the potential exit channels would be an excellent addition to the computational work that was performed by Pham et al.⁵⁹

References

(57) Pham, T. V.; Tue Trang, H. T. Combination Reactions of Propargyl Radical with Hydroxyl Radical and the Isomerization and Dissociation of trans-Propenal. *The Journal of Physical Chemistry A* **2020**, *124* (30), 6144-6157. DOI: 10.1021/acs.jpca.0c05106.

(59) Savee, J.; Soorkia, S.; Welz, O.; Selby, T.; Taatjes, C.; Osborn, D. Absolute photoionization cross-section of the propargyl radical. *The Journal of chemical physics* **2012**, *136*, 134307. DOI: 10.1063/1.3698282.

Appendix

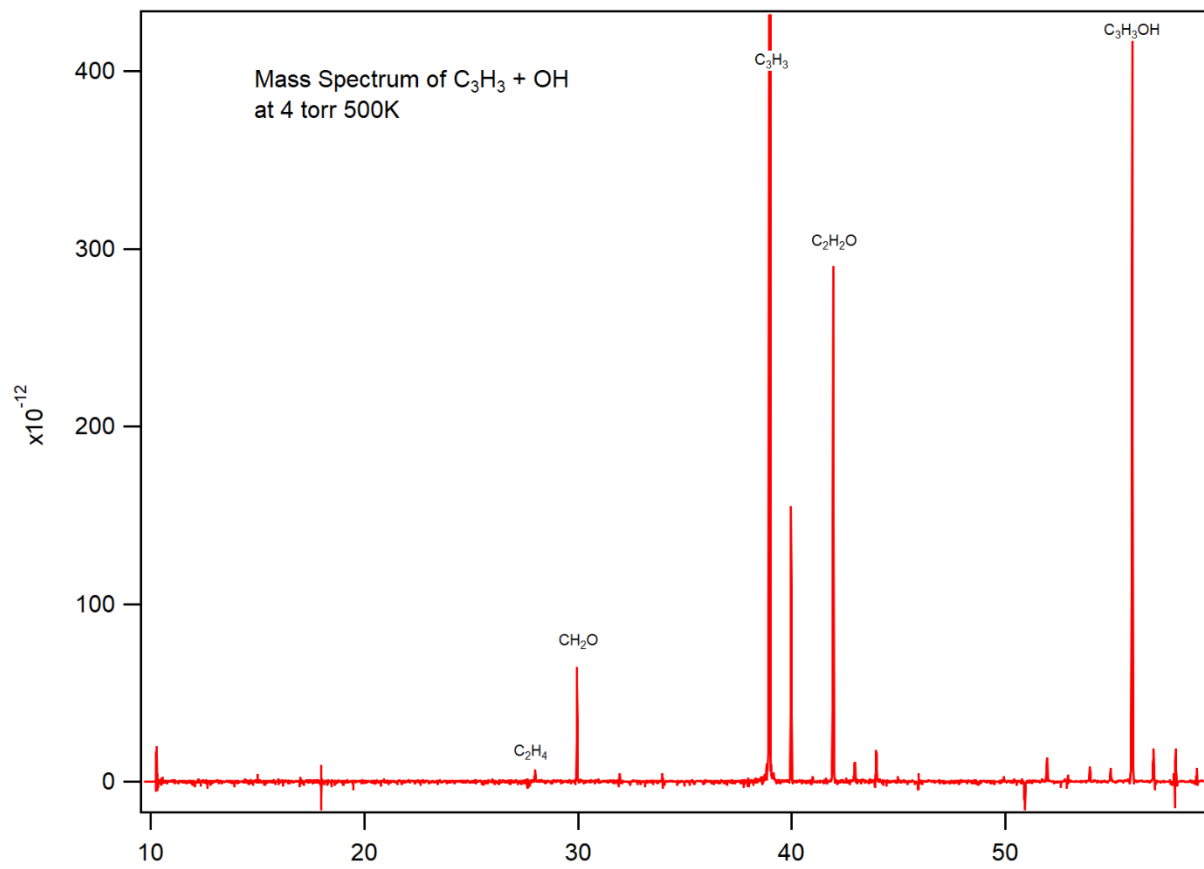


Figure A1. Mass spectrum of $C_3H_3Cl + HOOH$ at 500 K

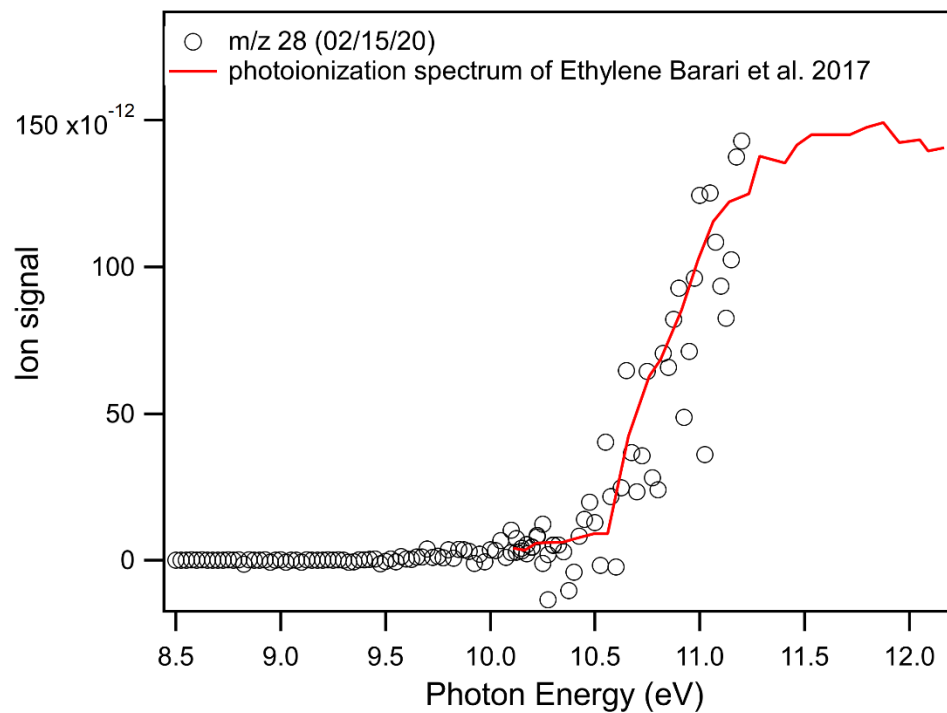


Figure A2. Photoionization spectrum of m/z 28 of the $C_3H_3Cl + HOOH$ reaction superimposed on the photoionization spectrum of ethylene

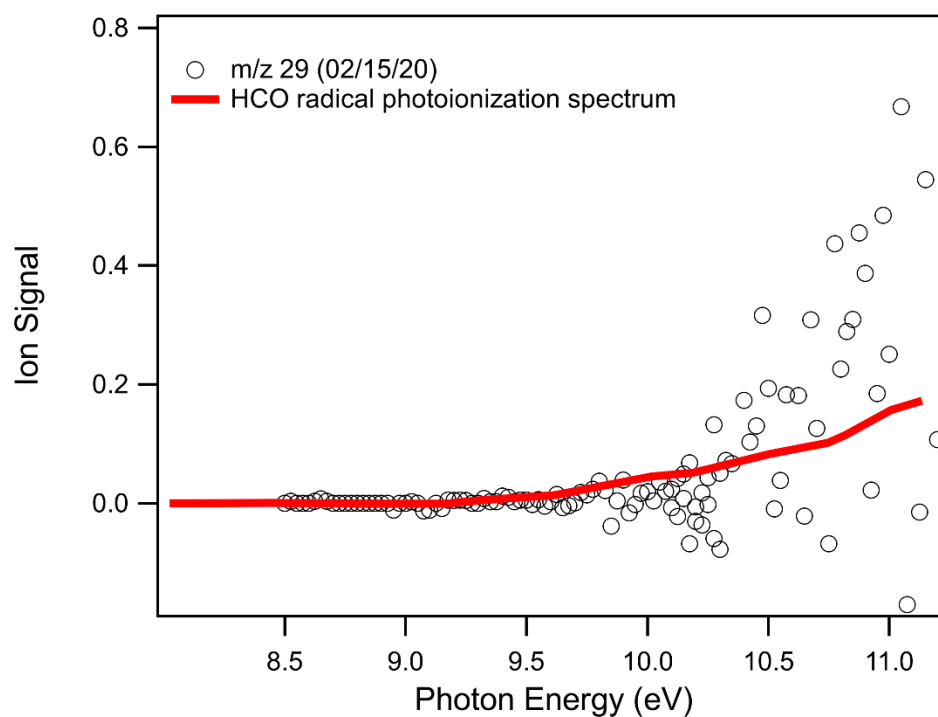


Figure A3. Photoionization spectrum of m/z 29 of the $C_3H_3Cl + HOOH$ reaction superimposed on the photoionization spectrum of the HCO radical

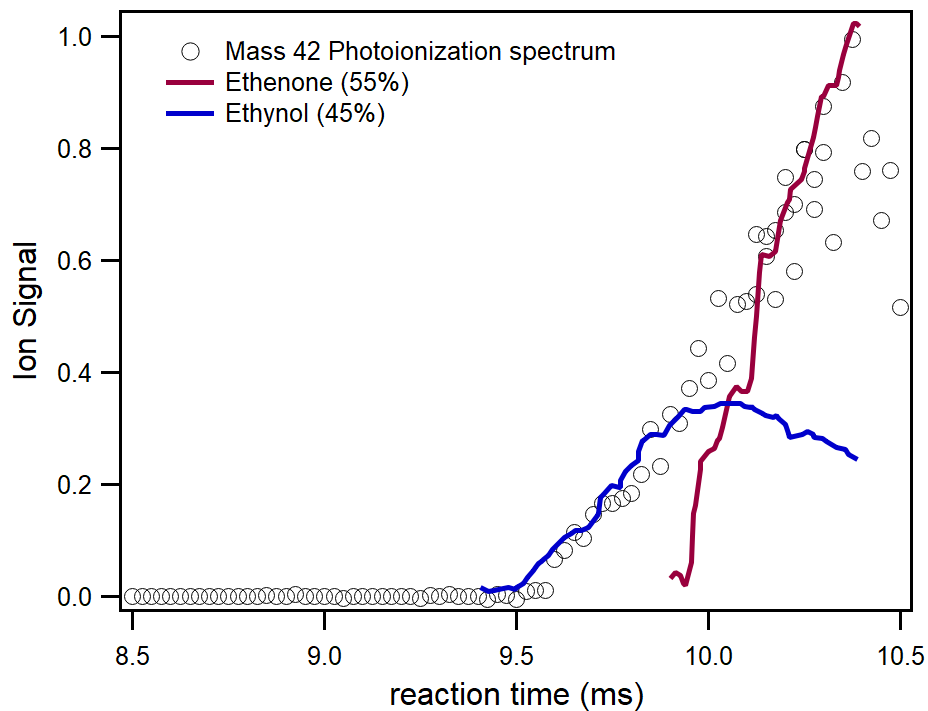


Figure A4. Photoionization spectrum of m/z 42 of the $C_3H_3Cl + HOOH$ reaction superimposed on the experimental spectrum of ethenone and ethynol

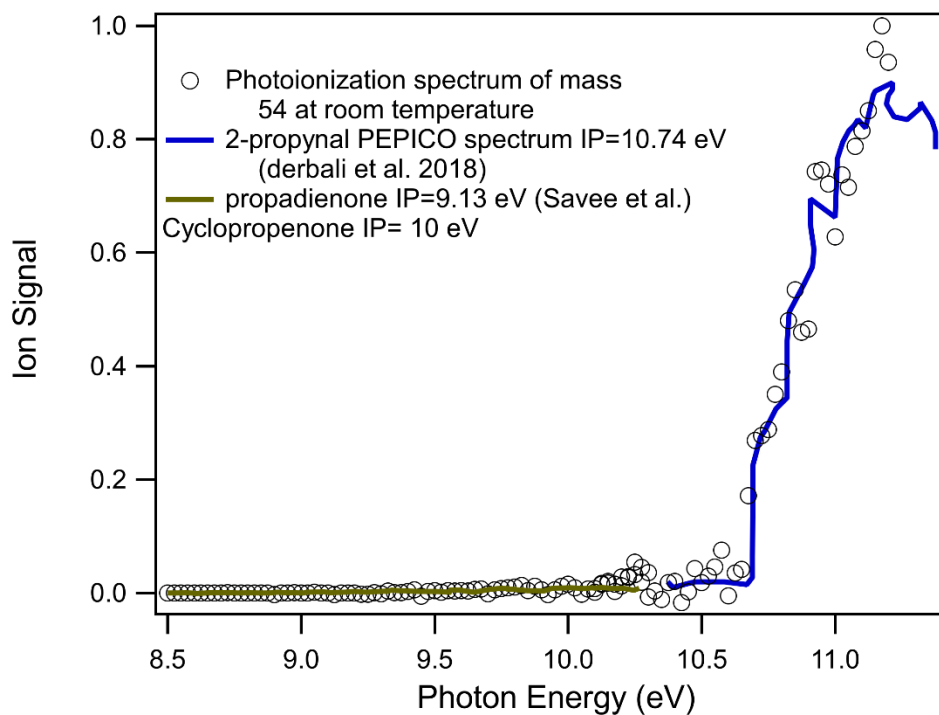


Figure A5. Photoionization spectrum of m/z 52 of the $C_3H_3Cl + HOOH$ reaction superimposed onto the experimental photoionization spectrum of propadienone and the PEPICO spectrum of 2-propynal